

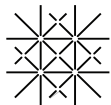
Detailed analysis of single molecular junctions for novel computing architectures

Inauguraldissertation

zur
Erlangung der Würde eines Doktors der Philosophie
vorgelegt der
Philosophisch-Naturwissenschaftlichen Fakultät
der Universität Basel

von

Anton Vladyka
aus Jalta, Ukraine



**Universität
Basel**

Basel, 2017

Genehmigt von der Philosophisch-Naturwissenschaftlichen Fakultät
auf Antrag von
Prof. Dr. Christian Schönenberger
PD Dr. Michel Calame
Dr. habil. Dominique Vuillaume

Basel, den 27. Februar 2017

Prof. Dr. Jörg Schibler
Dekan

Contents

Introduction	vi
Part I. Single molecular junctions	1
1 Single molecule measurement technique	2
1.1 Mechanically controlled break junction in liquid environment	2
1.2 Measurement scheme	3
1.3 Data analysis	5
1.3.1 Evolution plot	5
1.3.2 Conductance histogram	5
1.3.3 Conductance histogram evolution plot	7
1.3.4 Conductance–displacement histogram	7
1.3.5 Attenuation factor calibration	7
1.3.6 Plateau length analysis	9
1.3.7 Yield of junction formation estimation	10
2 Effect of highly polar anchor groups	12
2.1 Double plateaus in conductance traces	13
2.2 Plateau length analysis	16
2.3 Effect of concentration on molecular junction formation	17
2.4 Theoretical investigations	20
2.5 Closing traces analysis	21
2.6 Nature of the low-conductance plateau	23
2.7 Theoretical analysis of BdNC molecular chains	23
2.8 Influence of side groups on the molecular junction formation	24
2.9 Asymmetry of conductance peaks	29

2.10 Analysis of conductance plateaus	32
2.11 Further chaining: 3 molecules?	33
2.12 Current-voltage characterization	36
2.13 Conclusion	37
3 Properties of π-stacked molecular junctions	38
3.1 Studied molecules	39
3.2 Electrical characterization	39
3.2.1 CYS-NA measurements in MCBJ	39
3.2.2 CYS-NA measurements in NP array	40
3.2.3 CYS-PA measurements	41
3.3 Theoretical investigations	42
3.3.1 Geometry optimization	42
3.3.2 Classical molecular dynamics	45
3.3.3 Modeling of electrical response	46
3.4 Overview of experimental and theoretical results	48
 Part II. Molecular networks	 49
4 Nanoparticle arrays as a platform for molecular electronics	50
4.1 Fabrication techniques	51
4.2 Charge transport in the array	52
4.3 Emerging functionalities in arrays	53
4.3.1 Optical switching in NP array	53
4.3.2 Electrochemical switching	54
4.3.3 Strain sensing	54
4.4 Dimension control in NP array	55
 5 Graphene electrodes for hybrid devices	57
5.1 Graphene as an electrode for NP array	58
5.2 Downscaling the NPA-based hybrid devices	59
5.2.1 Optimization of PMMA-based e-beam lithography	60
5.2.2 Further miniaturization of G/NPAs: HSQ approach	62
5.2.3 Local transfer of nanoparticle arrays	63
5.3 Functionality of G/NPA devices	67
5.3.1 Molecular exchange	67
5.3.2 Optical molecular switching in G/NPA	69
5.4 Conclusion and outlook	73

6 NP array as a gate for graphene FET	74
6.1 Graphene FET with nanoparticle array	75
6.2 Nanoparticle array as a top gate for the graphene FET	77
6.3 Frequency response of GFET with NPA	79
6.4 Overview and outlook	81
Conclusion and outlook	84
Bibliography	86
Appendices	97
A Functional molecules measured in MCBJ	97
A.1 Single-molecule characterization of organic semiconductor Cys-NTCDI	97
A.2 Spiropyran-based compound as a possible molecular optical switch .	101
B Fabrication	104
B.1 MCBJ fabrication	104
B.2 Graphene growth and transfer	105
B.3 Graphene patterning for multi-terminal hybrid devices	107
B.4 PMMA master fabrication	107
B.5 PDMS stamps fabrication	109
B.6 Nanoparticles preparation	109
B.6.1 Synthesis	110
B.6.2 Functionalization	110
B.7 Nanoparticles transfer	111
B.8 NPSAN fabrication	112
List of publications	114
Curriculum Vitae	116

Introduction

“There’s Plenty of Room at the Bottom.”
— Richard Feynman, Caltech, 1969

The 2016 Nobel Prize in Chemistry was awarded to Fraser Stoddart, Jean-Pierre Sauvage and Ben Feringa *“for the design and synthesis of molecular machines”*. “Molecular machine” is a general term describing molecular-based nanoscale object which can controllably perform some mechanical operations. For instance, Feringa *et al.* [1, 2] proposed the ‘molecular motor’, which converts illumination into motion on the surface. Mechanically interlocked molecules like catenanes and rotaxenes were proposed to act as ‘molecular muscles’ [3, 4]. Another proposed molecular machines are ‘molecular switches’ — the molecules with several stable states with possibility to switch between them. Several molecular switches can form a molecular logic gate [5]. The latter concept is a central theme of the Molecular electronics, an idea to introduce molecules into electrical circuits.

The field of molecular electronics can be traced back to 1950s, when D.D. Eley and D. I. Spivey performed first electrical measurements of organic crystals, proteins and nucleic acids [6–8]. Bernhard Mann and Hans Kuhn electrically characterized an organic device: the monolayer of fatty acid salt sandwiched between metal electrodes [9]. A first actual introduction of the field was done by Aviram and Ratner in 1974 [10]. They proposed the chemical structure of the molecule which can electrically act like a active device, a diode, by combining inside the structure the moieties with electron-donating and electron-withdrawing properties separated by insulating molecular bridge. The idea to use molecules as electronic components was inspiring, since all the molecules of one compound are identical and are nanometer in size. The diversity of existing organic compounds creates huge space of possible single molecule devices, and synthetic chemistry approaches widen this space to almost infinity. Using chemical design, the molecules with a variety of

possible functions can be created. Plenty of molecular-based devices were proposed such as molecular wires [11], molecular switches [12, 13], ‘Aviram-Ratner inspired’ molecular diodes [14–16], molecular transistors [17, 18] and molecular memory cells [19, 20].

The functionality of all these molecular devices could not be demonstrated without the development of the instruments for electrical measurements at the single-molecule level. The interest for this field started to arise after the invention of scanning tunneling microscope [21] (STM) and atomic force microscope [22] (AFM), which allowed to ‘look’ closely on the molecule and to probe it electrically [23]. The development of mechanically-controlled break junction approach [24–26] has let to measure actual single molecular device (named single molecule junction) [27, 28]. And finally after the first successful measurements of the single molecular junction using STM [29] the field of single molecule electronics started to grow rapidly. For now, the most common approaches to measure the molecular devices are STM- and AFM-based break junctions as well as mechanically controlled break junctions, but another techniques such as electromigrated junctions [30, 31] or eutectic gallium–indium (EGaIn) junctions approach [32] are also utilized.

Electrical properties of molecular junctions are defined by the electronic structure of the molecule (molecular backbone), by the linker groups, by the material of the electrodes, by the environment. Some of this properties can be predicted by modern quantum chemistry simulations, and desired functionality can be achieved by the chemical design. All this makes molecular electronics attractive to synthetic chemists and physicists. Additionally, a charge transfer (which can be considered as charge transport on the level of individual electrons) in organic molecules plays an important role in the life biology, e.g. in the processes of photosynthesis or energy storage in the cells etc. Therefore, electrical investigations of individual molecules covers a huge variety of fields.

Part 1 of this dissertation covers investigations of electrical properties on the level of single molecular junctions. First, general approach of MCBJ measurements and data analysis is described in Chapter 1. In-depth investigation of isocyanide molecular junctions is presented in Chapter 2. Chapter 3 shows combined experimental and theoretical study of the mechanical stability and its influence on the conductance for π -stacked dimers. Additional investigations on functional molecules are presented in Appendix A.

A long-term vision of the molecular-scale electronics is the development of unconventional computing scheme based on the properties of individual molecules. Since the invention of the first digital computing machines (Zuse’s Z3 in 1943 and ENIAC in 1946), the development of new technologies — such as transistors, integrated circuits, processors — tremendously increased the computing power. Modern computers are remarkably more powerful than the first computers of 1940s–1950s. However, in the upcoming years the computing power of Turing-style computers is expected to reach the limit, since further scaling down the computing

units has a fundamental constrains in the dimensions. In addition, there are still a lot of computational problems which require exponential amount of resources and computing power. Thereby, the development and implementation of new, unconventional computing paradigms is required.

One of the most advanced concepts of unconventional computing is brain-inspired approach. Indeed, human brain has unique computing performance with extremely low power consumption. The hypothetical modern computer to simulate human brain behavior requires gigawatts of power, while the brain itself consumes around 20 W [33]. Therefore even at the beginning of computing era in 1950s von Neumann was looking at the brain for the future developments [34].

Contrary to the classical computer architectures (namely, von Neumann architecture and Harvard architecture, where computing unit and memory are physically separated [35]), the data memory, instructions memory as well as processing unit(s) in the brain are implemented in the same entities — neurons (the neural cells) and synapses (the connections between neurons). Human brain consists of about 10^{11} neurons and 10^{15} synapses, thereby, it has much larger integration scale than any other existing computing unit [36]. The clock frequency of modern processors is about 3–4 GHz, but all operations are sequential. Human brain, in contrast, operates at low frequencies in a range of 10–100 Hz [37], but the computing is performed in the massively parallel way, which can not be achieved in the classical computers [38].

All the approaches to mimic brain behavior in the conventional devices get the name of neuromorphic engineering. There are two main approaches in this field: first, to simulate the neuron and its synaptic behavior with possible scaling to the network level, and second, to achieve computing from the network of identical objects.

Current understanding of the memory functionality in the human brain is the consequence of two basic types of synaptic plasticity: long-term potentiation (LTP) and short-term plasticity (STP) [39]. Both effects describe response of the neuron on the input electrical signals with different frequencies. Physical implementation of STP and LTP was demonstrated in inorganic devices [40] and in hybrid nanoparticle-organic devices [41, 42].

Tour *et al.* [43] demonstrated theoretical possibility to create a programmable nanocell, designed using molecular network. For the simulation, the model of negative differential resistance (NDR) measured in self-assembled monolayer by Chen *et al.* [44] was used. Following this theoretical idea, Bose *et al.* [45] created ‘programmable’ unordered blob of nanoparticles in a Coulomb blockade regime. Desired functionality was achieved by applying genetic algorithm to the device. Listed systems satisfy the criteria for physical realization of the neural network, which are the following: universality (i.e. programmability), robustness (defect- and fault tolerance) and evolvability.

Another concept of memory-type elements is an idea of memristors. The memris-

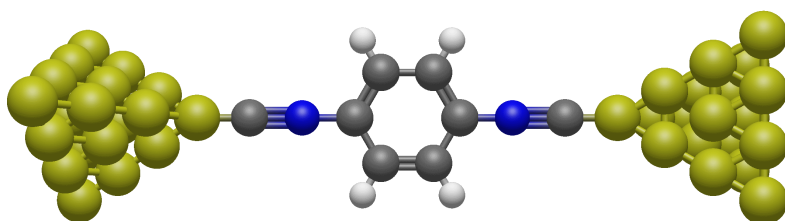
tor, initially described as ‘missing circuit element’ [46, 47], attracts a lot of interest for variety of applications [48]. Generalization of the memory-type circuit elements led to the concepts of memristive elements [49] and memristive networks [50, 51].

The nanoparticles in the device proposed by Bose *et al.* [45] were covered with an insulating shell of 1-octanethiol molecules. Unordered three-dimensional structure does not allow to alter the molecular shell after fabrication, which therefore required operation at low temperatures to achieve needed functionality. However, self-assembled monolayer on nanoparticles (nanoparticle array, NPA) is a convenient platform for molecular functionality testing due to possibility to insert functional molecules into the molecular network. For example, non-linear response can be achieved by insertion proper molecules into the array. Thereby, we utilize this platform for the unconventional computing approach investigations in the Part 2 of this dissertation.

The description of the nanoparticle array platform and basic functionalities are presented in the Chapter 4. Development of hybrid nanoparticle-based devices with graphene electrodes is presented in the Chapter 5. Finally, Chapter 6 shows investigation of nanoparticle effect on the properties of graphene field-effect transistor.

Part I

Single molecular junctions



Single molecule measurement technique



Electrical characterization of molecular junctions is usually carried out using three approaches: scanning tunneling microscope break junction (STM-BJ), conductive probe atomic force microscope break junction (CP AFM-BJ) and mechanically controlled break junction (MCBJ). In all listed approaches the metallic wire is controllably broken to form atomically sharp electrodes separated with sub-nanometer gap, which then is bridged by the molecule(-s). All single molecule measurements in this dissertation were performed using the MCBJ approach with lithographically defined samples [52].

1.1 Mechanically controlled break junction in liquid environment

The idea to fabricate mechanically controlled break junction originates from early studies of point contacts [24, 53]. The first micro- and nanofabricated break junctions were used to investigate quantum properties of metallic point contacts [25,

54] and tunneling current through nanogaps [26]. But the first measurements of electrical properties of a single molecule using the MCBJ approach [27] vastly increased the interest in the field of molecular electronics in general and in MCBJ in particular.

As a consequence of single molecule sensitivity, any contaminant should be avoided during the measurements and therefore all measurements have to be performed in a controlled environment. One option is to use high vacuum (HV) and low temperatures (LT), where the dynamics of the molecules on the electrodes is suppressed. Another possibility is to measure the molecular junctions in solution, where a controlled environment is created by the excess solvent molecules. A liquid environment is also adding possibility for external tuning of the molecular junctions, e.g. electrochemically [55–57]. In this dissertation, the latter approach is used: all measurements are performed in solution at room temperature (RT). The typical solvent for these measurements is a mixture of tetrahydrofuran (THF) and mesitylene (1,3,5-trimethylbenzene, MES) 1:4 (v/v).

The samples were fabricated following a previously developed procedure [52, 58] (see Section B.1). In brief, metal electrodes (5 nm Ti and 60 nm Au) were fabricated on a polyimide-covered spring steel plate using e-beam lithography. The constriction of the electrodes is 70–100 nanometers in width. To reduce possible leakage currents, the samples were then covered with UV-sensitive polyimide (not shown on Fig. 1.1a for simplicity), and only small area around the constriction of the electrodes was deprotected using UV-lithography technique. At the last step, the polyimide layer was partially removed using reactive-ion plasma etching (RIE). During etching, approximately 2 μm thick layer of polyimide is removed and a suspended gold bridge is formed with the typical length of 1 μm (Fig. 1.1b). The liquid cell (teflon rubber ring, Viton[®]; Fig. 1.1a) was glued to the substrate using polyimide and baked in high vacuum at 350 °C for 1 hour. The volume of the liquid cell is about 200 μL .

Before the measurements every sample is rinsed in acetone and isopropyl alcohol, dried in N_2 and additionally cleaned using UV/ozone for 10 minutes. After the cleaning procedure, the sample is installed into a home-built three-point bending setup for electrical characterization.

1.2 Measurement scheme

Electrical measurements are performed using an 18-bit data-acquisition (DAQ) board (National Instruments PXI-6289) as a source as well as a measurement tool (Fig. 1.2). The MCBJ sample R_{BJ} is connected in series with a pre-resistor R_{S} of 100 k Ω to prevent high current flowing through the closed junction. The electrical signal is amplified using a home-made IV converter (SP895/SP895a, University of Basel) with autoranging unit, which switches the gain of the IV converter (R_{gain})

1. Single molecule measurement technique

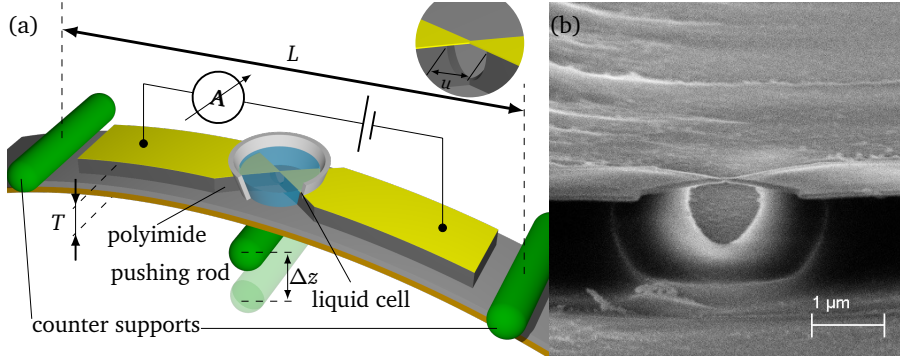


Figure 1.1: (a) Schematics and characteristic dimensions of MCBJ setup for liquid measurements. (b) SEM image of the MCBJ sample.

from 10^5 to 10^8 V/A. The switching time between different gains is around 1 ms, and the bandwidth of the IV converter is 800 Hz at $R_{\text{gain}} = 10^8$ V/A. The pushing rod is driven by a stepper motor with a system of reduction gears. The final resolution of the mechanical subsystem is 3 nm per step. The setup is controlled via LabView.

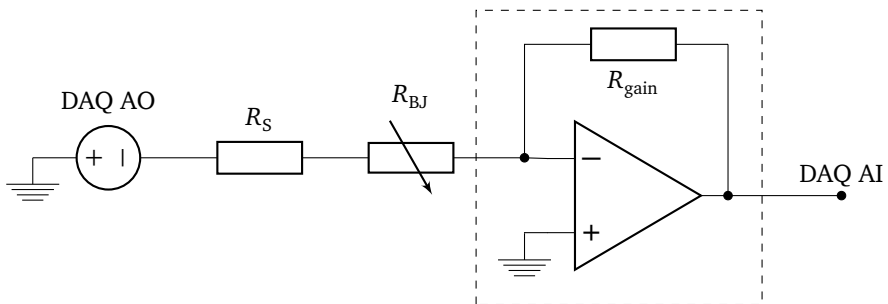


Figure 1.2: Electrical scheme of the measurements. A voltage is applied and measured using DAQ board (NI PXI-6289). DAQ AO and DAQ AI refer to analog output and analog input, respectively. The break junction sample R_{BJ} is connected in series with a pre-resistor $R_S = 100\text{ k}\Omega$. The signal is converted into voltage with a home-made IV-converter with autoranging unit (dashed rectangle).

During measurements, the pushing rod is moving with a speed of $31.2 \mu\text{m/s}$. Typically, the applied bias voltage is $V_{\text{out}} = 0.1 \text{ V}$ and the sampling rate is 500 Hz.

The voltage V_{meas} , measured by the DAQ, is converted into conductance G using the formula:

$$G(G_0) = \frac{1}{G_0} \frac{1}{\frac{V_{\text{out}R_{\text{gain}}}}{V_{\text{meas}}} - R_s}, \quad (1.1)$$

where $G_0 = 2\frac{e^2}{h} = 77.5 \mu\text{S} = \frac{1}{12900 \Omega}$ is a conductance quantum.

The analog input channels of the DAQ board are configured to work in the bipolar mode with a range of $(-10, 10)$ V. Thus, the resolution of the measured input voltages is:

$$\delta V_{\text{meas}} = \frac{20 \text{ V}}{2^{18}} \approx 80 \mu\text{V}, \quad (1.2)$$

and the corresponding resolution of the measured conductance is

$$\delta G(G_0) = \frac{1}{G_0} \frac{1}{\frac{V_{\text{out}} R_{\text{gain}}}{\delta V_{\text{meas}}}} = 12900 \Omega \cdot \frac{80 \mu\text{V}}{0.1 \text{ V} \cdot 10^8 \text{ V/A}} = 1.03 \cdot 10^{-7}. \quad (1.3)$$

The current noise of the setup is about 10 pA, which corresponds to a conductance detection limit of $10^{-6} G_0$ at 100 mV bias voltage.

In all measurements the conductance traces were recorded by repeatedly opening the junction while the measured conductance reaches the setup noise level, followed by its closing to the bulk gold contact ($\approx 10 G_0$).

1.3 Data analysis

The investigation of single molecular junctions includes acquisition of data from plenty (hundreds to thousands) conductance traces (Fig. 1.3a), typically with constant applied bias of 100 mV, followed by statistical analysis of the measured data [29, 58]. Every conductance trace includes the information about the pushing rod displacement Δz and the corresponding conductance value G/G_0 . In the following the different ways to depict the data are described in detail.

1.3.1 Evolution plot

Closing of the junction to conductance values above G_0 , i.e. to the ‘bulk’ gold–gold contact, causes reconfiguration of the gold atoms on the electrodes, and the breaking point of the junction can be different from the previous cycle with respect to the absolute position of the electrodes. The stability of the junction can be observed on the evolution plot (Fig. 1.3b). The evolution plot is a two-dimensional map in *displacement–trace number* coordinates where every row represents an individual conductance trace.

1.3.2 Conductance histogram

Conductance histogram (Fig. 1.3c) shows the probability to observe a specific value of conductance in all the measured traces. Conductance histograms are usually plotted in the counts vs. $\log(G/G_0)$ coordinates. $\log(G/G_0)$ values are binned with a bin-size of 0.04. Counts are normalized according to the number of traces taken

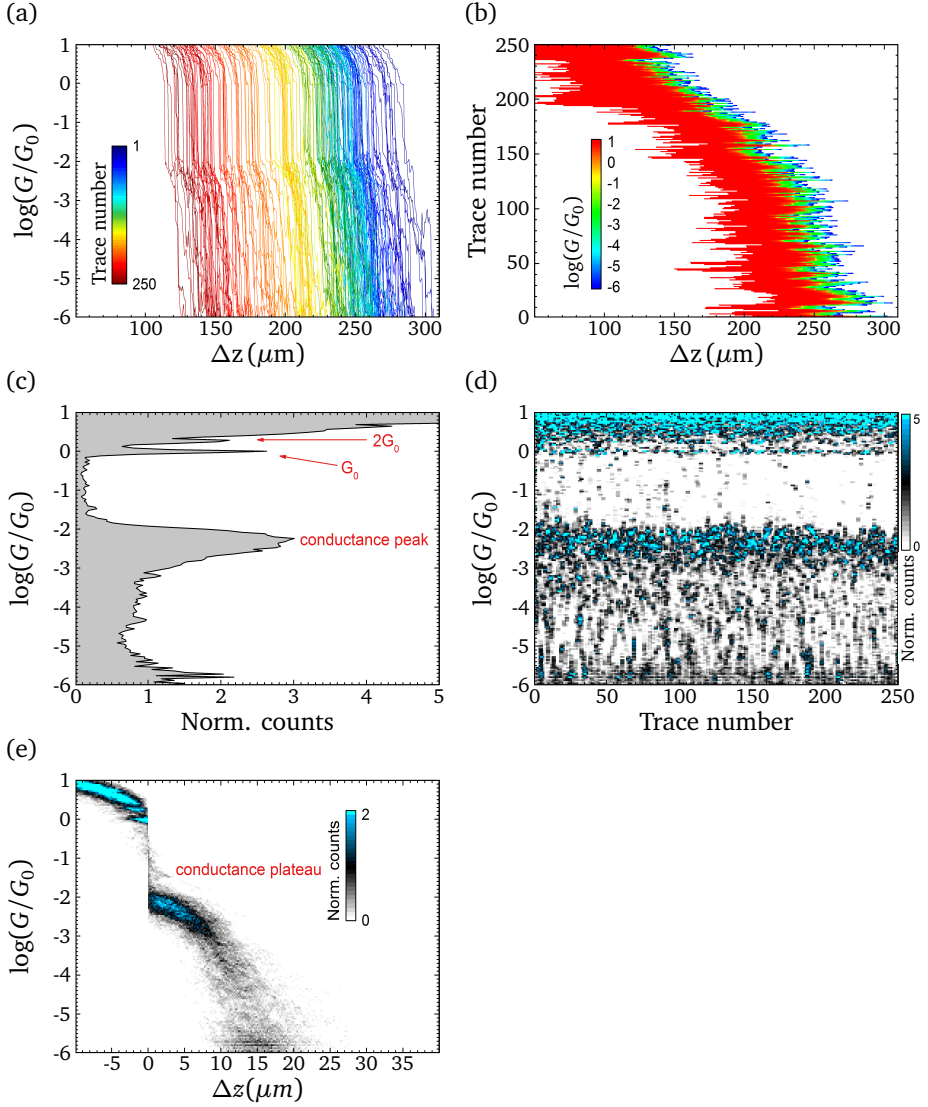


Figure 1.3: Analysis of break junction data. (a) Raw data: 250 opening conductance traces for MBdNC molecule (see Chapter 2). Color-coding shows the trace number from blue to red. (b) Evolution plot. Every row of the plot shows a color-coded conductance value vs. displacement. (c) Conductance histogram. (d) Conductance histogram evolution plot. Every column of the plot shows a color-coded conductance histogram of three consecutive traces, i.e. the column with the trace number 50 shows conductance histogram for the traces 49, 50, 51. (e) Conductance-displacement histogram. In all the graphs Δz represents the displacement of the pushing rod, not the distance between the electrodes (see subsection 1.3.5).

into analysis. Stable configurations, e.g. signatures of molecular conductance, form peaks in the conductance histogram. Fitting of these peaks provides a quantitative characterization of the molecular junction.

1.3.3 Conductance histogram evolution plot

Conductance histogram evolution plot (Fig. 1.3d) shows the time evolution of the conductance histogram. In this two-dimensional map every column (or row, depending on the chosen axes) represents a conductance histogram of the individual trace (or several consecutive traces) corresponding to the trace number. On this map we can clearly observe the stability of the conductance plateau(-s) and any changes happening in the junction over time, which affect the conductance histogram.

1.3.4 Conductance–displacement histogram

More detailed information about a molecular junction can be deduced from a conductance–displacement histogram (Fig. 1.3e), which is a two-dimensional map in (*conductance*, *displacement*) coordinates, where every point (d_i, G_j) shows the probability of the configuration with a certain conductance value G_j at a specific displacement d_i of the electrodes. Stable molecular configurations form conductance plateaus in the conductance–displacement histogram. Since the breaking of the atomic Au–Au contact occurs at a different pushing rod displacement for every conductance trace (cf. Fig. 1.3a–b), a trace alignment procedure is required. The breaking point is determined for every trace individually, then traces are shifted so, that all breaking points coincide, and a two-dimensional binning procedure is performed. Conductance values $\log(G/G_0)$ are binned with a bin-size of 0.04, Δz values with a bin-size of $0.187\text{ }\mu\text{m}$ for non-calibrated graphs, and Δd values with a bin-size of $0.15\text{ }\text{\AA}$ for calibrated graphs (see Subsection 1.3.5). Counts are also normalized according to the number of traces taken into analysis.

1.3.5 Attenuation factor calibration

One important advantage of the STM-based break junction approach is the ‘built-in’ information about the displacement of the electrodes. In contrast, in mechanically controlled break junction the ‘controlled’ entity is the position of the pushing rod and the actual distance between the electrodes has to be calculated. The ratio between horizontal motion of the electrodes and vertical motion of the pushing rod is known as reduction or attenuation factor $a = \Delta d / \Delta z$, where Δz is the vertical displacement of the pushing rod and Δd is the corresponding horizontal displacement of the electrodes [52, 59]. For lithographically fabricated MCBJ samples typical attenuation factors are $10^{-5} - 10^{-6}$, making the control of inter-electrode distance with sub-angstrom precision possible. Theoretically, the attenuation factor

can be estimated as $a = 6uT/L^2$ [60, 61], where u is the length of the free-standing metallic bridge in the sample, T is the thickness of the flexible substrate, and L is the distance between counter supports (see Fig. 1.1). For our particular geometry, $u \approx 1 \mu\text{m}$, $T = 0.3 \text{ mm}$, $L = 20 \text{ mm}$, which leads to $a \approx 5 \cdot 10^{-6}$. However, it was shown that an actual attenuation factor of MCBJ samples typically is 5–10 times higher, because mechanical and elastic properties of the substrate and especially the polyimide insulating layer deviate from ideal [59, 61].

To estimate the actual attenuation factor experimentally, the tunneling current in the measured traces without molecules is analyzed. For vacuum and low-temperature measurements both opening and closing traces can be taken for this analysis, but for room temperature solvent measurements only opening traces provide proper information. During approaching the electrodes van der Waals interactions between molecules of the solvent and electrodes prevent fast closing of the junctions, i.e. cause repulsion of the electrodes, and the closing traces are typically longer than the opening ones.

Because of sample-to-sample variations during fabrication, the calibration is performed for each measured sample. For every measurement, the sample is first broken in pure solvent, and 50–100 opening-closing cycles are recorded. Only after these solvent measurements the liquid cell is filled with the target molecule solution for further investigations. For all measured traces we determine the conductance range where the current has a tunneling characteristic, typically ($10^{-5.5} G_0$, $10^{-4} G_0$). Then, for every trace we determine the length in this conductance range and deduce the average slope β_{exp} of the tunneling current in the units of z per decade.

Assuming a Simmons model for the tunneling current [62],

$$I \propto \exp\left(-\frac{2}{\hbar} \sqrt{2m\phi} d\right),$$

where $m = 9.1 \cdot 10^{-31} \text{ kg}$ is the mass of an electron, $\phi \approx 4.5 - 5 \text{ eV}$ is the work function of gold, d is the gap size between the electrodes, we can estimate the theoretical decay of the tunneling current:

$$\beta_{\text{theor}} = \frac{\Delta d_{1,2}}{\log(I_1/I_2)} = \frac{\ln 10}{\frac{2}{\hbar} \sqrt{2m\phi}} / \text{dec} \cong 1 \text{ \AA} / \text{dec}.$$

The ratio between this theoretical decay β_{theor} and experimental decay β_{exp} is an attenuation factor.

Example procedure is shown in Figure 1.4. 42 opening conductance traces were measured in pure solvent (Fig. 1.4a). For every trace we determined the length in the conductance range of ($10^{-5.5} G_0$, $10^{-4} G_0$). The distribution of the lengths is shown in Figure 1.4b. From the Gaussian fit of the histogram we deduce the average slope of the traces:

$$\beta_{\text{exp}} = \frac{(2.8 \pm 1.35) \mu\text{m}}{1.5 \text{ dec}} = (1.87 \pm 0.9) \mu\text{m} / \text{dec},$$

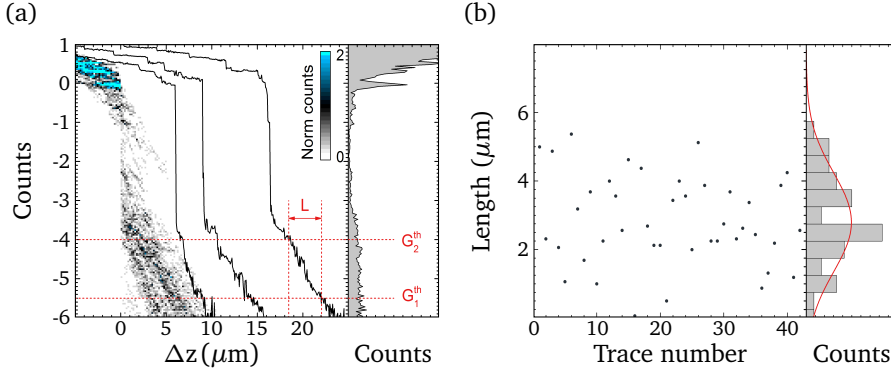


Figure 1.4: Attenuation factor calibration procedure. Conductance traces are measured in pure solvent. (a) Left: conductance–displacement histogram and 3 sample opening conductance traces, shifted horizontally for clarity. Right: conductance histogram. Dashed lines represent threshold conductances $G_1^{\text{th}} = 10^{-5.5} G_0$ and $G_2^{\text{th}} = 10^{-4} G_0$ where the slope of the tunneling current is determined. The trace length L is determined as a trace length between threshold conductances. (b) Scatter plot of all the determined trace lengths in the defined conductance range and the distribution of the lengths. Red curve is a Gaussian fit of the histogram, with $\mu = 2.8 \mu\text{m}$.

therefore, the attenuation factor for this certain sample is:

$$a = \frac{\beta_{\text{theor}}}{\beta_{\text{exp}}} = \frac{1 \text{ \AA/dec}}{1.87 \mu\text{m/dec}} = 5.4 \cdot 10^{-5}.$$

For our samples, attenuation factor varies in the range of $(5 - 8) \times 10^{-5}$.

1.3.6 Plateau length analysis

Additional information about microscopic features of the molecular junction can be extracted from the length of the formed conductance plateaus. The plateau length analysis procedure exploits the same approach as for attenuation factor calibration and requires the following steps:

1. From the conductance histogram the conductance range ($G_1^{\text{th}}, G_2^{\text{th}}$) corresponding to the conductance plateau is defined (Fig. 1.5a).
2. For every trace the length of the trace inside the defined conductance range is determined (Fig. 1.5b, left).
3. Statistical analysis of obtained data is performed. Usually the distribution of trace length is close to normal, so by fitting the distribution to Gaussian,

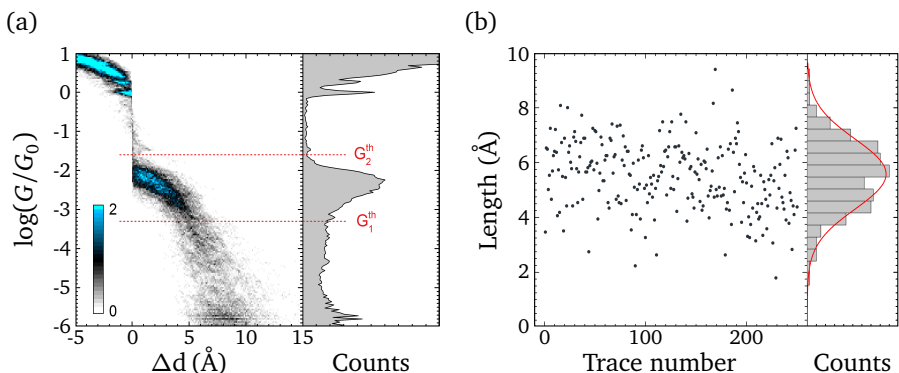


Figure 1.5: Plateau length analysis procedure. (a) Determination of conductance range (G_1^{th} , G_2^{th}) which is considered as conductance plateau. (b) Left: scatter plot of the plateau length for all the traces. Right: distribution of the plateau length. Red line shows the Gaussian fit of the distribution with $\mu = 5.6 \text{ \AA}$.

we deduce the average length of the trace inside plateau conductance range, which we define as plateau length (Fig. 1.5b, right).

1.3.7 Yield of junction formation estimation

Usually, conductance plateau is not observed in all the conductance traces. Therefore, we can define the yield of junction formation as a percentage of the traces where conductance plateau is observed. Here, similar approach to plateau length analysis is also applied.

To estimate the yield, we compare the distribution of traces length for pure solvent measurement and for measurements with the molecule. The trace length is defined as before for the conductance range of $(10^{-5.5} G_0, 10^{-1} G_0)$. For solvent (Fig. 1.6a) and molecule measurements (Fig. 1.6b) we analyze the trace length separately and assuming normal distribution, estimate the parameters of these distributions (mean μ and standard deviation σ). Then, we compare the overlap of normalized fitted distribution curves. We define the yield as a area below molecular curve which does not overlap with the area below solvent curve (Fig. 1.6c).

For sample data, we measured 100 opening conductance traces for the pure solvent and 379 traces for the molecule. The distribution of trace length for the solvent was fitted to Gaussian with the parameters $\mu_s = 3.12 \text{ \AA}$ and $\sigma_s = 1.48 \text{ \AA}$, and for the molecule with the parameters $\mu_{mol} = 10.3 \text{ \AA}$ and $\sigma_{mol} = 3.22 \text{ \AA}$. The

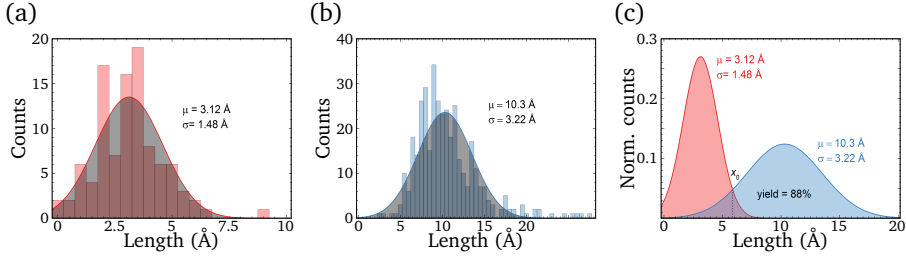


Figure 1.6: Yield of junction formation estimation. For every trace the length is determined in the conductance range of $(10^{-5.5} G_0, 10^{-1} G_0)$. (a) Traces length distribution for pure solvent measurement and Gaussian fit of the distribution. (b) Traces length distribution for the measurements with a molecule and Gaussian fit of the distribution. (c) Normalized Gaussian fitted curves for solvent (red) and for the molecule (blue). The area below molecular curve excluding overlap with the area below solvent curve is considered as an yield of junction formation and equals to 88%.

yield can be calculated as:

$$\begin{aligned}
 \text{Yield} &= \int_{x_0}^{\infty} \mathcal{N}(x; \mu_{\text{mol}}, \sigma_{\text{mol}}) dx - \int_{x_0}^{\infty} \mathcal{N}(x; \mu_s, \sigma_s) dx = \\
 &= \int_{x_0}^{\infty} \mathcal{N}(x; 10.3, 3.22) dx - \int_{x_0}^{\infty} \mathcal{N}(x; 3.12, 1.48) dx = 0.88, \quad (1.4)
 \end{aligned}$$

where $x_0 = 5.9 \text{ \AA}$ is an intersection of solvent and molecular curves and $\mathcal{N}(x; \mu, \sigma) = \frac{1}{\sqrt{2\pi}\sigma} \exp\left(-\frac{(x-\mu)^2}{2\sigma^2}\right)$ is a normal distribution with the parameters μ and σ .

Effect of highly-polar anchor groups on molecular junction formation

Molecular junction is an object which consists of inseparable but usually considerable individually moieties: molecular backbone and linker, or anchor, groups. The design of molecular backbones attracts a lot of interest from synthetic chemists and provides variety of freedom to observe unique features in molecular junctions. Using chemical design, the variety of 'molecular wires' [63] or the molecules with the switching function were synthesized [64–68]. Another field of interest in molecular junctions is the observation of quantum interference [69–73], which is also possible thanks to organic chemistry tools. The main limiting factor of molecular backbone design is the decrease of conductance for more complex molecules, which makes electrical measurements more complicated.

In contrary, not a big diversity of anchor groups exists in investigated molecular junctions. Starting from original paper by Reed *et al.* [27], thiol group is the most often used the the most studied linker for molecular junctions [74, 75]. Due to strong affinity of sulfur to gold, thiol-anchored molecules create covalently bonded molecular junctions which are easy to characterize. Typical widely used non-covalent anchor groups are amino- ($-\text{NH}_2$) [76, 77], cyano- ($-\text{C}\equiv\text{N}$) [78, 79],

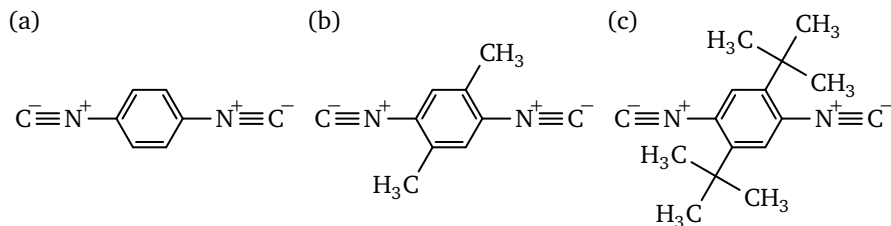


Figure 2.1: Chemical structures of studied molecules. (a) 1,4-benzenediisocyanide, BdNC. (b) 2,5-dimethyl-1,4-benzenediisocyanide, MBdNC. (c) 2,5-di-*tert*-butyl-1,4-benzenediisocyanide, tBuBdNC. Molecules are provided by M. Gantenbein and M. Mayor, Department of Chemistry, University of Basel.

isocyano- ($-\text{N}\equiv\text{C}$) [75, 80] and pyridyl- [13, 29, 64, 81] groups or more exotic isothiocyanates ($-\text{N}=\text{C}=\text{S}$) [82], carboxilates ($-\text{COOH}$) [83]. In this chapter, the family of benzenediisocyanides was studied (Fig. 2.1): 1,4-benzenediisocyanide (BdNC, Fig. 2.1a), 2,5-dimethyl-1,4-benzenediisocyanide (MBdNC, Fig. 2.1b) and 2,5-di-*tert*-butyl-1,4-benzenediisocyanide (tBuBdNC, Fig. 2.1c).

BdNC molecule was studied before by different groups in self-assembled monolayers [84], using MCBJ in high vacuum [85] and with STM-BJ in solution [75, 86]. However, in all the cases the measurements were limited to small conductance range ($G > 10^{-4} G_0$).

All the measurements were performed using MCBJ approach in solution at room temperature (see Chapter 1 for details). The mixture of tetrahydrofuran and mesitylene (1:4 v/v) was used as a solvent.

2.1 Double plateaus in conductance traces

We studied the molecular junctions formed by BdNC molecule (Fig. 2.1a) in liquid environment. 200 conductance traces were measured in 100 μM solution of BdNC. Measured data are presented in Figure 2.2a–e.

Typical opening conductance traces are shown in Figure 2.2a. For all the opening traces we observed the slow decrease of conductance from around $10 G_0$ (bulk gold contact) to G_0 (atomic point contact) with the features of conductance values closes to multiples of G_0 (plateaus with the conductance values of $2 G_0$, $3 G_0$). After the breaking of atomic point contact, sharp drop of conductance by about 2 orders of magnitude is observed, followed by the signature of molecular junction—conductance plateaus (Fig. 2.2a). Surprisingly, two conductance plateaus were observed: high conductance (HC) and low conductance (LC) plateau with the conductances of $\approx 10^{-2} G_0$ and $\approx 10^{-4} G_0$, with clear transition between them. After LC plateau, conductance trace drops below the noise level of the setup.

On the conductance histogram (Fig. 2.2b) two conductance peaks corresponding to plateaus are observed. The conductance values estimated from the Gaussian fit of the peaks, are $10^{-2} G_0$ (FWHM = 0.39) and $2 \cdot 10^{-4} G_0$ (FWHM=0.47) for HC and LC plateau, respectively. On the conductance-displacement histogram (Fig. 2.2c) conductance plateaus are very well separated and slightly slanted. The LC configuration is formed after the rearranging of HC one. The conductance of the first plateau G_{HC} is slightly higher than previously reported measurements of BdNC [75, 86], but comparable to the conductance of similar 1,4-disubstituted benzenes with other anchoring groups [75, 87–90]. Conductance histogram evolution plot (Fig. 2.2d) shows the presence and stability of both plateaus in all the measured traces on the timescale of measurements. The MCBJ device itself is stable in time, demonstrating small drift of a breaking point (Fig. 2.2e).

The same behavior was observed in all the measurements of BdNC molecule (Fig. 2.3a). Two plateaus were present on the conductance histogram as well as on conductance-displacement histogram. The yield of junction formation exceeded 99% for both plateaus (Fig. 2.3b).

In none of the previous measurements of BdNC molecule [75, 84–86] the formation of a low conductance plateau was observed. In the following we argue that this is due to the difference in measurement configurations (namely, us working with individual molecules in solution), although that feature might have been observable in two latter works, had the measurements been performed for conductances lower than $10^{-4} G_0$. Multiple conductance plateaus in traces or multiple peaks in conductance histograms have been observed before for other molecules. Multiple plateaus in a single trace can be attributed, for instance, to multiple molecules in the junction in parallel [87, 91] or different configuration of the molecule in the junction [13, 29, 74, 82, 83, 90, 92]. In the first case, the conductance value are integer multiples of the presumed single molecule conductance, while for the latter, the ratio for the peaks is in the order of 5–20 and needs not be integer. Switching of molecules between different conductance states has been reported before, but such switching requires an external stimuli like UV illumination [64–66, 93] or electrochemical gating [67, 68, 94]. Voltage controlled switching was also observed [19], but it appears at much higher applied voltages (≈ 0.8 V). In these cases the conductance histogram may exhibit two peak values. However, usually these originate from a mixture of traces with the molecule in either one or the other switching state with each individual trace showing just one plateau. Presence of two plateaus in individual traces was also reported [13], but this happened only in 20% of traces. This is in stark contrast to our observation of reproducible formation of double plateaus in the individual traces with almost 100% yield.

The presence of plateaus with larger difference in conductance ($G_{HC}/G_{LC} > 20$) is sometimes explained by intermolecular π – π stacking [81, 95, 96]. BdNC molecule has completely conjugated π -electron system with several possible intermolecular configurations based on stacking (Fig. 2.4).

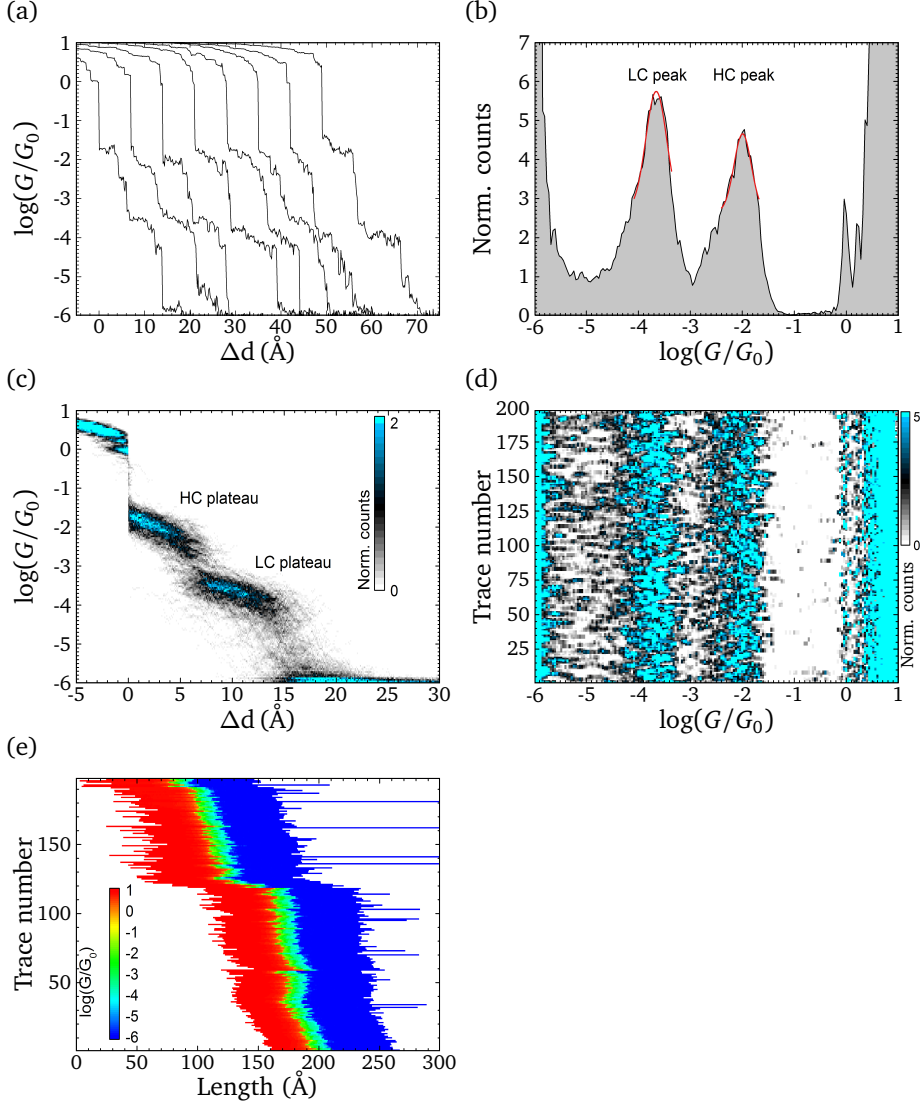


Figure 2.2: Overview of initial BdNC measurements: 200 traces. (a) Typical opening traces, shifted horizontally for clarity. (b) Conductance histogram. (c) Conductance-displacement histogram. (d) Conductance evolution plot. (e) Evolution plot

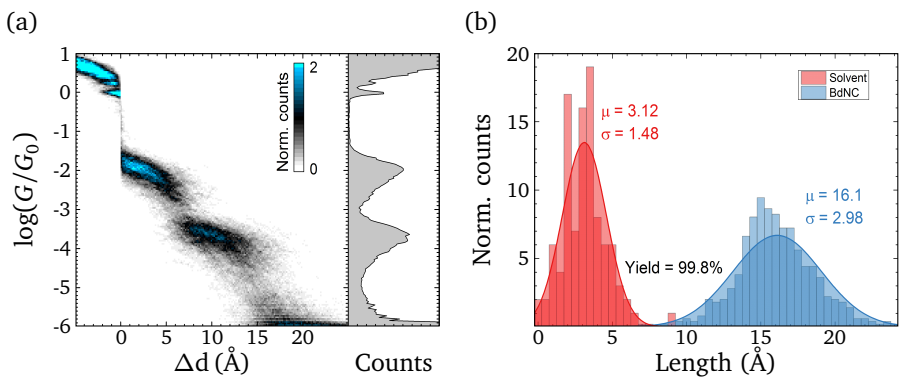


Figure 2.3: Overview of BdNC measurements: 498 traces on 3 different samples. (a) Left: Conductance-displacement histogram. Right: corresponding conductance histogram. (b) Yield of junction formation estimation.

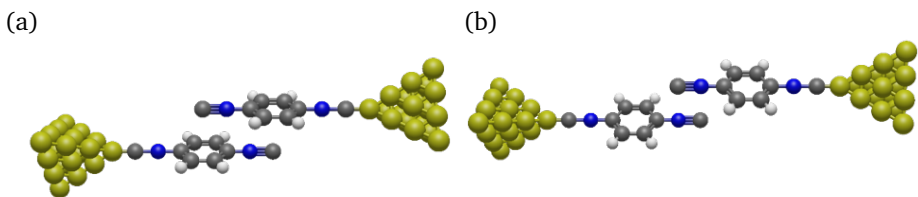


Figure 2.4: Possible configurations of intermolecular dimers formed due to (a) π - π stacking, and (b) dipole-dipole interaction.

2.2 Plateau length analysis

To assess whether this model fits our data we take a new parameter, the plateau length into account.

From conductance histogram we defined plateau as a certain conductance range (see Section 1.3.6 for details). For our data, LC plateau can be determined as a conductance range between $G_1^{\text{th}} = 10^{-4.8} G_0$ and $G_{1,2}^{\text{th}} = 10^{-3.0} G_0$, and HC plateau – as a range between $G_{1,2}^{\text{th}}$ and $G_2^{\text{th}} = 10^{-1.3} G_0$. These threshold conductances are shown in Figure 2.5a with red dashed lines.

The estimated plateau lengths are shown on Figure 2.5a (top panel) and Figure 2.5b. The distributions for both plateaus are close to normal. Deduced from the Gaussian fit of distributions average plateau lengths are 6.5 Å (FWHM = 3.4 Å) and 8.3 Å (FWHM = 4.0 Å) for HC and LC plateau, respectively. The difference in plateau length $L_{\text{LC}} - L_{\text{HC}} = 1.8$ Å is statistically significant: $t(497) = -15.931$, $p < 2.2 \cdot 10^{-16}$ for the paired t-test. 99% confidence interval for the plateau length

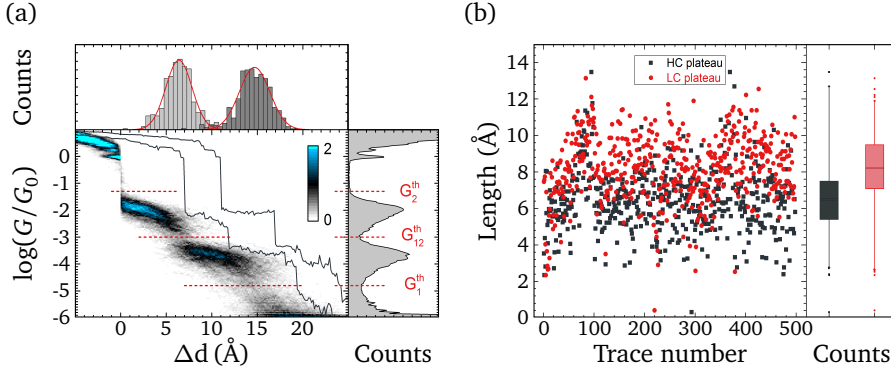


Figure 2.5: Plateau length analysis of 100 μM BdNC solution measurements. (a) Determination of conductance ranges for conductance plateaus. Central panel: conductance-displacement histogram and 2 typical opening traces. Sample traces are shifted horizontally for clarity. Right panel: conductance histogram. Top panel: plateau length histograms. The plateau length is defined as the length of a trace between $G_1^{\text{th}} = 10^{-4.8} G_0$ and $G_{1,2}^{\text{th}} = 10^{-3.0} G_0$ for the LC plateau and between $G_{1,2}^{\text{th}}$ and $G_2^{\text{th}} = 10^{-1.3} G_0$ for the HC plateau. The corresponding threshold conductances (red dashed lines) are deduced from the minima in the conductance histogram. A Gaussian fit of the histograms yields plateau lengths of $L_{\text{HC}} = 6.5 \text{ \AA}$ and $L_{\text{LC}} = 8.3 \text{ \AA}$ for the HC and LC plateau, respectively. The second plateau length histogram is shifted horizontally by $L_{\text{HC}} = 6.5 \text{ \AA}$. (b) Comparison of plateaus length for all the traces. Central panel: scatter plot. Right panel: box plots.

difference is $(1.42 \text{ \AA}, +\infty)$. LC plateau is also longer than the BdNC molecule (C–C distance is 7.9 \AA , estimated in Avogadro-2.0).

For proposed before models based on π – π -stacking the length of the LC plateau is presumed to be shorter than the molecule, and also shorter than the HC plateau, what is in contradiction with the experimental observation.

2.3 Effect of concentration on molecular junction formation

In order to make a complete in-depth study of the concentration effect on the molecular junction formation, we performed concentration evolution measurement. To do that, we started with a pure solvent measurements, and then increased the concentration of BdNC solution *in situ*. We used freshly prepared solvent (a mixture of THF:Mesitylene 1:4 v/v) and 100 nM, 10 μM and 1 mM solutions of BdNC in this solvent.

We started on a clean junction and recorded 50 opening–closing cycles in solvent. Then, a droplet of 100 nM BdNC solution was added into the liquid cell to reach

2. Effect of highly polar anchor groups

10 nM concentration and 100 traces were measured immediately. After recording, the concentration was increased to 1 μM and 100 more traces were measured. On the next step, we sample was cleaned and the same evolution measurements with 1 μM (100 traces) and 100 μM (200 traces) solutions of BdNC were performed. The results of evolution measurements are shown in Figure 2.6.

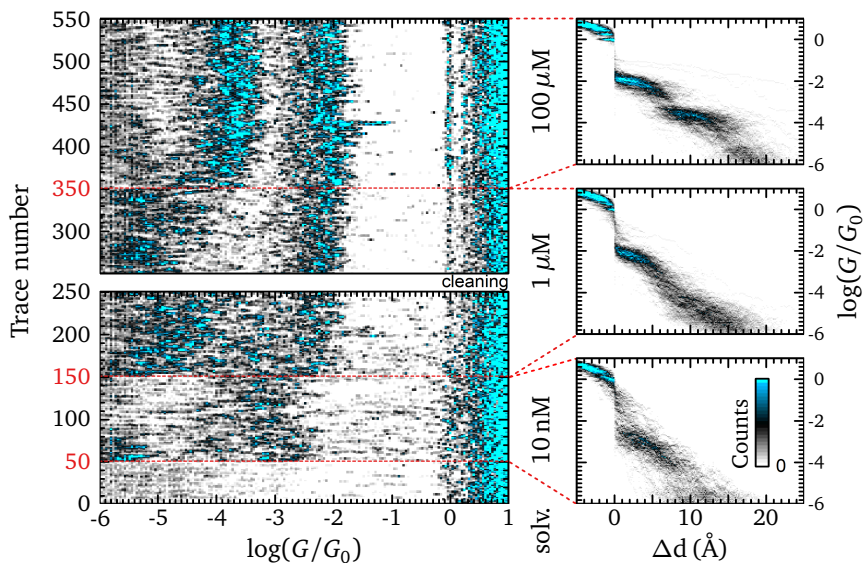


Figure 2.6: Evolution measurements of BdNC. Left panel: histogram evolution plot for the first 250 opening traces (solvent, 10 nM and 1 μM solutions) before junction cleaning and last 300 traces (1 μM and 100 μM solutions) after cleaning. red dashed lines separate regions with different concentrations. Red labels indicate numbers of traces when the concentration was increased. Right panels: corresponding conductance–displacement histograms for 3 different concentrations.

Conductance histogram is changing immediately after increase of concentration, i.e. the processes in solution and on the electrode surface are much faster than the measurement rate.

Two plateaus formation was observed only for 100 μM solution of BdNC. The conductance values, shapes and lengths of both plateaus match very well the plateaus measured without concentration increase (Fig. 2.7c). For 1 μM solution only one plateau is observed. The conductance value deduced from the Gaussian fit of the conductance peak ($G_{1\mu\text{M}} = 10^{-2.3} G_0$, FWHM = 0.53, Fig. 2.7b) is slightly lower than conductance of HC plateau for 100 μM solution. For 10 nM solution also only one plateau is observed with lower conductance: $G_{10\text{nM}} \approx 10^{-3.1} G_0$ (Fig. 2.7a).

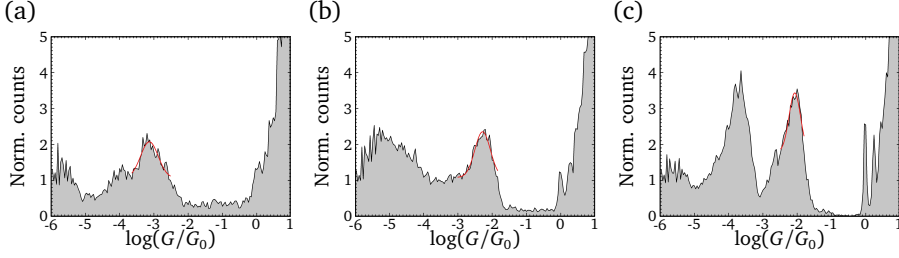


Figure 2.7: Conductance histograms for concentration evolution measurements of BdNC. (a) 10 nM. (b) 1 μ M. (c) 100 μ M. Red curves shows the Gaussian fit of the conductance peaks.

Yield of junction formation is increasing with increase of the concentration (Fig. 2.8):

$$\text{Yield}_{10\text{ nM}} \approx 86\%$$

$$\text{Yield}_{1\text{ }\mu\text{M}} \approx 98\%$$

$$\text{Yield}_{100\text{ }\mu\text{M}} > 99\%$$

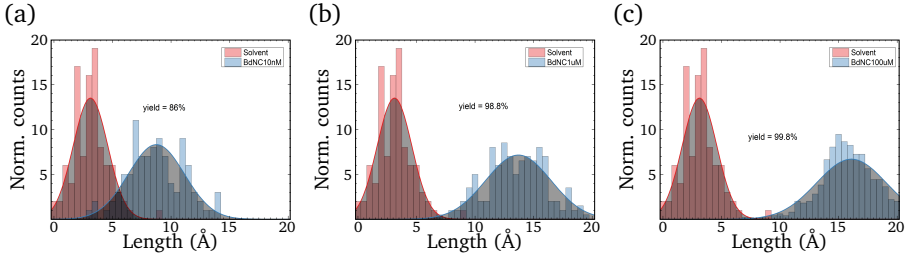


Figure 2.8: Yield of junction formation estimation for: (a) 10 nM, (b) 1 μ M, (c) 100 μ M solutions of BdNC

Clear concentration effect on junction formation is observed in concentration evolution measurements. We assume that for higher concentrations the conductance plateau is initially formed by several molecules in parallel. While the electrodes are withdrawing, the amount of molecules in the junction is decreasing, and only on the tail of the conductance plateau single molecular junction is formed. Conductance value on the tail of conductance plateau for 100 μ M solution measurements as well as for 1 μ M solution is about $10^{-3} G_0$, which is close to the conductance value for the 10 nM solution plateau. This value is also in a good agreement with previously reported conductance value of BdNC molecule measured using STM-BJ approach [75, 86]. Thus, for higher concentrations intermolecular interactions play an important role in molecular junction formation. We can assume that

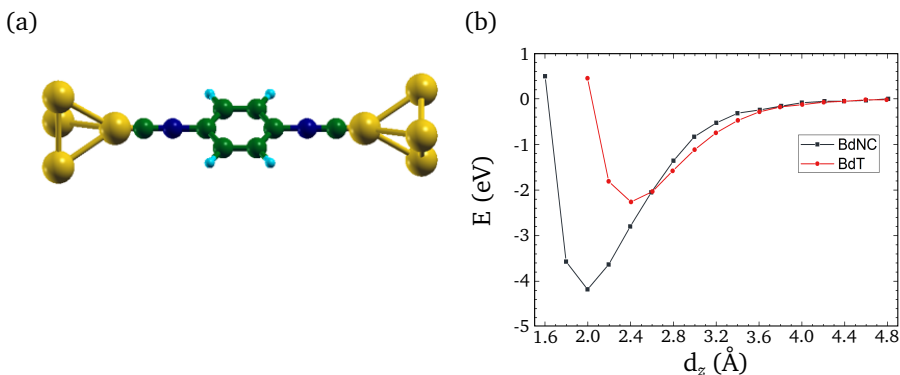


Figure 2.9: (a) Schematics of the configuration for binding energy calculation. (b) Comparison of calculated binding energies to gold electrodes for BdNC (black curve) and 1,4-benzenedithiol (BdT; red curve) molecules.

the formation of LC plateau for 100 μ M solution of BdNC is also mediated by intermolecular interactions.

2.4 Theoretical investigations

To understand the behavior of the molecules on the gold surface, density functional theory (DFT) calculations were performed in collaboration with Jaime Ferrer (University of Oviedo, Spain).

First, the binding energy of BdNC molecule to gold electrodes was studied. The calculation were performed in comparison to mostly studied 1,4-benzenedithiol molecule (BdT). The model configuration for the calculations is presented in Figure 2.9a. Two gold electrodes were simulated as 4-atom pyramids, and the molecule was placed along common z-axis. The distance between apexes of the electrodes is d_z . The binding energy was calculated for every d_z distance with a step of 0.2 Å and shown in Figure 2.9b.

From the calculations we can conclude that the optimal position of the molecule between electrodes corresponds to $d_z^{\text{opt}} = 2.0$ Å, and that isocyano–gold bond is stronger than covalent thiol–gold bond.

Experimental study of the monolayers formed by isocyanides shows that tilting angle of the molecules on the gold surface is around 18°–24° [97]. We also performed theoretical modeling of the single BdNC molecule on the gold surface. For the simulation, the gold surface was limited to five Au(111) layers, and the molecule had two degrees of freedom on the surface: distance to the surface (d_z) and tilting angle (Fig. 2.10a). Calculations were performed for the angles of 0°,

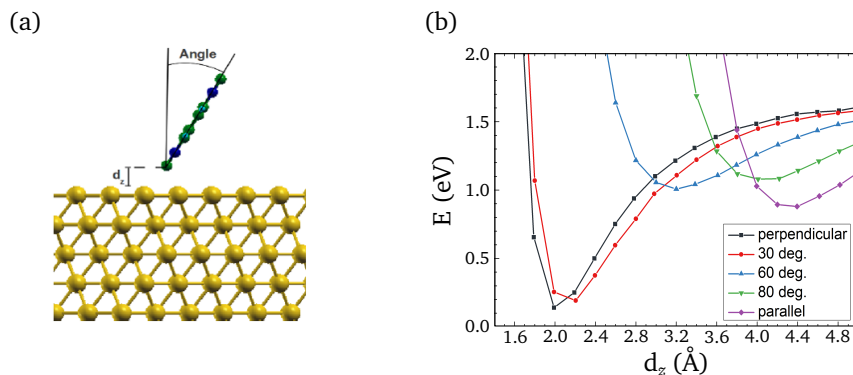


Figure 2.10: (a) Configuration for optimal geometry of the molecule on the gold surface calculation. (b) Calculated dependencies of the energy for different tilting angle.

30°, 60°, 80° and 90° with the step of 0.2 Å for d_z .

Results of the modeling (Fig. 2.10b) show that the optimal tilting angle of BdNC molecule on the gold surface is in the range of 0°–30°. Thereby, independently on the concentration, isocyanide molecules take upright position of the gold surface.

2.5 Closing traces analysis

Usually, only the opening conductance traces are used for molecular junction characterization. The closing traces, i.e. the traces measured during approaching the electrodes, were not studied a lot [98, 99]. Typical application of closing traces analysis is the deduction of the attenuation factor in MCBJ. To do that, measurements without the molecules (e.g. in vacuum, in air or in a pure solvent) are performed. However, close look into these data can provide us with some additional useful information. Here, the closing traces for the same datasets as for opening traces (Fig. 2.11) were analyzed.

Two stable configuration were observed also in the closing traces. While approaching the contacts, first jump to the LC configuration was observed in a conductance trace, followed by the jump to HC configuration. The presence of the intermediate state with the conductance of $\approx 10^{-4} G_0$ is supported by conductance histogram (Fig. 2.11b), conductance-displacement histogram (Fig. 2.11c) and conductance histogram evolution plot (Fig. 2.11d). The latter graph also shows the stability of LC configuration in time, but the yield of LC plateau formation is lower, than for HC plateau in closing traces, and for both plateaus in opening traces. HC plateau is widening in time, this is an evidence of molecule accumulation on the electrode surface. Such behavior is in a good agreement with theoretical calcula-

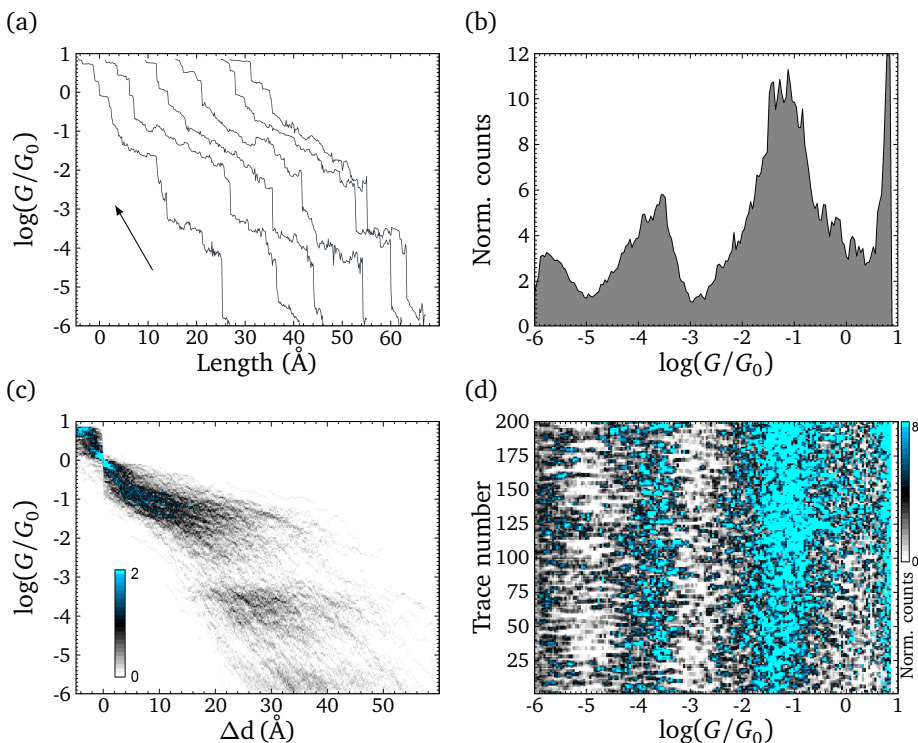


Figure 2.11: Overview of 200 closing traces measured in 100 μM BdNC solution. (a) Typical closing traces. The arrow indicates direction of the traces. (b) Conductance histogram. (c) Conductance-displacement histogram. (d) Histogram evolution plot.

tions: since the molecule takes upright position on the surface, and the interaction energy between isocyano group and gold is high, while approaching the samples the isocyano group can ‘jump’ to the another electrode and form stable molecular junction configuration.

Comparison of the conductance histograms for all measured opening and closing traces shows perfect match for LC peak (Fig. 2.12a), supporting the hypothesis about high stability of LC configuration. Corresponding conductance-displacement histogram is shown in Figure 2.12b. In this graph, all the closing traces were aligned to the $G = 10^{-3} G_0$, which represents a minimum between the conductance peaks in the conductance histogram. Narrow distribution of the points in the range $(10^{-3} G_0, 10^{-1} G_0)$ indicates accumulation of the molecules between the electrodes.

Analysis of closing traces for lower concentrations of BdNC was also performed (Fig. 2.13). For 1 μM solution (Fig. 2.13b) single jump to $G \approx 10^{-2} G_0$ is observed, supporting our hypothesis. For the lowest concentration (10 nM, Fig. 2.13a) the

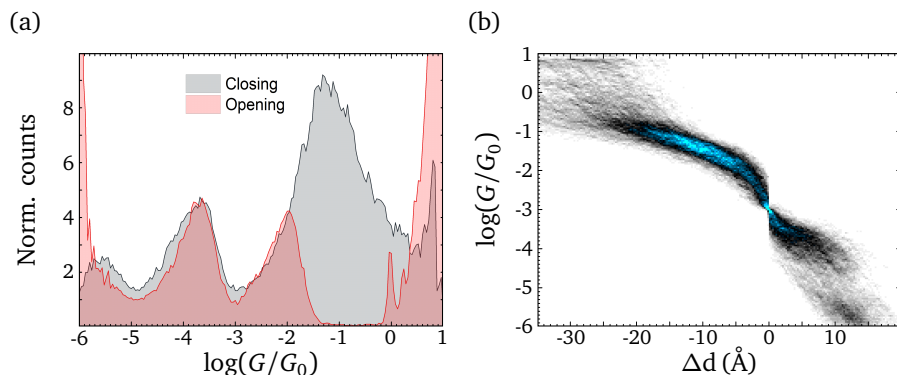


Figure 2.12: Overview of 498 closing traces measured in 100 μM BdNC solution. (a) Conductance histogram. Red curve represents conductance histogram for corresponding opening traces. (b) Conductance-displacement histogram for the traces, aligned at $10^{-3} G_0$.

jumps in a closing traces were also observed, but with significantly lower yield, which can be explained by molecule-solvent interactions in the proximity to the electrode surface.

2.6 Nature of the low-conductance plateau

Due to strong interaction of the molecules with the electrodes in the break junctions, formation of the atomic metal chains was observed for gold [100–103] as well as for another metals [104, 105]. Basing on our studies of plateau length, theoretical studies of isocyano–gold interactions [97], we propose linear chaining of the molecules which involves additional gold atoms into the chain (Fig. 2.14a). The existence of such metal-organic compounds with gold atoms in the linear chain is confirmed by previous studies [106] (Fig. 2.14b). The possibility to involve more gold atoms into the chain is also considered as possible, since the presence of such compounds with aurophilic bonds (Au–Au) was also confirmed by X-ray analysis [107].

2.7 Theoretical analysis of BdNC molecular chains

To check the validity of the model, DFT simulation was performed. First, we studied the electronic structure of the individual BdNC molecule connected to gold pyramids representing the electrodes, and several intermolecular junctions formed by linear chaining of BdNC molecules with 1–2 gold atoms in between (Fig. 2.15).

The calculation shows that the transmission of the chain structure is approximately 2 orders of magnitude lower than the transmission of single molecule

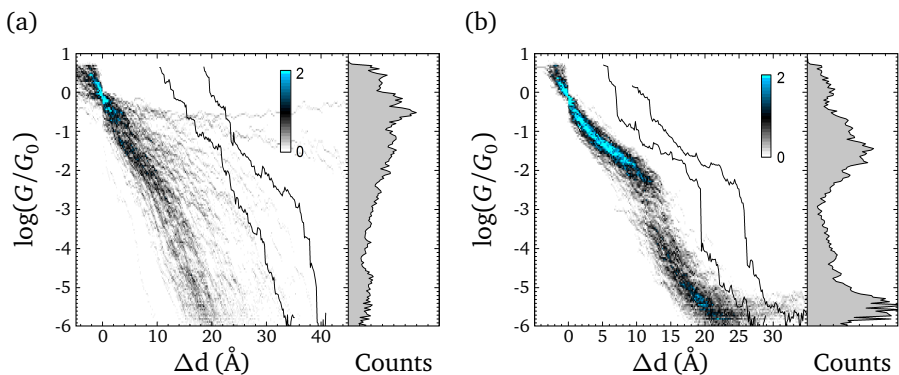


Figure 2.13: Analysis of closing traces for (a) 10 nM and (b) 1 μ M solutions of BdNC. For both graphs: left) conductance–displacement histogram and two typical closing traces; right) corresponding conductance histogram.

junction, what is in a good qualitative agreement with an experimental data.

Using molecular dynamics approach, we modeled behavior of the junction while withdrawing the electrodes if additional molecule is present close to the molecule in the junction. For every point of molecular dynamics trajectory we calculated the conductance, so overall we obtained predicted opening trace (Fig. 2.16). Assuming the pulling of gold atoms from the electrodes by the molecules due to strong polar interaction with isocyano groups as well as chaining of gold atoms, we got qualitative agreement with an experiment: our calculation predicted presence of 2 conductance plateaus with the conductances around $10^{-2} G_0$ and $10^{-4} G_0$.

2.8 Influence of side groups on the molecular junction formation

Another opportunity to check the influence of the surface coverage on the molecular junction formation is to investigate the same isocyano molecule with different side groups. Usually the presence of non-polar alkyl side groups does not influence of the conductance of the molecule [108–110], but big bulky side groups suppress intermolecular interactions.

We studied 2,5-disubstituted derivatives of BdNC: 2,5-dimethyl-1,4-benzenediisocyanide (MBdNC, Fig. 2.1b) and 2,5-di-*tert*-butyl-1,4-benzenediisocyanide (tBuBdNC, Fig. 2.1c).

374 opening traces were measured for 100 μ M solution of MBdNC at two different samples. For opening traces only one conductance plateau was observed (Fig. 2.17a), giving single peak on the conductance histogram (Fig. 2.17b) with the

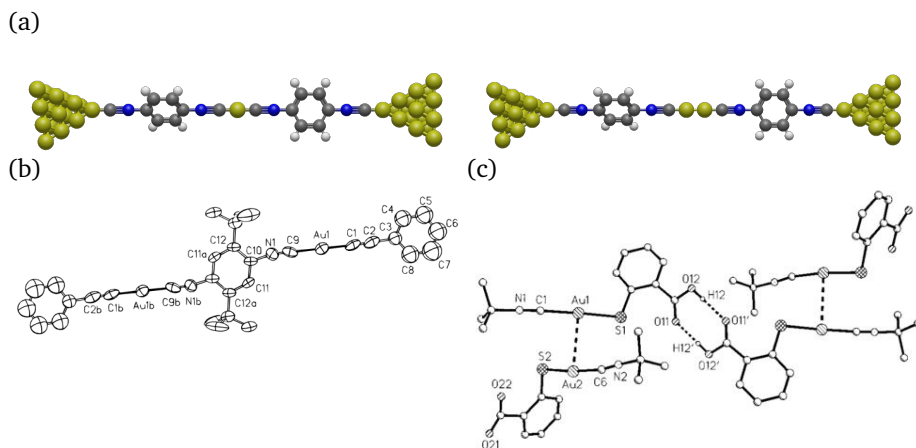


Figure 2.14: (a) Proposed molecular configurations for the LC plateau. (b) X-ray data of the compound with Au atom involved into linear chain with isocyano group. Figure is taken from Irwin *et al.* [106]. (c) X-ray data of the crystal compound with auriophilic bond between gold atoms from Au-isocyano chain. Figure is taken from Schneider *et al.* [107].

conductance value of $G_{\text{MBdNC}}^{\text{opening}} = 10^{-2.3} G_0 = 5 \cdot 10^{-3} G_0$, deduced from the Gaussian fit of the conductance histogram. The plateau on the conductance-displacement histogram (Fig. 2.17c) is slightly curved and has very similar shape to the HC plateau of BdNC. We defined the plateau as a conductance range between $10^{-3.3} G_0$ and $10^{-1.6} G_0$, and estimated average plateau length was 5.8 \AA (Fig. 2.17d). The estimated yield of junction formation reached 86%.

For tBuBdNC molecule 565 opening traces were measured in $100 \mu\text{M}$ solution at two different samples. Only one conductance plateau was observed (Fig. 2.18a, b) with the conductance value of $G_{\text{tBuBdNC}}^{\text{opening}} = 10^{-3.3} G_0 = 5 \cdot 10^{-4} G_0$. Observed conductance plateau is shorter than for BdNC and MBdNC and very slanted (Fig. 2.18c). Using conductance range between $10^{-4.7} G_0$ and $10^{-2.2} G_0$ as conductance thresholds, we estimated plateau length as 4.9 \AA (Fig. 2.18d). The yield of junction formation was only 74%.

Closing traces for MBdNC and tBuBdNC were also analyzed (Fig. 2.19). Clear single jump from the noise level to corresponding G^{opening} conductance values was observed for both molecules, supporting the hypothesis of upright position of the molecules on the surface.

Summarizing, the spatial increase of the molecule size due to side groups has a strong impact on the molecular junction formation. Since this also decreases effective molecular coverage of the surface, and change of a solution concentration leads to similar effect, we can assume that exactly the surface coverage plays the most important role in the formation of isocyanide molecular junctions.

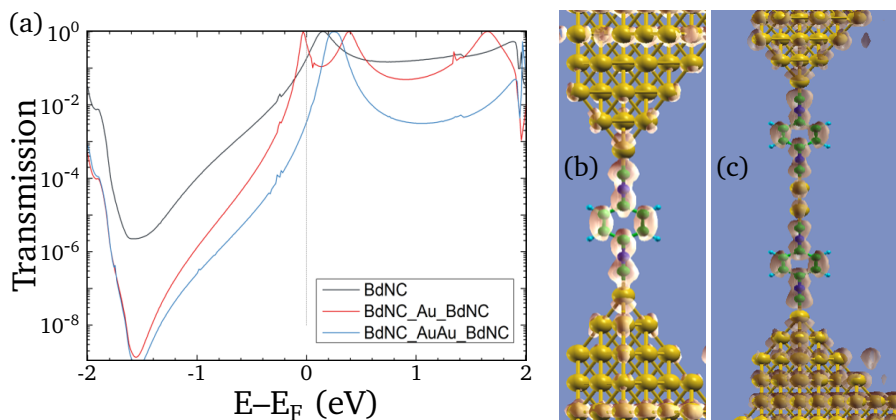


Figure 2.15: (a) Calculated transmissions for single BdNC molecule and for molecular chains with 1 and 2 gold atoms between BdNC molecules. (b, c) Calculated LUMO orbitals for the configurations with one BdNC molecule between the electrodes and for molecular chain with two gold atoms in the chain.

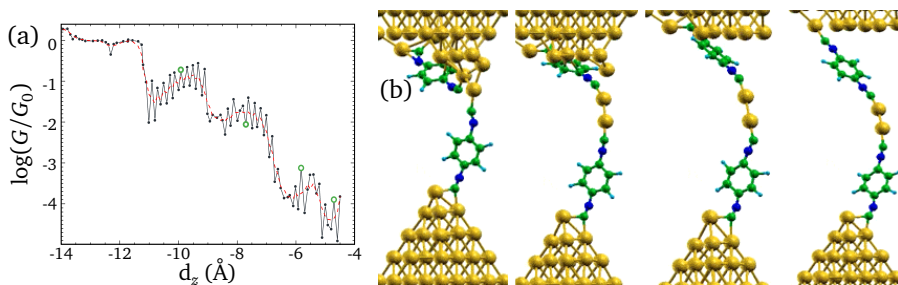


Figure 2.16: (a) Conductance trace calculated for the molecular dynamics trajectory. (b) Snapshots of the molecular dynamics trajectory. The points where snapshots were taken are marked on the conductance trace with green circles.

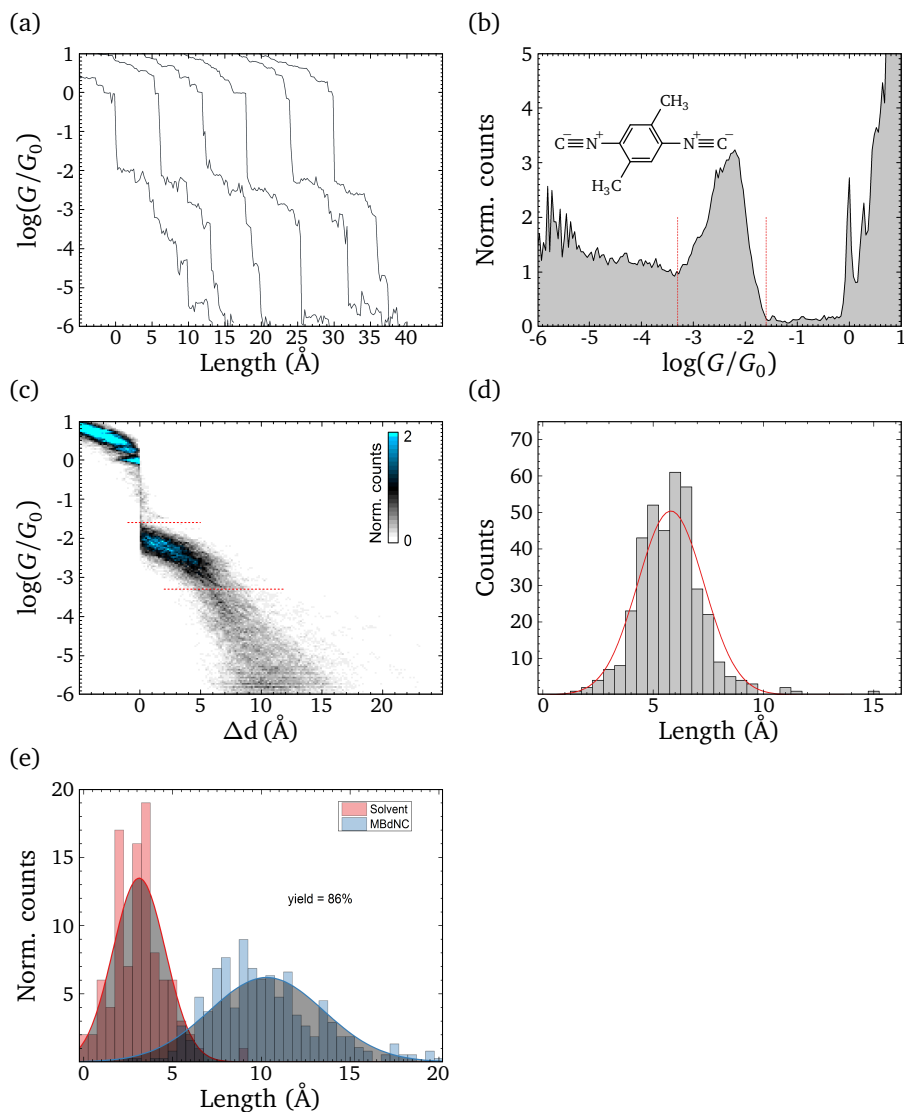


Figure 2.17: Overview of MBdNC measurements. 374 opening traces at 2 different samples. (a) Typical opening traces. (b) Conductance histogram. Red dashed lines represent conductance range defining the plateau: $G_1^{\text{th}} = 10^{-1.6} G_0$ and $G_2^{\text{th}} = 10^{-3.3} G_0$. (c) Conductance-displacement histogram. (d) Plateau length histogram and normal distribution curve. Parameters of the distribution calculated using MLE approach: $\mu = 5.8 \text{\AA}$, $\sigma = 1.5 \text{\AA}$. (e) Junction formation yield estimation.

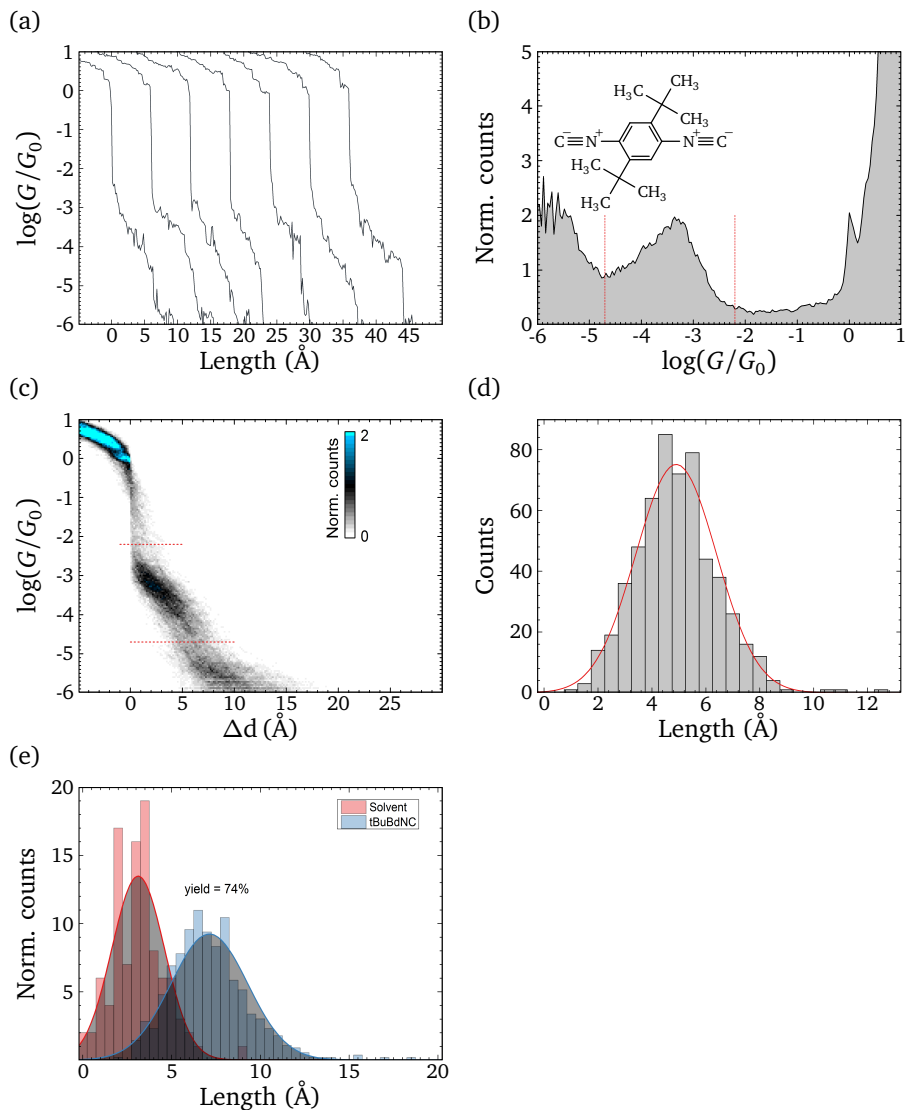


Figure 2.18: Overview of tBuBdNC measurements. 565 opening traces at 2 different samples. (a) Typical opening traces. (b) Conductance histogram. Red dashed lines represent conductance range defining the plateau: $G_1^{\text{th}} = 10^{-2.2} G_0$ and $G_2^{\text{th}} = 10^{-4.7} G_0$. (c) Conductance-displacement histogram. (d) Plateau length histogram and normal distribution curve. Parameters of the distribution calculated using MLE approach: $\mu = 4.9 \text{\AA}$, $\sigma = 1.5 \text{\AA}$. (e) Junction formation yield estimation.

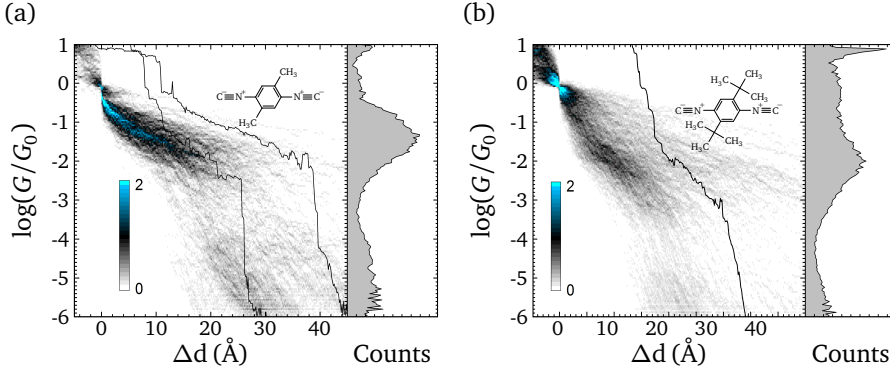


Figure 2.19: Overview of closing traces for MBdNC (a, 374 traces) and tBuBdNC (b, 565 traces). Central panel: conductance-displacement histogram and examples of traces. Right panel: corresponding conductance histogram.

2.9 Asymmetry of conductance peaks

Statistical analysis of conductance traces is a key quantitative approach in single molecule investigations [58, 111]. Usually, the expected value for single molecular conductance is deduced from conductance histogram by fitting the conductance peaks. Typically, fitting to Gaussian or Lorentzian curve is used to fit the histogram in logarithmic axis. Since both Gaussian and Lorentzian curves are symmetric, for the proper fit the conductance peak has to be symmetric too. However, conductance peaks for all measured molecules are asymmetric, therefore the fitting to the symmetric curve is not sufficient.

Two models, explaining asymmetry of the conductance peaks were considered. For the first model, Reuter *et al.* [112] proposed to describe conductance histogram with beta distribution probability function. The shape of the conductance peak can be described as:

$$N_{\text{beta}}(g) \sim \text{Be}(g; \alpha, \beta) = \frac{g^{\alpha-1}(1-g)^{\beta-1}}{B(\alpha, \beta)}, \quad (2.1)$$

where $g = G/G_0$ is the conductance, α and β are two shape parameters of beta distribution, $B(\alpha, \beta)$ is the Euler beta function.

For the second model, Williams and Reuter [113] proposed to explain molecular conductance using single level model [114] with varying parameters. Assuming symmetric coupling of the molecule to both electrodes, in the limits of low bias and low temperature the conductance can be given as:

$$g = G/G_0 = T(E_F) = \frac{\Gamma_R \Gamma_L}{(E_F - \varepsilon)^2 + \left(\frac{\Gamma_R + \Gamma_L}{2}\right)^2} \approx \frac{\Gamma^2}{(E_F - \varepsilon)^2 + \Gamma^2},$$

2. Effect of highly polar anchor groups

where E_F is the Fermi energy, ε is the single molecular level, $\Gamma_{R,L}$ are the couplings of the molecular level to right and left electrode, respectively. $\Gamma \equiv \sqrt{\Gamma_R \Gamma_L}$ is the effective coupling. For their model, Williams and Reuter [113] assumed that both Γ and ε are normally distributed with standard deviations δ_Γ and δ_ε , respectively. The final expression for the conductance peak shape is given by:

$$N_{\text{align}}(g) \sim \frac{c}{\sqrt{8\pi g(1-g)^3}} \exp\left(-\frac{(c\sqrt{g} - d\sqrt{1-g})^2}{2(1-g)}\right), \quad (2.2)$$

where $c \equiv |E_F - \varepsilon|/\delta_\Gamma$ and $d \equiv \Gamma/\delta_\Gamma$.

Since both equations 2.1 and 2.2 describe the conductance histogram in the linear scale of conductance, adopted formulas were used for the fitting of the histograms in the logarithmic scale [58]:

$$N_{\text{beta}}(\log g) = y_0 + A \cdot N_{\text{beta}}(g) \cdot g = y_0 + A \cdot \frac{(10^{\log g})^\alpha (1 - 10^{\log g})^{\beta-1}}{B(\alpha, \beta)} \quad (2.3)$$

and

$$N_{\text{align}}(\log g) = y_0 + A \cdot N_{\text{align}}(g) \cdot g = y_0 + A \cdot \frac{c\sqrt{10^{\log g}}}{\sqrt{8\pi(1 - 10^{\log g})^3}} \exp\left(-\frac{(c\sqrt{10^{\log g}} - d\sqrt{1 - 10^{\log g}})^2}{2(1 - 10^{\log g})}\right), \quad (2.4)$$

where y_0 is the vertical offset and A is the scaling factor.

The analysis of asymmetry was performed for all measured conductance peaks (Fig. 2.20). For the comparison of these models with the ‘conventional’ approach, the fitting to log-normal distribution was also performed for the same datasets. Deduced parameters for all fits are summarized in Table 2.1. For the beta distribution the peak position can be analytically calculated as a mode value of the distribution:

$$\text{mode}_{\text{Be}(\log g; \alpha, \beta)} = \text{mode}_{\text{Be}(g; \alpha+1, \beta)} = \frac{\alpha}{\alpha + \beta - 1}$$

As seen from Table 2.1, r^2 values for both beta distribution model and level alignment model are higher than for log-normal distribution. Therefore, both models are *mathematically* more consistent and can be efficiently used for the asymmetric conductance peaks fitting. However, for the level alignment model deduced parameters d which describe the variation of the electrode coupling Γ are small and not consistent with the model assumptions ($d \gg 0$), especially for 10 nM BdNC and tBuBdNC.

Beta distribution curve with $(\alpha, \beta) > 1$ and $(\alpha, \beta) < 1$ has two qualitatively different behaviors. For our data $\alpha > 1$ for MBdNC and higher concentrations of BdNC, and $\alpha < 1$ for tBuBdNC and 10 nM BdNC. With the previous assumption of

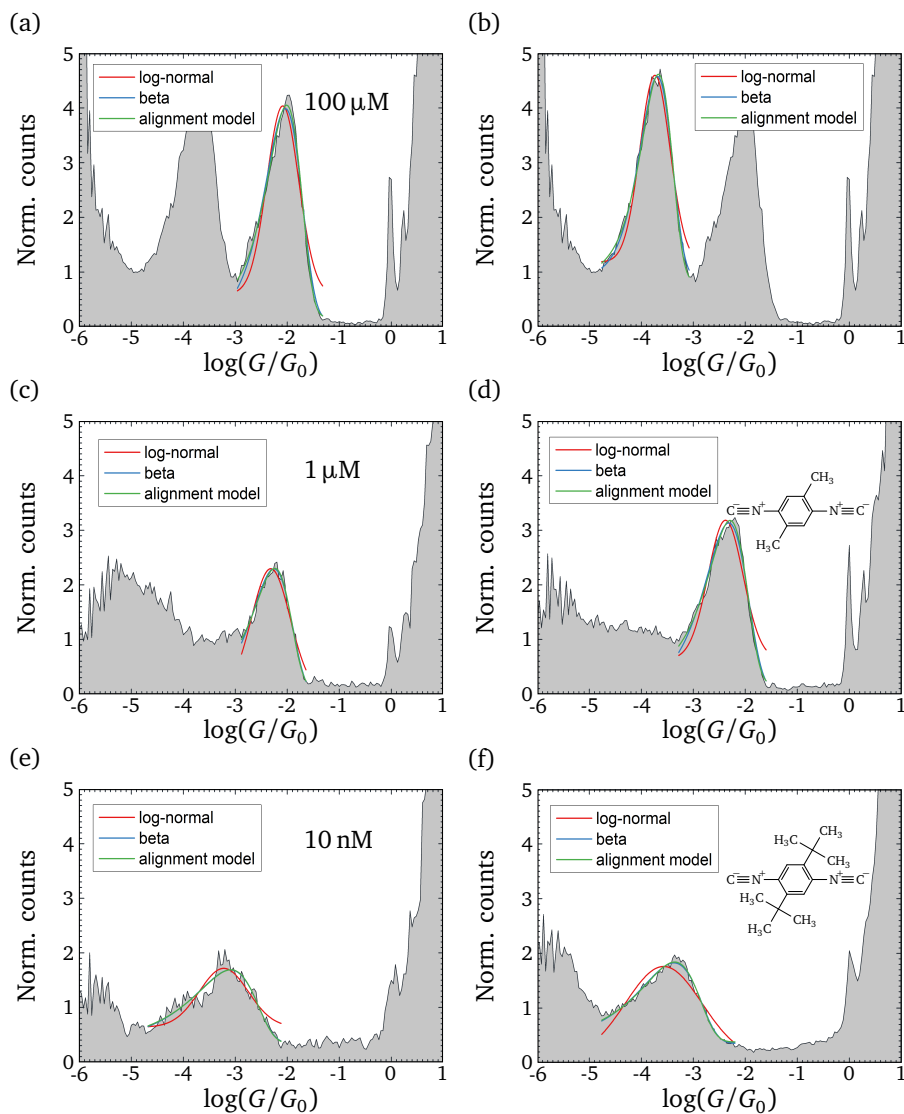


Figure 2.20: Comparison of log-normal distribution fitting (red curves), beta distribution fitting (blue curves) and level alignment model [113] fitting (green curves) of conductance peaks. (a, b) 100 μM BdNC solution, (c) 1 μM BdNC solution, (e) 10 nM BdNC solution, (d) MbNC, (f) tBuBdNC.

2. Effect of highly polar anchor groups

Table 2.1: Parameters of the conductance peak fitting procedures. μ and σ refer to log-normal distribution, α and β to beta distribution [112] (Eq. 2.3), c and d to level alignment model [113] (Eq. 2.4). r^2 values are coefficients of determination for every fit. Standard errors of corresponding values are shown in parentheses.

	BdNC			MBdNC	tBuBdNC	BdNC
	100 μ M	1 μ M	10 nM	100 μ M	100 μ M	LC
μ	-2.08(0.02)	-2.32(0.01)	-3.23(0.03)	-2.38(0.02)	-3.57(0.02)	-3.74(0.01)
σ	0.31(0.03)	0.37(0.02)	0.47(0.05)	0.34(0.03)	0.74(0.1)	0.29(0.01)
r^2	0.88	0.91	0.77	0.87	0.86	0.95
α	1.52(0.1)	1.32(0.2)	0.55(0.1)	1.13(0.1)	0.57(0.03)	1.94(0.1)
β	165(15)	240(30)	680(100)	230(25)	1340(70)	9500(600)
mode	-2.03	-2.26	-3.09	-2.31	-3.38	-3.69
r^2	0.97	0.97	0.87	0.99	0.98	0.99
c	24.5(0.8)	29.3(2)	38.9(7)	28.8(1.2)	58.6(2.5)	185(6)
d	2.01(0.1)	1.78(0.2)	0.22(0.4)	1.58(0.1)	0.41(0.1)	2.34(0.1)
r^2	0.987	0.97	0.87	0.985	0.981	0.99

the multimolecular junction formation at higher concentration and in absence of big side groups, the value of α can be used as a criteria to determine if the molecular junction formed by individual molecule or by several molecules in parallel.

2.10 Analysis of conductance plateaus

To study the influence of the intermolecular interactions on the conductance plateaus shape, the analysis of the plateaus was performed. For every measurement conductance–displacement histogram was fitted to tilted two-dimensional (bivariate) normal distribution:

$$N(x, y) \sim \exp \left(-\frac{\left((x - x_0) \cdot \cos \phi - (y - y_0) \cdot \sin \phi \right)^2}{2\sigma_x^2} - \frac{\left((x - x_0) \cdot \sin \phi + (y - y_0) \cdot \cos \phi \right)^2}{2\sigma_y^2} \right), \quad (2.5)$$

Table 2.2: Parameters of the two-dimensional conductance plateau fit.

Parameter	BdNC			MBdNC	tBuBdNC	BdNC
	100 μM	1 μM	10 nM	100 μM	100 μM	LC
$x_0, \text{\AA}$	2.23	2.4	4.2	2.29	3	10.4
$\sigma_x, \text{\AA}$	3.2	3.0	3.8	3.0	2.6	3.43
$y_0 \equiv \log(G/G_0)$	-2.0	-2.28	-3.2	-2.3	-3.4	-3.75
σ_y	0.24	0.28	0.48	0.27	0.37	0.33
slope, dec/ \AA	0.124	0.17	0.21	0.156	0.27	0.09
decay, $\text{\AA}/\text{dec}$	8.0	5.8	4.8	6.4	3.7	10.9

where $x \equiv \Delta d$, $y \equiv \log(G/G_0)$ and ϕ is the tilting angle. For every plateau (Fig. 2.21) we defined the plateau slope as

$$\text{slope} = \tan \phi.$$

Deduced parameters are summarized in Table 2.2.

The plateau width σ_y and the slope increases with an increase of a side group and a decrease of concentration. This effect can be attributed to the presence of multiple molecules in the junctions. Indeed, several parallel molecules create more stable junction and provide more freedom for its elongation. Thereby, the slope of the conductance plateau can be used as a criteria to determine presence of multiple molecules in the junction.

2.11 Further chaining: 3 molecules?

Our previous results show strong affinity of BdNC molecules in the highly concentrated solution to form linear chains consisting of 2 molecules and 1–2 gold atoms in between. We can, however, also assume the chaining with more than 2 molecules.

Since the conductance ratio between individual molecule (HC plateau) and two-molecule chain (LC plateau) is around 50, we can assume the same ratio for the three-molecule chain. I.e. expected conductance for the proposed structure is $G \approx G_{\text{LC}}/50 = 2 \cdot 10^{-4} G_0/50 = 4 \cdot 10^{-6} G_0$, $\log(G/G_0) = -5.4$. This value is a little above our measurement limit ($10^{-6} G_0$).

Two processes causing third plateau formation while opening the junction are considered: an interaction of double molecular chain with the third molecule on the surface and a breaking of Au–NC or Au–Au bonds in the middle of double molecular chain and interaction of this 2 moieties with extra molecule from the solution. The probabilities of these two processes are defined by the interaction energy for Au–NC

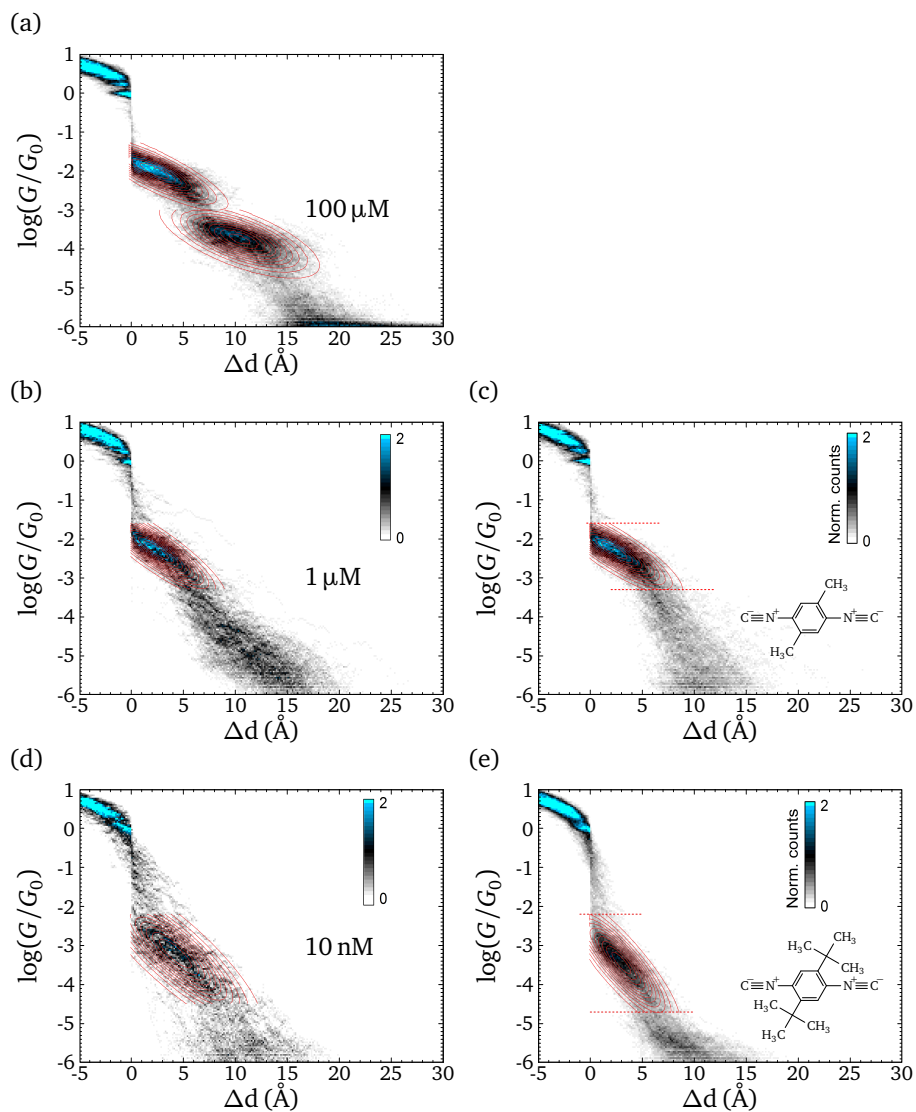


Figure 2.21: Analysis of conductance plateaus. (a, b, d) BdNC 100 μM , 1 μM and 10 nM solutions, respectively. (c) MBdNC. (e) tBuBdNC.

and Au–Au bonds in the chain and on the electrodes. For both processes we could assume much lower yields, than for double molecular chain formation.

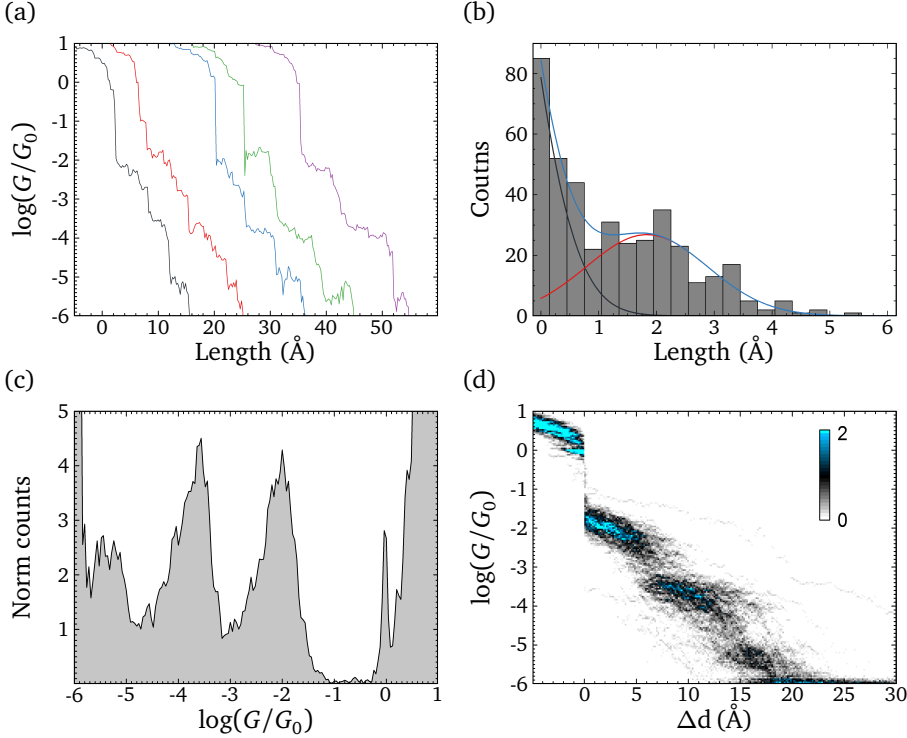


Figure 2.22: ‘Third plateau search’ procedure. (a) Sample traces with the plateau in the defined conductance range ($10^{-5.7} G_0$, $10^{-5.1} G_0$). (b) Distribution of the trace length for this conductance range. The curves show Gaussian fit of two peaks. (c, d) Conductance histogram and conductance displacement histogram for the selected traces, respectively.

We defined ‘third plateau’ conductance range as ($10^{-5.7} G_0$, $10^{-5.1} G_0$). Several traces with existing plateau in this range were observed (Fig. 2.22a). Using length of the trace in this conductance range (Fig. 2.22b) as a criteria for selection, about 25% of traces longer than 2 \AA were extracted. Conductance histogram (Fig. 2.22c) and conductance-displacement histogram (Fig. 2.22d) for selected traces show low yield of third plateau formation, and this plateau is much shorter than LC and HC ones, which supports the previous assumption.

2.12 Current-voltage characterization

Room temperature current-voltage investigation of molecular junctions in solution requires special technique. We proposed to perform such type of measurements in the following way:

1. The junction is being opened much slower than during conductance traces measurements: the speed of pushing rod was set to $5 \mu\text{m/s}$ instead of $31.2 \mu\text{m/s}$.
2. Ramping source-drain voltage is applied continuously: 200 IVs per second with 100 points per IV. The sampling rate is 20 kHz for the voltages up to 2 V.
3. IV converter is working in a manual gain regime without autoranging due to limitations in the bandwidth. Therefore, the IVs can be measured only in the limited conductance range.
4. The conductance is deduced from the linear regime of each measured IV. Conductance trace is reconstructed from all the deduced conductance values.

The corresponding displacement between 2 measured IVs can be estimated as:

$$\Delta D = v^{(\text{push.rod})} \cdot \tau^{(\text{IVtime})} \cdot a^{(\text{att.factor})} = 5 \mu\text{m/s} \cdot 5 \text{ ms} \cdot 10^{-4} = 2.5 \text{ pm} \ll D_{\text{Au}}.$$

So, the configuration of molecular junction is not changing during every individual IV measurement.

An example of IV measurements is shown in Figure 2.23. Measurements were performed in $100 \mu\text{M}$ solution of BdNC with 0.5 V amplitude of ramping voltage.

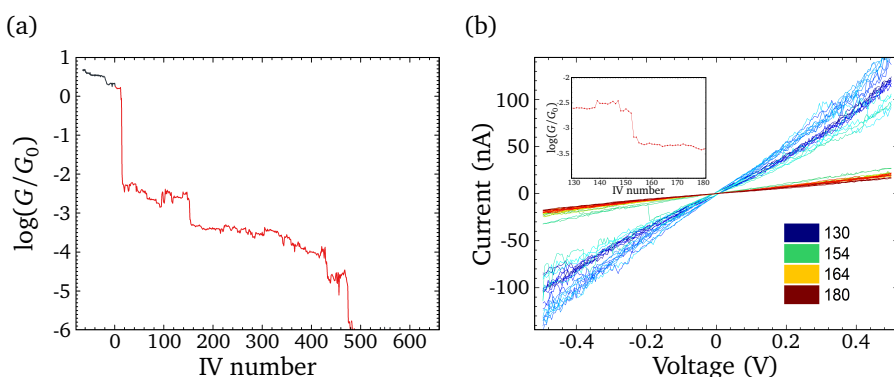


Figure 2.23: IV measurements in $100 \mu\text{M}$ solution of BdNC. (a) Conductance trace reconstructed from linear regime of IVs. (b) Voltage-current characteristic around jump in the conductance trace. Only IVs corresponding to the inset are shown.

The results demonstrate the possibility to measure voltage-current characterization of molecular junctions at room temperature. Despite the high mobility of the molecules in solution, due to high stability of isocyanide molecular junctions IV can be measured along the entire conductance trace from $10^{-2} G_0$ to $10^{-4} G_0$. Sharp transition between conductance states is clearly observed (Fig. 2.23b).

2.13 Conclusion

Non-substituted 1,4-benzenediisocyanide shows unusual molecular junction formation in the liquid environment with two well defined configurations (plateaus) and almost 100% yield. The formation of the second (LC) plateau is strongly concentration- and side group dependent. The linear chaining of the molecules which involves additional gold atoms into the chain was proposed. Validity of this model was supported by DFT calculations. Estimated single molecular conductance value $G \approx 10^{-3} G_0$ is in agreement with previous measurements in STM, but can be observed only in a low concentrated solutions where intermolecular interactions are suppressed.

Interplay between mechanical and electrical properties in π -stacked molecular junctions

In recent years, a few molecular rectifying devices following the original idea of Aviram and Ratner [10] were implemented in SAM [116, 117], in STM geometry in liquid environment [15, 118] and in MCBJ [16, 92]. The key issues of molecular diodes as well as another molecular devices (like switches, transistors etc.) are scalability and the speed. Only recently the molecular diode functioning on GHz frequencies was demonstrated [119]. Another field of possible application molecular electronic devices is the realization the functions which are hardly implemented in CMOS, like molecular muscles or similar electromechanical devices. In all the cases, the question of mechanical stability of the molecules between the electrodes and an influence of mechanical fluctuations on the electrical transport becomes important. In this chapter, the interplay between mechanical and electrical degrees of freedom in π -stacked molecular dimers is studied both experimentally and theoretically.

The results of this chapter were published as a paper Ghane *et al.* [115]

3.1 Studied molecules

As a model molecules, we studied two compounds: the conjugate of cysteamine with naphthalic anhydride (CYS-NA, Fig. 3.1a), and the cysteamine conjugate of pyrene (CYS-PA, Fig. 3.1b). These molecules have π -electron rich ‘core’ and thiol group (SH), separated with short alkyl chain of two and three carbon atoms for CYS-NA and CYS-PA, respectively. We can assume strong binding of thiols to the gold surface and strong π - π interaction between π -electron clouds of two molecules to form molecular bridge between electrodes.

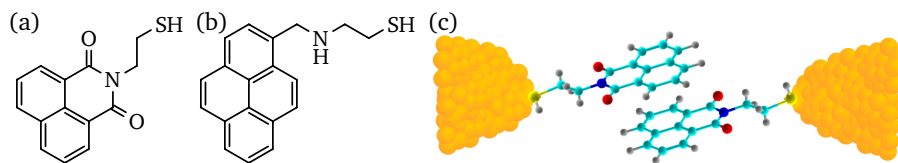


Figure 3.1: (a, b) Chemical formulas of CYS-NA and CYS-PA molecules, respectively. (c) The concept of π -stacked molecular junction formed by two CYS-NA molecule between two gold electrodes.

Short alkyl chains in the studied molecules separate anchor groups from π -electron rich core, but let us expect not very low conductance, which is inherent for saturated alkyl dithiols.

The synthesis of CYS-NA and CYS-PA molecules was performed by Jugun Prakash Chinta in the group of Prof. Shlomo Yitzchaik (Hebrew University of Jerusalem, Israel).

3.2 Electrical characterization

Electrical response in the molecular junctions formed by CYS-NA molecules was first studied using mechanically controlled break junction approach. Since the formation of the intermolecular π -stacked dimers was confirmed by measurements, investigation of electrical properties was also performed in NP array.

3.2.1 CYS-NA measurements in MCBJ

We investigated the stability of molecular dimers formed by CYS-NA molecules using MCBJ approach. We assumed strong interaction between highly π -electron rich moieties of the molecule like observed in simple OPE molecules [120].

The measurements were performed in 100 μ M solution of CYS-NA in the mixture of mesitylene and tetrahydrofuran (4:1 v/v). First, 50 opening-closing cycles were

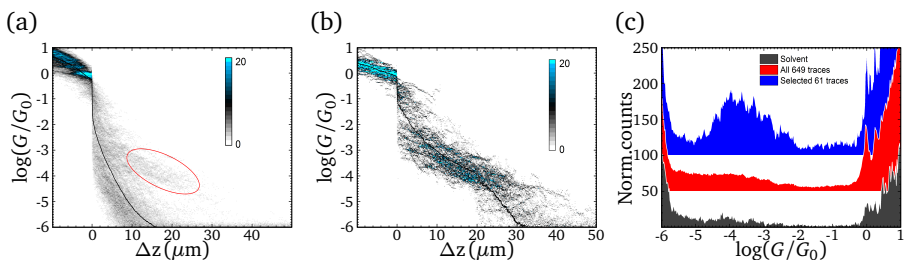


Figure 3.2: (a) Conductance-displacement histogram for 649 traces of CYS-NA measurements. Red ellipse denotes the area which corresponds to junction formation. (b) Conductance-displacement histogram for selected 61 traces. (c) Conductance histograms for pure solvent measurements (dark gray), for all 649 traces (red) and selected 61 traces (blue). Black curves on (a), (b) denote ‘average’ traces by displacement.

recorded for the pure solvent. Then, solvent was replaced with the solution of molecules and as much as possible opening-closing traces were recorded. All the measurements were done with 100 mV bias voltage, 500 Hz sampling rate and the speed of pushing rod of $31.2 \mu\text{m/s}$. Overall, 649 opening-closing cycles were measured on three different samples.

Overview of the opening traces data is shown in Figure 3.2. Conductance-displacement histogram (Fig. 3.2a) does not show clear signature of molecular conductance, which is also supported by the conductance histogram (Fig. 3.2c, red). Only weak signal is visible around the point $(20 \mu\text{m}, 10^{-3.5} G_0)$, marked with red ellipse on the graph. So, only a few traces out of measured 649 are long and can be attributed to molecular junction formation. Using the criteria of length, long traces were selected and analyzed separately. 61 traces matched out length criteria for filtering. Conductance-displacement histogram for these traces is shown in Figure 3.2b. Strong molecular signature can be seen also on the conductance-histogram (Fig. 3.2c, blue).

Thereby, CYS-NA molecules can form relatively stable intermolecular junctions due to π - π interactions. The conductance of such a molecular dimer is around $10^{-4} G_0$. However, the probability of junction formation is very small and only equals to $61/649 = 9\%$.

3.2.2 CYS-NA measurements in NP array

To test intermolecular interactions for CYS-NA molecule on the large scale, we performed measurements in the NP array (nanoparticle self-assembled network, NPSAN, see [121]).

First, NPSAN samples were fabricated using 1-octanethiol covered gold nanoparticles with the diameter of 10 nm (Fig. 3.3a, see Section B.8). Every pair of neighboring gold contact pads and NP array between represents individual two-terminal

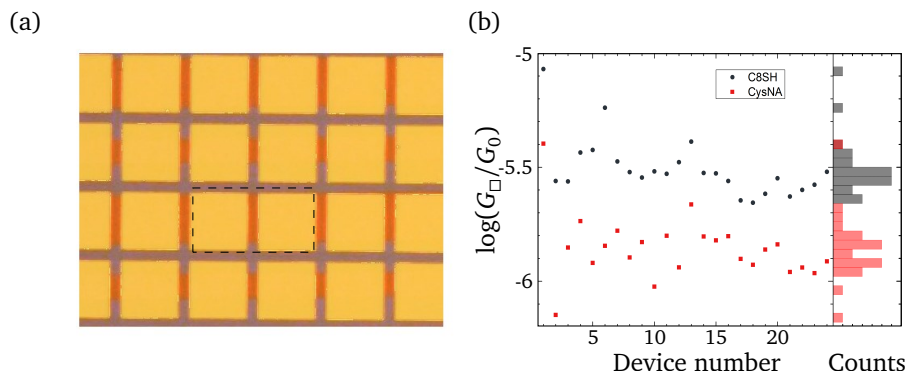


Figure 3.3: (a) Optical image of typical NPSAN sample. Size of gold contact pads is $75 \times 75 \mu\text{m}$, width of NP array lines 29 and $53 \mu\text{m}$. Every pair of neighboring gold contact pads with the NP array in between (e.g., marked with a dashed rectangle) represents individual two-terminal NPSAN device. (b) Conductances of individual NPSAN devices before and after molecular exchange procedure.

NPSAN device. For each device current-voltage characteristic was measured. The amplitude of applied source-drain voltage was 10 V and the sweeping rate 10 V/s.

After initial measurements, molecular exchange procedure was performed [121]. The sample was placed into 10 mM solution of CYS-NA molecule in mesitylene for 24 hours under Ar atmosphere and continuous Ar-bubbling through the solution to prevent oxidation of thiol linker groups. Then, sample was rinsed in the pure mesitylene, dried with N_2 and IV characteristics were measured for the same two-terminal devices. As shown before, in NPSAN the sheet conductance is comparable with the conductance of individual molecular junction, measured in MCBJ [121]. Thus, expected value of the sheet conductance for NPSAN with CYS-NA molecules is about $10^{-4} G_0$.

The comparison of sheet conductances before and after molecular exchange is shown in Figure 3.3b. The figure shows that the conductance of every two-terminal NPSAN devices decreased after exchange. This means that the molecular exchange procedure is not efficient, most probably due to small length of the molecular dimer. In other words, the dimer formed by two CYS-NA molecules is too short to bridge the gap between neighboring nanoparticles (which is 1.8 nm).

3.2.3 CYS-PA measurements

Electrical characterization of CYS-PA molecule was performed using MCBJ approach. Measurements were done in the $100 \mu\text{M}$ solution of CYS-PA in dimethylsulfoxide (DMSO). In all the measured traces, after the breaking of gold-gold contact, sharp drop to the conductance of $10^{-4} G_0$ is observed, followed by the long tail (Fig. 3.4).

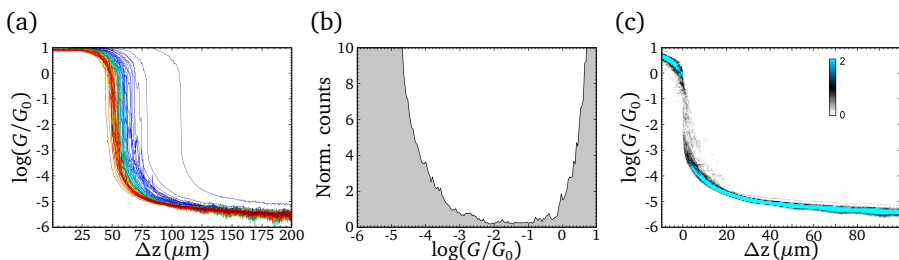


Figure 3.4: CYS-PA measurements. (a) Conductance traces. (b) Conductance histogram. (c) Conductance-displacement histogram.

The formation of individual molecular junctions was not observed. Possible explanation of such behavior is a very strong affinity of CYS-PA molecules to form intermolecular π - π stacks as well as stacks on the gold surface. These molecules form continuous film on the gold electrodes which prevents proper opening of the junction.

3.3 Theoretical investigations

To study the dynamics of geometrical configurations of the intermolecular dimers and its influence on the mechanical stability and electrical properties of the molecular dimer, density-functional theory (DFT) calculations were performed. In general, the theoretical approach includes the following steps:

- geometry optimization of single molecule junctions;
- classical molecular dynamics simulations, i.e. calculation of molecular dynamics trajectories;
- calculation of energy- and time-dependent linear conductance $G(t, E)$ along the corresponding molecular dynamics trajectory.

3.3.1 Geometry optimization

First, DFT calculations were performed to calculate electronic structure and optimized geometry for individual CYS-NA and CYS-PA molecules and for π -stacked dimers chemisorbed on Au(111) surfaces via thiol linkers. To model the Au (111) surface, three gold layers were used, and all the atoms of the first layer were allowed to relax.

Isolated π -stacked molecules

The minimum energy configurations for the π -stacked molecules were calculated using a hybrid Gaussian plane-wave (GPW) method as implemented in the CP2K code with a triple- ζ valence doubly polarized (TZV2P) basis set. The molecular geometries for both dimers are depicted in Figure 3.5(a–d). The corresponding electronic structures for these configurations are shown in Figure 3.5(e, f). For both dimers the highest-occupied (HOMO) and lowest-unoccupied (LUMO) molecular orbital densities are mostly concentrated over the pyrene core with a very low weight on the terminal sulfur atoms, and a HOMO-LUMO gaps are similar, ~ 2.1 eV.

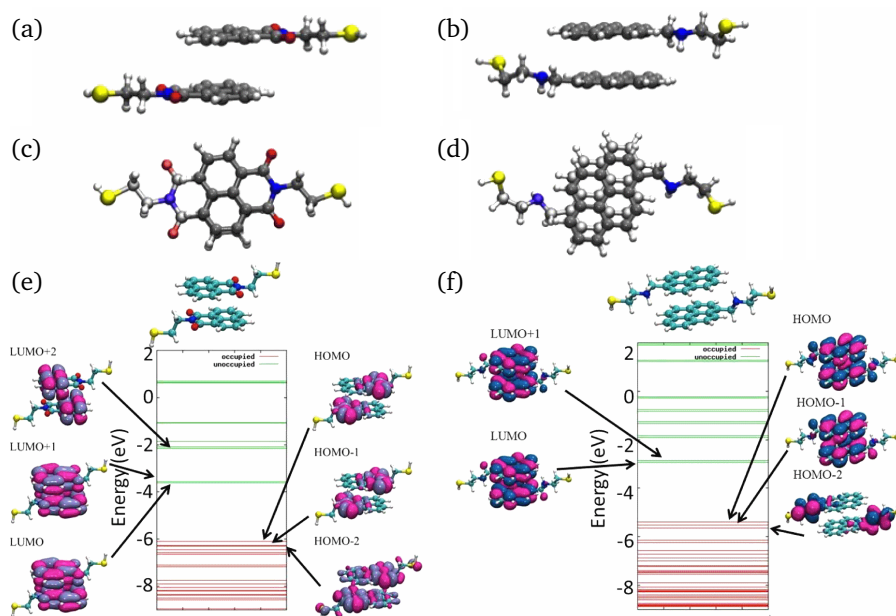


Figure 3.5: (a, c) Side- and top-view of the optimized geometrical structure of molecular dimer, formed by two CYS-NA molecules. (b, d) Side- and top-view of the optimized geometrical structure of molecular dimer, formed by two CYS-PA molecules. (e, f) Calculated electronic structure and several molecular orbitals, closer to LUMO and HOMO levels, for CYS-NA and CYS-PA dimers, respectively. Figure is adapted from Ghane *et al.* [115].

Molecules on Au(111) surface

Since the electronic structure can change upon chemisorption of the molecule on the gold surface, the configurations of molecular dimers sandwiched between gold electrodes were built and optimized (Fig. 3.6a–b).

3. Properties of π -stacked molecular junctions

Table 3.1: Calculated parameters of the most energetically favorable configurations of CYS-NA and CYS-PA molecules on the gold surface. h_s is a distance between S atom and Au(111) surface, $\theta_{\text{Au-S}}$ is Au-S bond angle with respect to the Au surface, $r_{\text{Au-S}}$ is Au-S distance.

	CYS-PA			CYS-NA		
Package	h_s (Å)	$\theta_{\text{Au-S}}$ (deg)	$r_{\text{Au-S}}$ (Å)	h_s (Å)	$\theta_{\text{Au-S}}$ (deg)	$r_{\text{Au-S}}$ (Å)
CP2K	1.94	51.68	2.53	1.86	54.34	2.57
Gromacs	2.41	59.59	2.41	2.42	59.71	2.94

The calculations show that the hollow site is more energetically favorable for both molecules (see Table 3.1). Calculated charge density plots of the HOMO and LUMO orbitals are shown in Figure 3.6(c, d). The highest density weight occurs on the aromatic rings for both dimers (similar to the isolated molecules), but also contributions from the sulfur states hybridized with the gold surface states do also emerge due to coupling to the substrate. This additional electron density delocalization can open charge transport pathways through the molecular system.

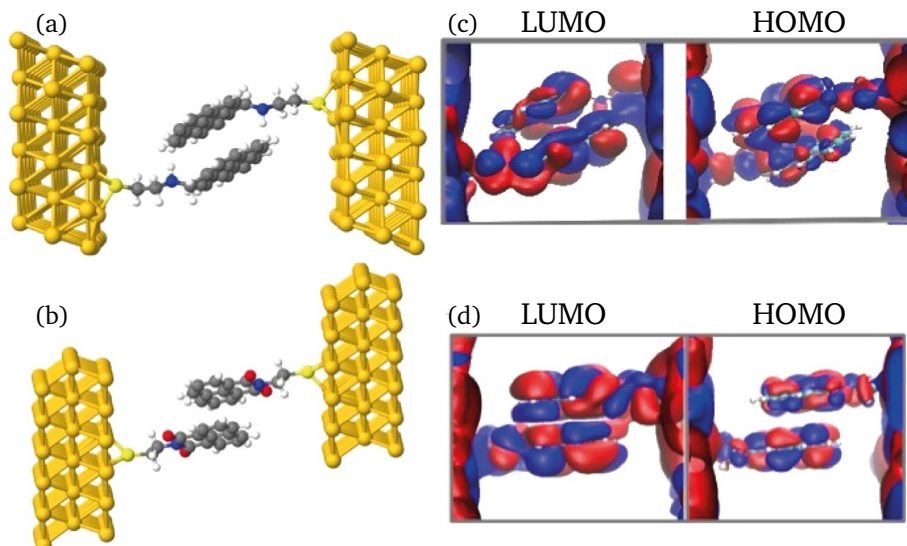


Figure 3.6: (a, b) Two possible optimized molecular arrangements considered for studying the electrical transport properties of the π -stacked dimers of (a) CYS-PA and (b) CYS-NA sandwiched between two gold electrodes. (c, d) Corresponding charge density plots of the LUMO and HOMO orbitals. Figure is adapted from Ghane *et al.* [115].

3.3.2 Classical molecular dynamics

Molecular dynamics (MD) simulations were performed using the Gromacs package [122] with a time step of 1 fs. To simulate a gold surface, a gold slab with a size of $48 \times 55 \text{ \AA}^2$ and five atomic layers thick was used. The temperature of gold electrodes was kept at 300 K, while the temperature for the molecules was decreased from starting temperature of 200 K to 1 K. Since no slow (a few ns) conformational changes were observed in the trajectories, the snapshots for the transport calculations were collected only over the first 3 ns, shown in Figure 3.7. This figure qualitatively illustrates the mechanical stability of both molecular junctions during the simulation time. An important variable when studying the motion of a molecule attached to a surface is the local conformational dynamics of the linkers since they build the bottleneck for charge transport. Thus, e.g., conductance switching can be induced by stochastic fluctuations of the interfacial bonds [12]. Figure 3.8a shows the trajectory path of a sulfur atom and the nearest gold atom for the left and right electrodes. Surprisingly, the stochastic motion of sulfur atom for CYS-NA molecule is significantly smaller than for CYS-PA, despite the larger π -stacked system in the latter molecule. The distribution of the distances between two carbon atoms belonging to opposite π -stacked aromatic rings (Fig. 3.8b) is also broader for CYS-PA. We surmise that the stronger fluctuations of the aromatic rings together with the longer side chains in the CYS-PA dimer may be responsible for the stronger stochastic motion of the sulfur atom on the surface when compared with the CYS-NA dimer.

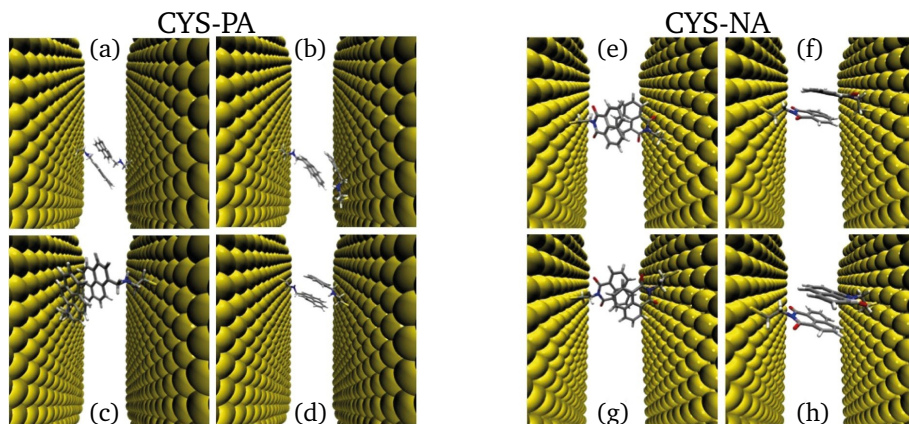


Figure 3.7: Snapshots from a molecular dynamics run for the CYS-PA (a–d) and CYS-NA (e–h) molecular junctions. In both cases, panels display molecular conformations taken at (a, e) 0 ns, (b, f) 1 ns, (c, g) 2 ns, and (d, h) 3 ns. Figure is adapted from Ghane *et al.* [115].

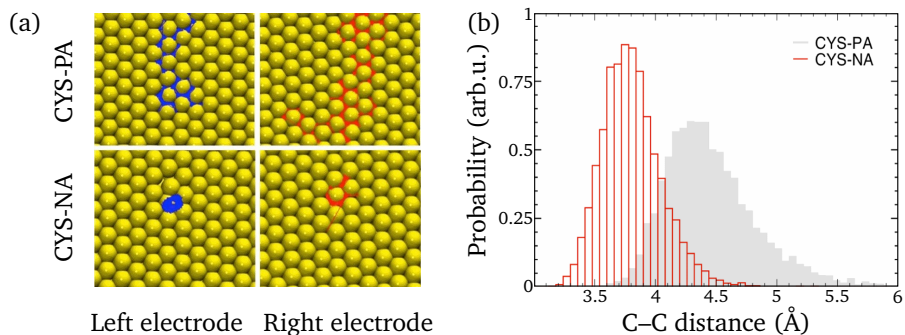


Figure 3.8: (a) Surface trajectories of the sulfur atom on the left and right electrodes for both CYS-PA and CYS-NA molecular junctions. (b) Distribution of the distances between two carbon atoms in the aromatic rings in dimers during 3 ns MD simulations. The gray histogram shows the results correspond to the CYS-PA dimer, while the red one presents the results related to the CYS-NA dimer. Figure is adapted from Ghane *et al.* [115].

3.3.3 Modeling of electrical response

The electrical response of the single molecule is the energy-dependent linear conductance G . In case of coherent transport, the conductance is defined by the Landauer formula: $G = \frac{2e^2}{h} T(E)$, where $T(E)$ is the quantum mechanical transmission probability of the molecular junction.

In order to examine the relationship between molecular conformation and transport characteristics, the electronic structure and the corresponding energy-dependent quantum mechanical transmission function $T(E, t_j)$ were calculated for every snapshot along the MD trajectory. The calculations were performed for two time scales: (i) short time window, with 100 snapshots extracted every 1 ps, and (ii) long time window, with 100 snapshots extracted every 30 ps. The results for both molecular junctions are shown in Figure 3.9. The bunch of red curves corresponds to the time-resolved transmission functions. Additionally, the time average transmission (blue curves) as well as the transmission function of the static molecular junctions (green curves) are shown for comparison.

For both molecules short- and long-time windows demonstrate roughly the same quantitative results in terms of the time average transmission, while the difference is visible only in a very specific energy windows. Since only the low-energy behavior (around Fermi level) is relevant for the linear transport, the differences in transmission for short- and long-time windows are negligible. Therefore, only short-time results (Fig. 3.9a, b) are further analyzed.

Fluctuations in the dimers lead to an increase of the transmission function for non-resonant tunneling, especially for CYS-NA molecule (Fig. 3.9c), where the time average transmission is roughly 1–3 orders of magnitude larger than the static

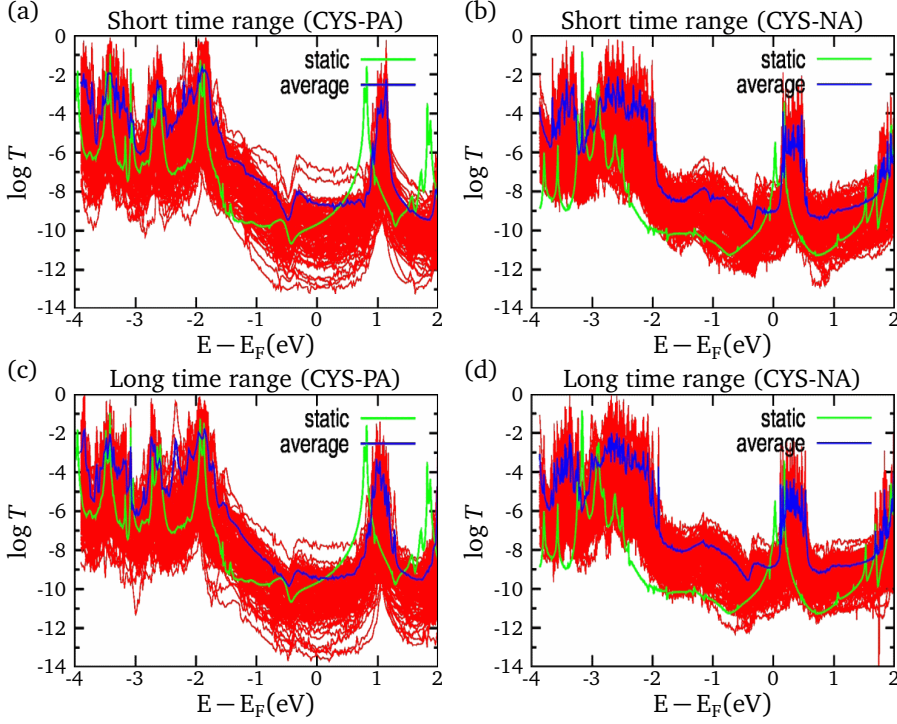


Figure 3.9: Red: transmission functions for molecular dimers, calculated over simulation time. Short time range: 100 snapshots every 1 ps, long time range: 100 snapshots every 30 ps. Blue curves represent the time-average transmission function, and green curves denote the transmission function for the static configuration. Figure is adapted from Ghane *et al.* [115].

one. Energy levels are also shifted (e.g., the orbitals above the Fermi level). Such energy shifts induced by the average influence of the dynamics which modulates the electrode-molecule coupling. The variations of the transmission function are larger for CYS-PA molecule, which is in a good agreement with Figure 3.8b. Figure 3.10 shows the log-normal histograms of the transmission functions at the Fermi energy E_F . The variations of the conductance at the Fermi energy for the CYS-PA junction cover around 5 orders of magnitude, which is about 2–3 orders of magnitude larger than for the CYS-NA junction. This difference is most likely related to the different dynamical behavior of the sulfur linkers as well as to the stronger fluctuating π – π coupling as previously discussed (Fig. 3.8).

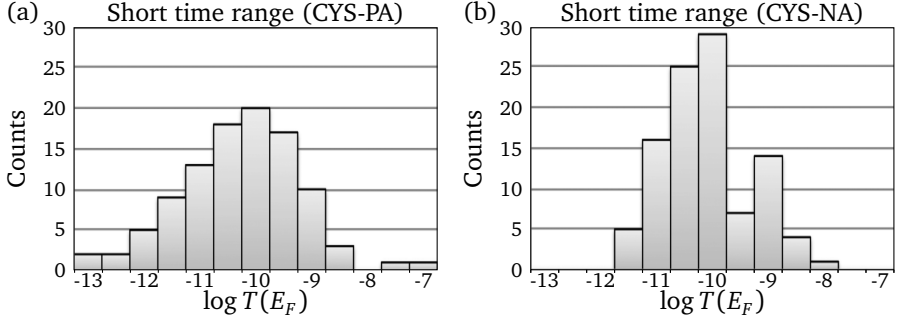


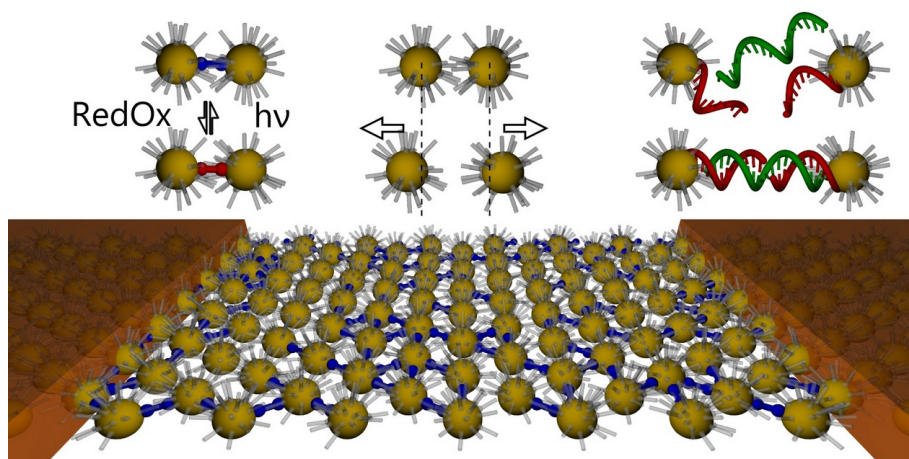
Figure 3.10: Log-normal histograms of the transmission function at the Fermi energy E_F as built from the time series for (a) CYS-PA molecule and (b) CYS-NA molecule. Only short-time series are displayed (cf. Fig 3.9a, b). Figure is adapted from Ghane *et al.* [115].

3.4 Overview of experimental and theoretical results

Both experiment and calculation demonstrate stability of the molecular dimer formed by CYS-NA molecules to bridge gold electrodes and to form molecular junction. Surprisingly, fluctuations in the molecular dimers can cause significant increase in conductance in comparison to the static configuration. Additionally, the stability of CYS-NA molecular dimer is higher than CYS-PA, despite larger π -electron overlap for the latter. However, predicted transmission value for CYS-NA dimer (Fig. 3.10c–d) is significantly lower than observed experimentally (Fig. 3.2b–c). Such a difference can be related to the problem of precise Fermi energy level computation. Fermi energy lies close to the series of calculated resonances in the transmission function (Fig. 3.9c–d). Hence, even very small shift in E_F could lead to the increase of transmission by a few orders of magnitude. Another reason of the discrepancies is an influence of the solvent which was not taken into consideration [123].

Part II

Molecular networks



Nanoparticle arrays as a platform for molecular electronics

Nowadays a lot of organic-based devices are available on the market. First of all, the displays based on organic light-emittive diodes (OLED) present in the consumer electronics for a long time. Recent advances on the growing market of wearable electronics require new approaches to fabricate electronic devices. These devices have to be stable in the much wider environmental conditions than conventional solid-state electronics, have necessary functionality, be cheap in production. One attractive branch of wearable devices is flexible electronics. Existing semiconductor technology can not completely satisfy all these requirements.

Conductive polymers, one candidate to function in the flexible electronics, are the parts of expanded rapidly in the recent year field of organic electronics. Till now, a lot of 'conventional' electronic devices were also implemented using organic polymers, like OLED, organic field-effect transistor (OFET), organic solar cell etc. All these devices function on the level of molecular assembly. As it was shown in the previous chapters, a lot of functionality can be also achieved on the level of

This chapter is based on the review [124].

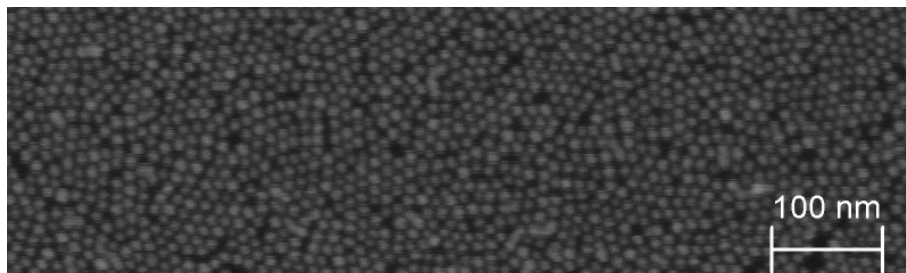


Figure 4.1: SEM image of nanoparticle array formed by gold nanoparticles with the average diameter of 10 nm, covered with 1-octanethiol organic shell.

individual molecules. Existing approaches for single molecule characterization do not have scalability which is required for the actual single-molecule based devices. One promising platform for single molecule junction upscaling is an array of metallic nanoparticles.

Two-dimensional arrays of metallic nanoparticles (or, simply, nanoparticle array, NPA) represent a useful template to create network of molecular junctions, where nanoparticles act like the electrodes which are interconnected by molecules.

4.1 Fabrication techniques

To fabricate two-dimensional nanoparticle arrays, a variety of techniques were developed, including drying-mediated assembly, Langmuir-Blodgett technique and drying-mediated technique on the water surface. The latter approach is a simplest way to fabricate densely packed monolayers of nanoparticles.

The fabrication starts with a synthesis of gold nanoparticles with desired size, followed by the encapsulating of thiol molecules. This organic shell prevents aggregation of the nanoparticles, and also works as a tunneling barrier for the charge transport between neighboring nanoparticles. To form an array, small amount of thiol-covered nanoparticle solution (in chloroform CHCl_3 , dichloromethane CH_2Cl_2 etc.) is transferred on the water surface (see B.5). During evaporation of the solvent, nanoparticles are self-assembled into densely packed array with triangular geometry (Fig. 4.1). By selection the thiol-terminated ligands with different molecular length, the interparticle distance can be adjusted in the wide range between 1.2 and 2.3 nm for 1-alkylthiols and even more for more complex molecules.

To fabricate the device suitable for electrical investigations the NP array is transferred on the Si/SiO_2 substrate using microcontact printing approach, followed by the evaporation of the metallic (usually, Ti/Au) contact pads using TEM grid as a shadow mask. Typically, the NP array is stamped in the shape of stripes 10–60 μm in width. The contact pads are separated by 8–20 μm (Fig. 4.2a).

current can be expressed as [128, 129]:

$$I \propto V_{\text{jct}} \sum_j \left(\frac{h}{e^2 R_T} \right)^j \left(\frac{k_B^2 T^2 + e^2 V_{\text{jct}}^2}{E_C^2} \right)^{j-1} \exp \left(-\frac{E_C/j - jeV_{\text{jct}}}{k_B T} \right), \quad (4.1)$$

where R_T is the resistance of the single junction, k_B is Boltzmann constant, T is the temperature, V_{jct} is a voltage drop over a single tunnel junction (i.e., $V_{\text{jct}} = V/N$).

For different voltage regimes, the Equation 4.1 can be approximated as:

$$\begin{aligned} I &\propto V, \text{ when } eV_{\text{jct}} \ll k_B T, \\ I &\propto V^\alpha, \text{ where } \alpha = 2N_{\text{cot}} - 1, \text{ when } k_B T < eV_{\text{jct}} < k_B T \ln \left(\frac{e^2}{h} R_T \right), \\ I &\propto \exp \left(-\sqrt{\frac{V^*}{V}} \right), \text{ when } k_B T \ln \left(\frac{e^2}{h} R_T \right) < eV_{\text{jct}}, \end{aligned}$$

where N_{cot} is a number of junctions involved into cotunneling (typically, $N_{\text{cot}} \approx 4-5$) and V^* is a characteristic voltage: $V^* = \frac{E_C}{e} \ln^2 \left(\frac{e^2 E_C R_T}{h e V_{\text{jct}}} \right)$.

4.3 Emerging functionalities in arrays

Extra functionality can be added to NP array by using functional molecules with an exchange procedure. The basic feature studied on the level of single molecules and thereby considered as possible functionality for an array is the molecular switching. Plenty of molecular switches were proposed [12]. Here, optical and electrochemical switches are described.

4.3.1 Optical switching in NP array

Photochromic diarylethene is well known for its optically-induced reversible isomerization, which does not change the length of the molecule, which makes diarylethene attractive candidate to build molecular devices. Diarylethene-based molecules were electrically measured before using MCBJ [130] and STM [131] approaches. It was observed, that the molecule can be switched only in one way once it is connected to gold. The possible reason is a strong coupling between molecule and the gold, which can be overcome by the special design of molecular structure, which decouples the optically-sensitive core of the molecule from the thiol linker groups.

Reversible switching of diarylethene molecule in NP array was demonstrated by van der Molen *et al.* [132]. Target molecules were inserted into NPA device using standard molecular exchange procedure (Fig. 4.3a). The measurements were performed during several cycles of alternated ultraviolet ($300 < \lambda < 400$ nm)

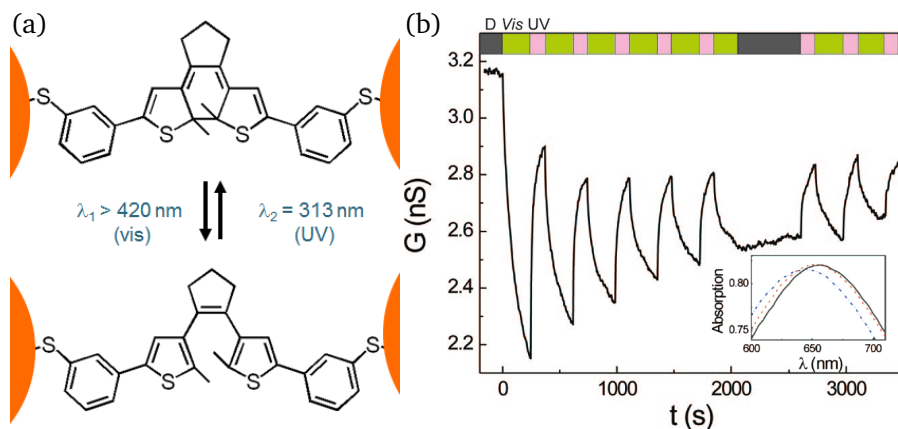


Figure 4.3: (a) Schematics of the optical switching of diarylethene molecule bridging neighboring nanoparticles in NP array. (b) Conductance of the NPA device measured along several cycles of alternated ultraviolet and visible light illumination. The inset shown the the optical spectra before illumination (black curve), after first UV illumination (blue) and after visible light illumination (red). Note that red and black curves almost coincide. Figure is taken from van der Molen *et al.* [132].

and optical ($590 < \lambda < 650 \text{ nm}$) light illumination. Conductance was measured simultaneously with optical absorption spectra (Fig. 4.3b). Decrease in conductance was observed while the array is illuminated by visible light, and increase for UV light. Since shifts in optical absorption spectra were also observed, the changes in conductance were attributed to the isomerization of the diarylethene molecules, i.e. reversible optical switching on the single molecular level.

4.3.2 Electrochemical switching

Since the NP array devices are stable in the liquid environment (and molecular exchange procedure is performed in solution), by insertion red-ox active molecules into the array, the sensor on oxidants or reductants can be created. Liao *et al.* [133] demonstrated electrochemical switching in the NP array using tetrathiafulvalene (TTF) derivative. Oxidation of TTF molecule with iron (III) chloride causes increase of conductance by the factor of ~ 30 , since the subsequent reduction with ferrocene restores the conductance to an initial value (Fig. 4.4).

4.3.3 Strain sensing

Since the current through the nanoparticle network has a tunneling nature, which is strongly dependent on the interparticle distance, nanoparticle array without any functionalization can be used as a very sensitive strain sensor. The sensitivity of the

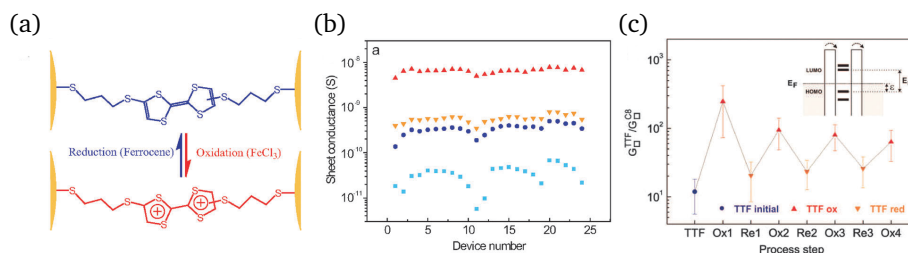


Figure 4.4: Electrochemical switching in the NP array. (a) Schematics of reversible switching of TTF molecule: oxidation by iron (III) chloride FeCl_3 and reduction by ferrocene. (b) Measured sheet conductances for the devices after fabrication (with octanethiol ligands; light blue squares), after TTF molecule insertion via molecular exchange (blue circles), after oxidation process (red triangles) and after subsequent reduction (orange triangles). Conductance after one cycle of oxidation and reduction returns to the initial value. (c) Reproducibility of the switching for several redox cycles. Figures are taken from Liao *et al.* [133].

strain sensors is described by gauge factor, which is defined as $GF \equiv \frac{\Delta R/R_G}{\varepsilon}$, where R_G is an initial resistance, ΔR is a change in resistance, and ε is a strain. For existing metallic strain devices GF is around 2. Using three-point bending mechanism, as in MCBJ setup, Guédon *et al.* [134] demonstrated high gauge factor of about 25, measured in the ordered nanoparticles monolayers, transferred on the phosphor bronze substrate (Fig. 4.5a). By insertion OPE molecules into the array, the gauge factor decreased by a factor of 5 (Fig. 4.5b), which can be explained by the change of molecules on the nanoparticles.

4.4 Dimension control in NP array

By pre-patterning the substrate, Liao *et al.* [135] demonstrated possibility to limit one of the dimensions of an array to only few decades of nanoparticles. The possibility to create arrays with arbitrary shapes was also demonstrated (Fig. 4.6a–c). Three-dimensional nanoparticle array can be created by sequential stamping of monolayers one over another (Fig. 4.6d) [136].

Thereby, using inherently two-dimensional self-assembled arrays of nanoparticles, pseudo-1D and 3D-structures can be created.

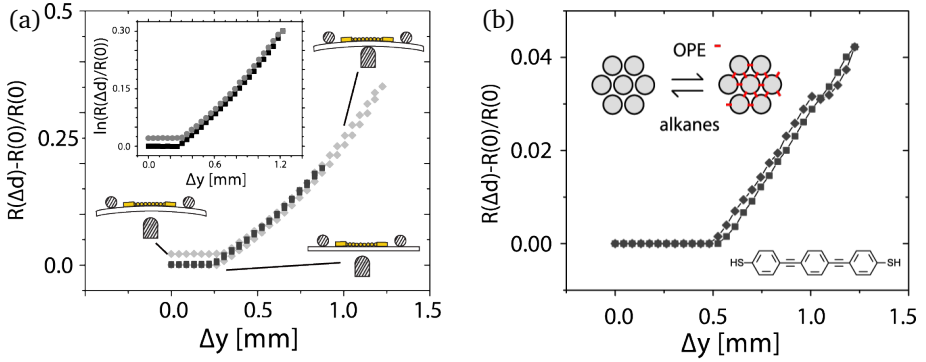


Figure 4.5: Relative resistance change of the NP array in the three-point bending mechanism with respect to the pushing rod displacement: (a) for alkanethiol-covered nanoparticles, and (b) after OPE-molecule insertion using molecular exchange procedure. Figures are taken from Guédon *et al.* [134].

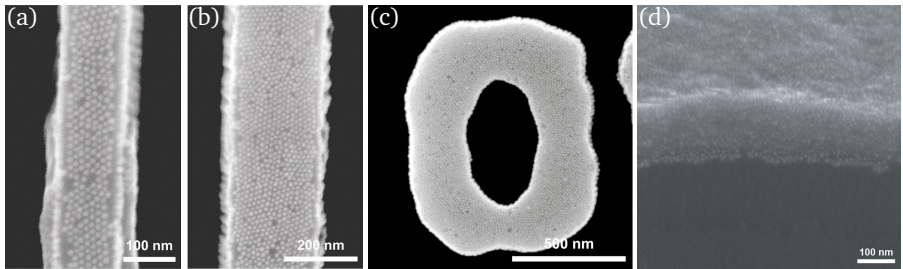


Figure 4.6: (a, b) NP array stripes with nanometer-sized width. (c) An example of NP array with arbitrary shape. Figures are taken from Liao *et al.* [135]. (d) SEM image (tilted view) of 15-layer thick NP array. Figure is taken from Wang *et al.* [136].

Graphene electrodes for hybrid devices



As shown in Chapter 4, nanoparticle array (NPA), or nanoparticle self-assembled network (NPSAN), is a convenient platform to investigate properties of individual molecules, or molecular junctions, on the larger scale. The geometry of devices is limited to the non-resist based lithography, since an organic molecular shell can be easily affected. Nanoparticle-based devices are usually fabricated using stamping of a NP array onto Si/SiO₂ or flexible substrate followed by evaporation of the metallic contacts using transmission electron microscopy (TEM) grid as a shadow mask (Fig. 5.1a). Such fabrication procedure requires proper alignment of the TEM grid on top of stamped NP array, which can destroy the regularity of an array. Thus, to be able to fabricate devices with arbitrary desired geometry, another approach is required. The key idea of the new fabrication strategy is to pattern electrodes first and then transfer nanoparticles on top of the electrodes and avoid any manipulations with an array after transfer.

Devices following this approach were fabricated and characterized before by Viero *et al.* [137]. In this work, thin metallic electrodes (1 nm Ti and 10 nm Au) were patterned using e-beam lithography, and NP array was transferred on top of the elec-

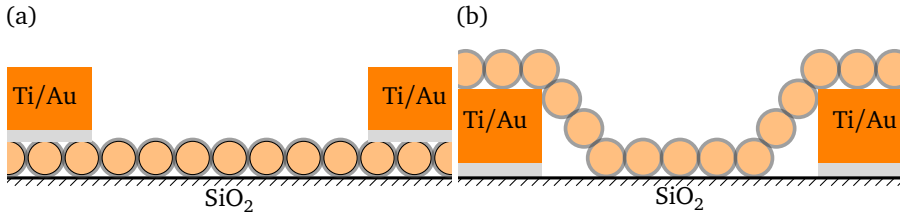


Figure 5.1: (a) Schematics of the regular NPSAN device. (b) Schematics of the NPSAN device with gold electrodes below an array. Size of nanoparticles and thickness of electrodes are to scale.

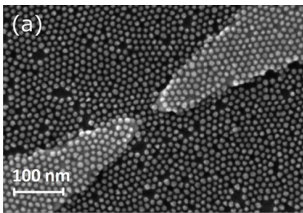


Figure 5.2: SEM image of the NPSAN device with gold electrodes underneath. Reprinted with permission from Viero *et al.* [137]. Copyright 2015 American Chemical Society.

trodes (Fig. 5.2a). The nanoparticles were functionalized with optically-sensitive azobenzene molecules, which reversibly isomerize under UV light illumination (see Subsection 5.3.2 for more details). Subsequent IV measurements confirmed good electrical contact between electrodes and NP array and the changes of the NP array resistance before and after illumination, which was attributed to the isomerization of the azobenzene molecules in the array.

The drawback of such geometry is an uncertain contact area between electrodes and nanoparticles (Fig. 5.1b). Since the diameter of nanoparticles is comparable to the size of electrodes, the shape of the edges is uncertain, thus, the array can not be described by its geometry (i.e. fabrication of the devices with the same geometry and electrical properties is not reproducible).

5.1 Graphene as an electrode for NP array

To circumvent the problem of the uncertain contact geometry, we proposed to use graphene as a contact material for NPA devices (Fig. 5.3). Graphene is a single atomic layer of sp^2 -hybridized carbon, which is well known for its unique electric properties [138]. Graphene has an ultimate thickness of 3 \AA , which makes it perfect candidate for contacting nanoparticles from the bottom. Possibilities to contact individual nanoparticles [139] and nanoparticle network [140] with graphene electrodes were demonstrated before. Several techniques to obtain graphene are already well developed. In this work large-area graphene grown by CVD method

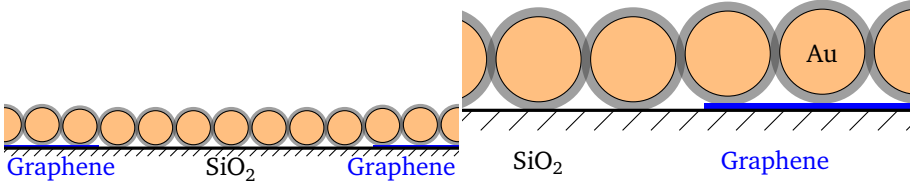


Figure 5.3: Schematics of NPA device with graphene electrodes. Dimensions of nanoparticles and graphene are to scale.

was used (see Section B.2 for details). Hybrid NPA device with graphene electrodes we called graphene/nanoparticles array device, or G/NPA.

To test the possibility to use graphene as an electrode to the NP array, two-terminal devices were fabricated. (Fig. 5.4a). Graphene stripes with a width of $60\mu\text{m}$ and a length of $\sim 100\mu\text{m}$ were patterned using e-beam lithography. The gap size between neighboring graphene electrodes was in the range $5\text{--}10\mu\text{m}$. Then, metal contact pads with the size of $100 \times 100\mu\text{m}$ (5nm Ti and 60 nm Au) were evaporated. Finally, NP array (gold nanoparticles, 10 nm in diameter, covered with 1-octanethiol) was transferred on top of graphene electrodes. Resulting active area of the device is $60 \times (5 - 10)\mu\text{m}$. Every sample has a few dozens of individual two-terminal devices.

For every two-terminal device current-voltage characteristics were measured. As can be seen from the measurements (Fig. 5.4b), IV characteristics of the devices are linear. Calculated sheet conductance value (G_{\square}) of the devices lies in the range ($10^{-5.6} G_0$, $10^{-4.8} G_0$) (Fig. 5.4c–d), which is in a good agreement with previous measurements performed in conventional NPSAN devices [121]. Thereby, the graphene can be used as electrode to contact NPA, which is easy to pattern into desired geometry.

5.2 Downscaling the NPA-based hybrid devices

Bose *et al.* [45] demonstrated possibility to create ‘programmable’ device based on unordered blob of nanoparticles. It was shown that using genetic algorithm applied to designless nanoparticle network via several terminals, any binary boolean function can be implemented. An important requirement for such system is a Coulomb blockade transport, or, more generally, very strong non-linear response. To access electrical properties of individual molecules in the NPA device, such as possible non-linear response, further miniaturization of the active area of G/NPA device is required. Non-linearities in individual molecular junctions were observed with the applied bias $\sim 600\text{mV}$ [19]. Assuming that applied voltage across the NPA-based device is 10 volts, to achieve nonlinear effect the length of the device

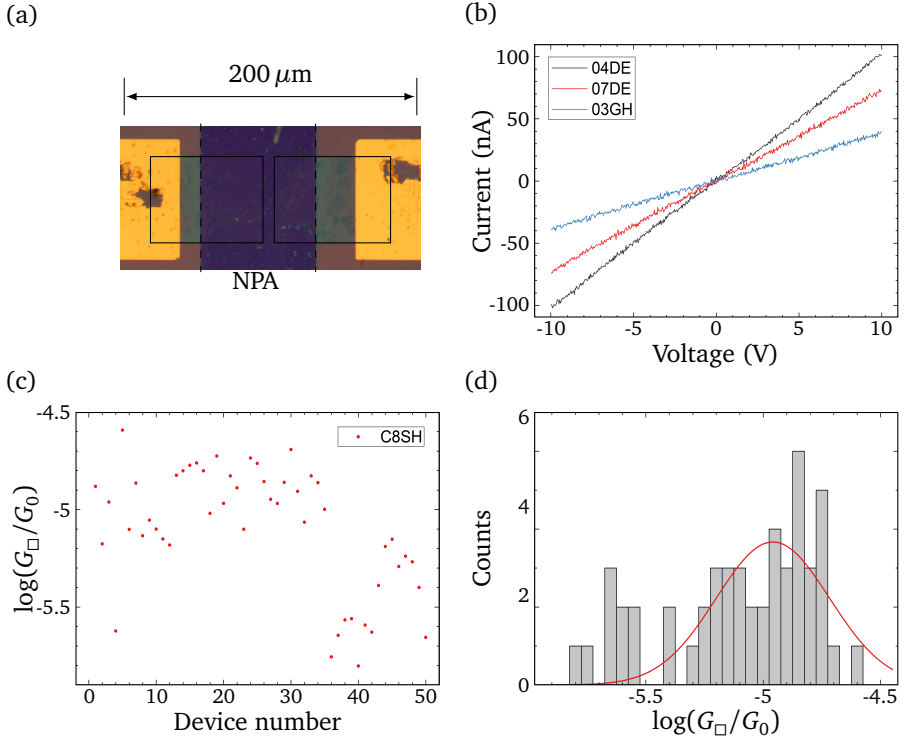


Figure 5.4: (a) Optical image of two-terminal G/NPA device. Solid lines represent shape of graphene electrodes, and dashed lines show stamped NP array (false color). (b) Typical IV characteristics of different two-terminal devices. (c) Sheet conductances of the measured devices. (d) Distribution of sheet conductances and Gaussian fit of the distribution ($\mu = -4.95$, $\text{FWHM} = 0.57$).

should not be exceed ~ 20 nanoparticles, or 200–250 nanometers. Thereby, the required distance between electrodes in NPA device is no more than 200 nm. For better electrical control of the NPA, multi-terminal geometry is also required.

5.2.1 Optimization of PMMA-based e-beam lithography

The design of 8-terminal GNPA device was developed (Fig. 5.5). For the fabrication of the electrodes patterned PMMA was used as a etching mask for RIE (see B.3 for details). The devices were fabricated on the Si/SiO₂ (300 nm) substrates.

Using different geometries of the e-beam mask (Fig. 5.6, top), a variety of shapes of graphene electrodes were obtained with a gap size down to 500 μm (Fig. 5.6, bottom).

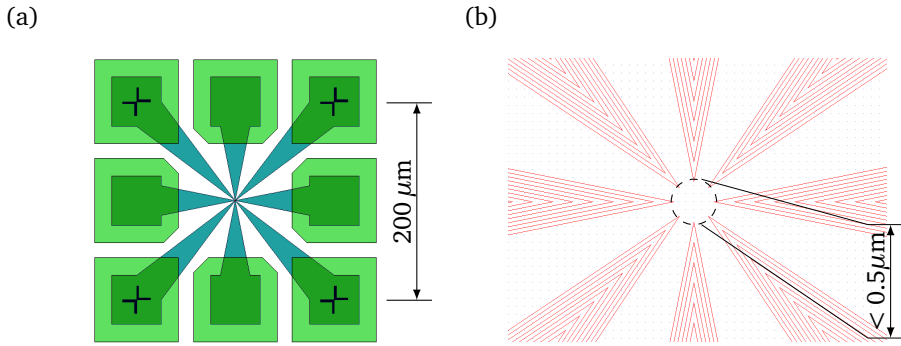


Figure 5.5: (a) Schematics of 8-terminal G/NPA device. Light green: contact pads, dark green: patterned graphene electrodes. (b) Central area of an e-beam mask for PMMA patterning.

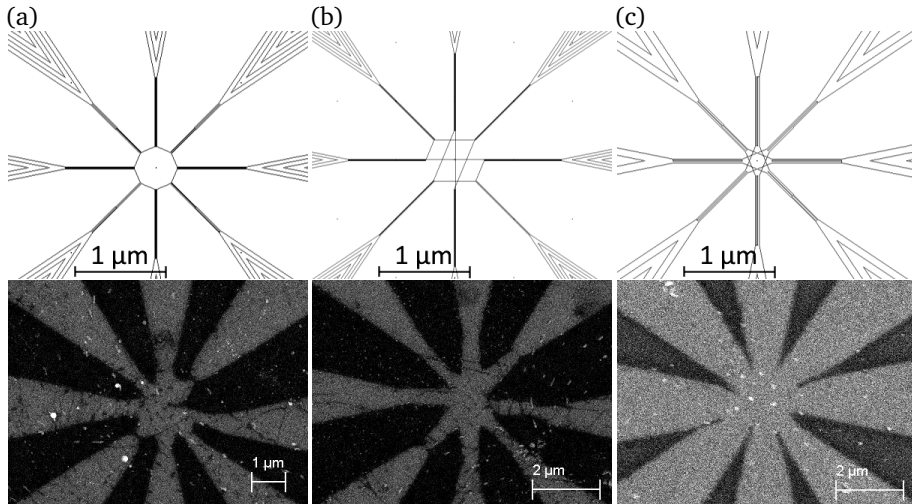


Figure 5.6: The e-beam structures (top) used for the patterning of the PMMA etching mask and resulting graphene electrodes (bottom, dark areas). The structures are exposed with the line dose of 900 pC/cm with an accelerated voltage of 10 kV.

5.2.2 Further miniaturization of G/NPAs: HSQ approach

An important limiting factor of the existing fabrication procedure is the usage of patterned PMMA as etching mask. Another approach is to use negative-tone resist to pattern graphene electrodes, not inter-electrode areas. This resist should be preferably stable to oxygen plasma in the RIE, which allows to etch the graphene for a long time and remove all the possible residues.

We choose HSQ (hydrogen silsesquioxane) resist for such approach. HSQ is well known negative-tone resist, which is transforming into silicon dioxide being exposed to electron beam. The resolution of the structures, written with HSQ, can reach up to 10 nm [141]. To achieve such resolution, the resist has to be very thin (few tens of nanometer), exposed to 100 kV e-beam as fresh as possible. All the fabrication was done using the facilities of IEMN CNRS in Lille, France. E-beam lithography was performed using Vistec e-beam machine.

HSQ on graphene

The substrates with graphene were prepared in Basel. The fabrication steps of the first generation samples were the following:

- Preparation the substrates: cleaning in acetone, IPA, followed by N₂ drying and 10 minutes baking at 180 °C for total dehydration.
- Spin-coating of HSQ resist (XR1541 6%, diluted in MIBK 1:3 v/v): resist is transferred on the substrate using the syringe with 0.2 μm filter, followed by spin coating at 3200 rpm for 60 seconds and 1 min baking at 80 °C. Final thickness of the resist is 20 nm.
- E-beam writing of the structures at 100 kV acceleration voltage with the dose of 7000 μC/cm².
- Development for 1 minute in 25% Tetramethylammonium hydroxide (TMAH), followed by double-rinsing in de-ionized water for 2 minutes and N₂ drying.
- RIE of graphene: 8 sccm of O₂/16 sccm of Ar at 30 W and 250 mTorr for 1 minute.

Figure 5.7a shows exposed HSQ after development. The gap size between electrodes is about 80 nm. To remove exposed HSQ, three different etchants were used: 1 minute in 1% solution of HF, 10 seconds in buffer oxide etchant (BOE 7.1, mixture of 40% water solution of NH₄F and 49% solution of HF 6:1 v/v), diluted in de-ionized water 1:2 v/v and 1:29 v/v. In all three cases, we observed flushing the graphene from the sample because of etching the SiO₂ substrate below the electrodes (Fig. 5.7b).

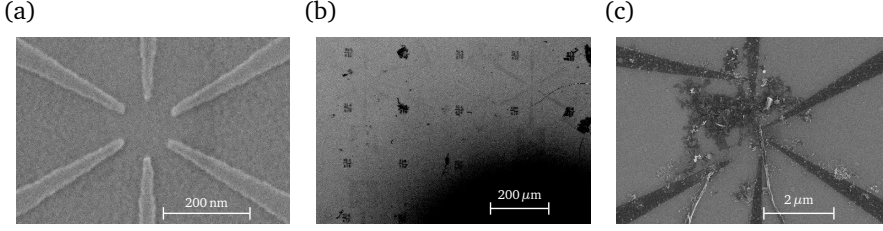


Figure 5.7: SEM images of HSQ mask for graphene etching. (a) Before BOE etching. (b) After BOE etching: HSQ mask and graphene are removed. (c) HSQ residues on the substrate after double-stack lithography.

Double-stack lithography

For easiest removal of exposed HSQ from the substrate without usage aggressive HF-based etchants, two-layered resist consisting of thin layers of PMMA and HSQ was used. This approach allows to combine the advantages of HSQ for high resolution lithography with the possibility to remove exposed HSQ by dissolving supporting PMMA layer in warm acetone. The same fabrication procedure as before was used, but first thin (180 nm, PMMA 950k) layer of PMMA was spin-coated on the substrate, followed by 20 nm thick layer of HSQ.

After all the subsequent steps of fabrication, we observed that exposed HSQ cannot be removed by acetone, instead it sticks to SiO_2 substrate in the random places (Fig. 5.7c).

Graphene electrodes on silicon nitride substrate

To avoid problems with the lift-off, described above, we used silicon nitride ($\text{Si}/\text{Si}_3\text{N}_4$) substrates instead of Si/SiO_2 . Silicon nitride is significantly more stable against HF-based etchant solutions.

Repeating the same steps of lithography, graphene electrodes with a gap of by 80–160 nm in between were obtained (Fig. 5.8).

5.2.3 Local transfer of nanoparticle arrays

To reduce leakage current between electrodes, we developed and implemented a method of the local NPA transfer. The goal is to transfer NP array only in the area of the electrodes, and the size of an array should be comparable to the size of the gap between the electrodes, as shown in Figure 5.9a. The overall design of multi-terminal G/NPA device with locally transferred NP array is depicted in Figure 5.9b.

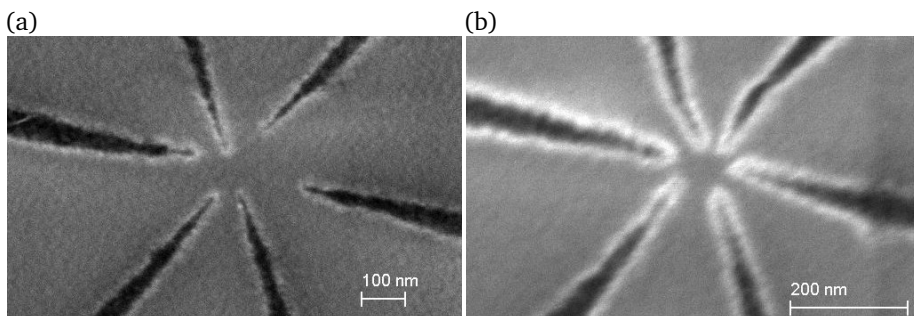


Figure 5.8: SEM images of nanogaps between graphene electrodes fabricated on Si_3N_4 substrate. (a) 160 nm gaps. (b) 80 nm gaps.

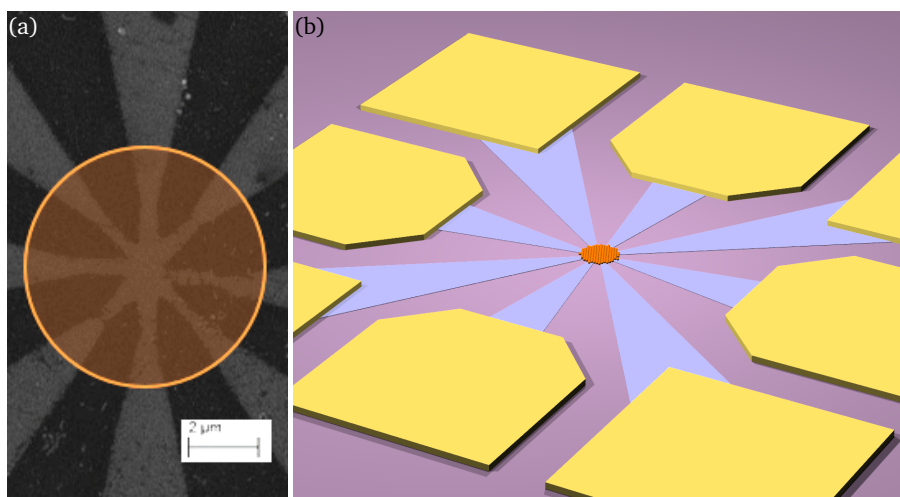


Figure 5.9: (a) Concept of multi-terminal NPA device with graphene electrodes and small-sized NPA as an active object. Orange semitransparent circle marks the area where NP array should be transferred. (b) Schematics of G/NPA device with transferred small NP array.

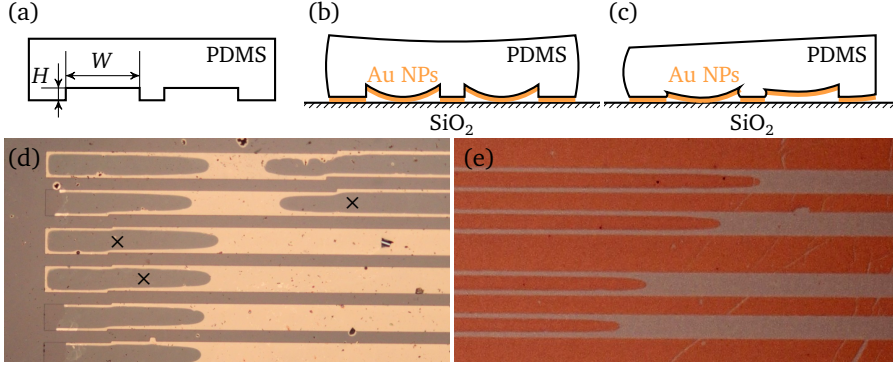


Figure 5.10: (a) Schematics of PDMS stamp with characteristic dimensions. (b, c) Schematics of the PDMS stamp deformations due to extra pressure and non proper level alignment of the stamp, respectively, which cause unwanted transfer of nanoparticles in wrong places. (d) Optical image of the stamp during the stamping procedure. Dark: regions where the stamp is in a contact with a substrate. Due to high pressure, stamp is bending and nanoparticles are transferred onto unwanted places (marked with \times). (e) Optical image of the NPs after transfer.

PDMS stamps design, fabrication and optimization

New design of PDMS stamps is necessary for the fabrication of proposed G/NPA devices. Local transfer of nanoparticles on top of patterned graphene electrodes has the following requirements:

- alignment of PDMS stamp and the substrate in XY-plane;
- alignment of contact surface of the stamp with the substrate;
- control the pressure during stamping to avoid deformation of the stamp and unwanted transfer.

If the applied pressure is too high, due to deformation of the stamp transfer of nanoparticles outside of desired areas is possible (Fig. 5.10b). The same happens if the contact surface of stamp is not parallel to the substrate (Fig. 5.10c), and irregular transfer of nanoparticles happens due to different applied pressure in different places. Examples of not desirable transfers are shown on Figure 5.10d-e.

To avoid extra bending, the width to height ratio ($W : H$, see Fig. 5.10a) of the stamp should not exceed 20:1. Thus, to stamp small structures, i.e. with big W , one have to prepare the stamp with $H \geq W/20$.

Therefore, the masters for PDMS stamp were fabricated in thick (ca. $3\ \mu\text{m}$) PMMA layer (see B.4 for details). In addition, the design of the stamp includes the

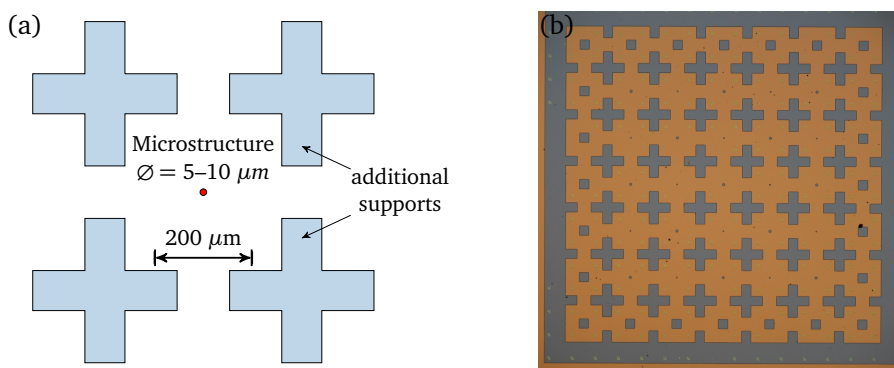


Figure 5.11: (a) Schematics of the mask for the e-beam lithography. (b) Optical image of the master for the stamps, prepared in 3 μm thick PMMA. Dark area: Si substrate, light area: PMMA. Total size of the master is 3×3 mm.

‘supports’ structures which prevent extra bending of the stamp in both directions (Fig. 5.11a).

To check the limitations for small-sized NP array transfer, the stamps with different sizes of pillars we fabricated. Several NP array transfers were performed using such stamps (Fig. 5.12a).

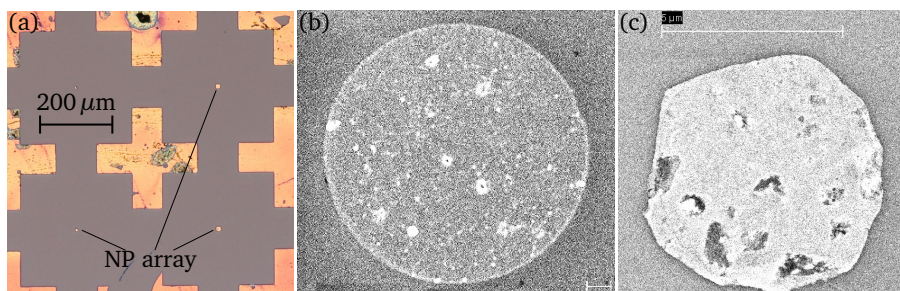


Figure 5.12: Local NP array transfer via stamping. (a) Optical image of transferred NP array on Si/SiO₂ substrate. (b) SEM image of stamped NP array with a diameter of 10 μm . Scalebar 1 μm . Transferred array has predefined shape, indicating good quality of the transfer. (c) SEM image of stamped NP array with a diameter of 5 μm . Scalebar 5 μm . Shape of the array is distorted by the edge effects.

The structures with the size of 10–20 micrometers in diameters were transferred well (Fig. 5.12b), but smaller structures (with the diameter of 5 μm) were strongly affected by edge effects (Fig. 5.12c). For smaller structures, viscous PDMS is not always fully filling the pit in the PMMA master, so the quality of the stamps decreases.

Local transfer on patterned graphene electrodes

To fulfill all the requirements for the proper NP array transfer (see p.65), the aligned stamping was performed under the optical microscope (Fig. 5.13). The substrate with a pre-defined gold contact pads and graphene electrodes was fixed on the vacuum holder of the microscope. The holder has 3 degrees of freedom (X, Y and rotation around Z-axis). The stamp is fixed on the bottom side of the glass slide, which is fixed in the manipulator with XYZ-degrees of freedom. The parallelism of the substrate and the stamp is controlled by the levels.

Transparency of the glass slide and PDMS stamp (even when the stamp is inked with nanoparticles) allows to perform alignment with a visual control in the microscope. When the PDMS stamp is in a close proximity to the substrate (less than 300–500 μm), the surfaces of the substrate and the stamp are in the focus range of the microscope (Fig. 5.13b), and precise alignment with the precision of $\approx 1 \mu\text{m}$ is possible. After alignment, the stamp is moved to the soft contact with a surface for 10 seconds, and then slowly lifted up. Small-sized NP array is transferred on the graphene electrodes (Fig. 5.13c, d).

Quality of the local NPA transfer

SEM images of the NP array after transfer show that the quality of the array on the graphene and on the SiO_2 substrate is different: while the array on the graphene has proper packing of the nanoparticles (Fig. 5.14a), array outside of graphene electrodes, i.e. on the SiO_2 substrate has more holes (Fig. 5.14b). This can be attributed to the hydrophobicity of graphene as well as thiol-based shell of nanoparticles.

5.3 Functionality of G/NPA devices

Nanoparticle network is a convenient platform to test properties of individual molecules on the large scale. To implement molecular features on the level of network, functional molecules have to interlink the nanoparticles either by synthesis [137], or by molecular exchange procedure [121]. Both possibilities were tested in the hybrid graphene/NPA devices.

5.3.1 Molecular exchange

8-terminal devices were tested for the molecular exchange functionality. First, small arrays of nanoparticles (10 nm in diameter with 1-octanethiol organic shell) with the size of 20 μm were locally transferred on top of graphene electrodes. The gap size between graphene electrodes was about 1 μm . IV characteristics were measured between all the pairs of electrodes.

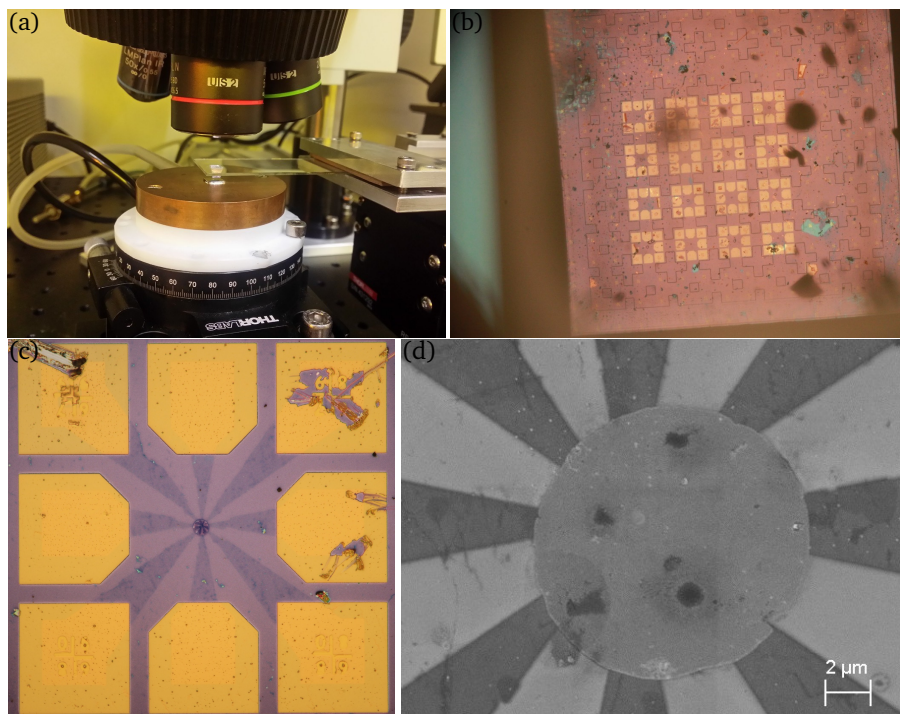


Figure 5.13: Procedure of local stamping of NPA on the graphene electrodes. (a) Sample and glass slide with the stamp under the optical microscope. (b) Optical image of the sample and the stamp during alignment. Note that shapes of the structures on the stamp are visible as well as contact pads on the sample, allowing precise alignment. (c) Optical image of one 8-terminal device with transferred small-sized NPA. (d) SEM image of the NP array with the diameter of 10 μm transferred on top of graphene electrodes.

After that, the sample was placed into 10 μM solution of oligo(phenylene ethynylene) molecule (OPE3-2N, Fig. 5.15b, in red) in mesitylene for molecular exchange. The process was performed for 24 hours under the argon atmosphere and with constant bubbling of argon through the solution to prevent oxidation of the thiol end groups. After exchange, the sample was washed in mesitylene and dried in the N_2 flow. IV characteristics were measured for the same pairs of electrodes.

Measured resistances are shown in Figure 5.15a. Clear decrease of resistance is observed, as a signature of molecular exchange. On average, the resistance of the individual devices decreased by a factor of ≈ 20 (Fig. 5.15b). This decrease in resistance is significantly smaller than observed in NPSAN devices with gold electrodes for OPE3 molecules [121, 125].

Thereby, hybrid devices with graphene electrodes are stable in the liquid en-

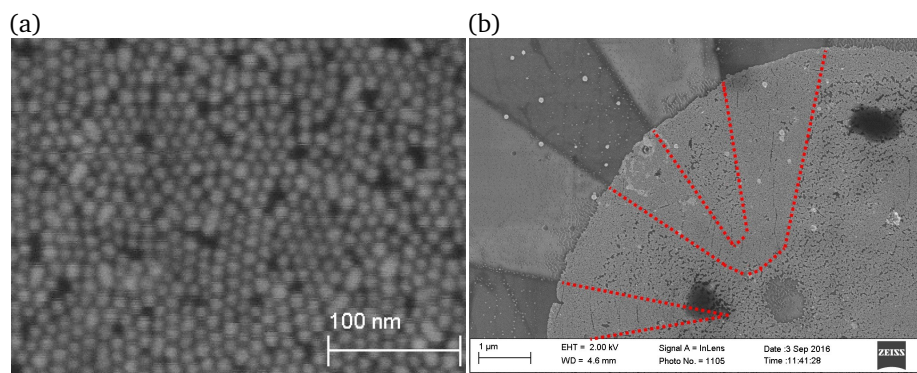


Figure 5.14: (a) SEM image of transferred NP array on top of graphene electrodes. (b) SEM image shows differences in the NP array quality in the areas of graphene electrodes and outside of these areas. Red dashed lines represent graphene electrodes under stamped NP array.

vironment under the conditions of the exchange procedure. The measurements demonstrate possibility to perform molecular exchange, however, the efficiency of an exchange is smaller than for conventional NPSAN devices with gold electrodes.

5.3.2 Optical molecular switching in G/NPA

Within collaboration with Institute of Electronics, Microelectronics and Nanotechnology in Lille, France (IEMN CRNS), we tested optical switching in the hybrid devices with graphene electrodes and nanoparticle arrays, formed by 10 nm azobenzene-covered gold nanoparticle. Azobenzene (AzBT) molecule is known to be reversibly switched from *cis*- into *trans*-configuration using UV or visible light illumination (Fig. 5.16). Switching between configurations changes the overlap between molecular chains which causes changes in conductance. Efficient reversible switching was previously demonstrated in the nanoparticle arrays with gold electrodes [137].

Multi-terminal devices with 8 graphene electrodes with 0.5–1 μm gap in between were fabricated (Fig. 5.17a, b). Then, nanoparticle array was transferred from the water-air interface following the procedure described in [137] (Fig. 5.17c). The nanoparticles were 10 nm in diameter and covered with light-sensitive azobenzene molecules during synthesis. Azobenzenes are oxygen-sensitive, so all the further measurements were performed in the glovebox under Ar atmosphere.

First, voltage-current characteristics were measured between all pairs of electrodes. The measurements were performed using an Agilent 4156C semiconductor parameter analyzer in the unipolar regime. Typical IV of such two-terminal device is strongly nonlinear (Fig. 5.18a, black curve). To characterize the devices quantitatively, for every IVs we defined the linear regime (as a voltage range, where

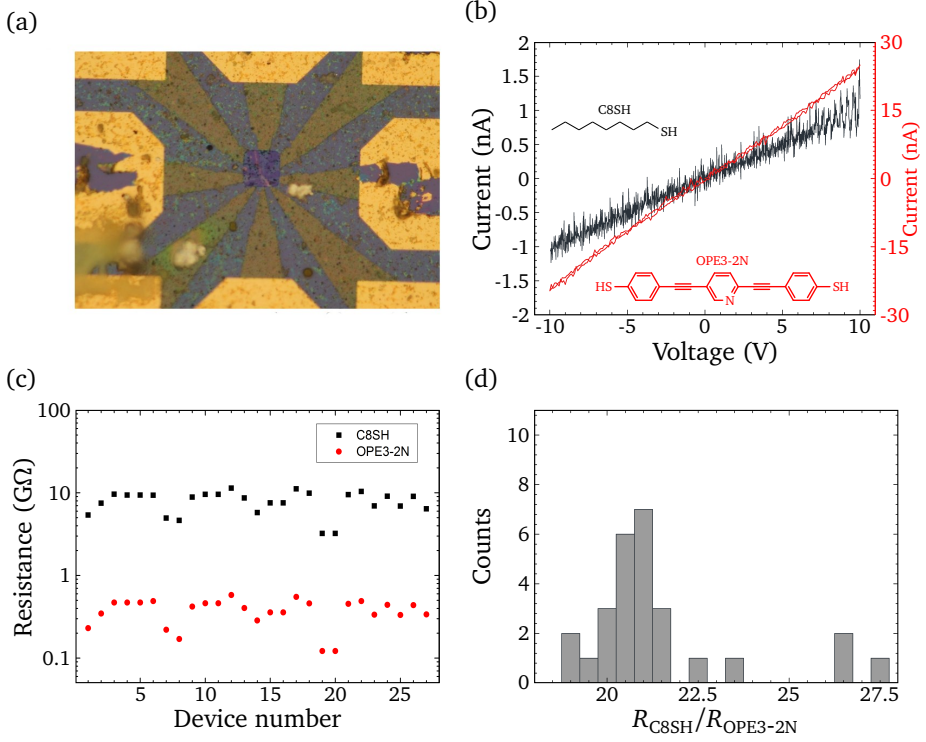


Figure 5.15: (a) Optical image of G/NPA sample after molecular exchange. Dark square in the center is a NP array. (b) Typical current-voltage characteristics measured between certain pair of electrodes before (black curve) and after (red curve) molecular exchange with OPE3-2N molecule. Note different vertical scales. (c) Resistances of all measured devices. (d) The distribution of resistance change after exchange.

coefficient of determination r^2 for the linear fit is above 0.99), and extracted the linear resistance. The resistance of our devices was in the range from 500 GΩ to 2 TΩ.

Then, devices were exposed to UV light using high power LED (M365F1 from Thorlabs) with the wavelength of 365 nm. The power density of light was $\sim 6 \text{ mW/cm}^2$, and illumination time of 2 hours. After illumination, the measurements were repeated for the same pairs of electrodes (Fig. 5.18a, red curve).

For every measured IV after illumination, we extracted linear resistance in the same way as before. Figure 5.18b show overall statistics for all measured two-terminal devices before and after illumination. For every device we defined on/off ratio as a ratio between linear resistance after and before UV illumination. The distribution of on/off ratios (Fig. 5.18c) shows the effective increase in conductance

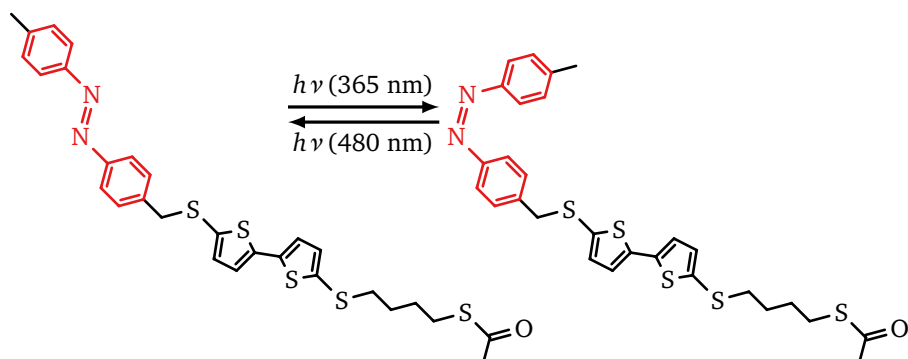


Figure 5.16: Optical switching of AzBT molecule. The configuration of the molecule is changing from trans- (left) into cis- (right) with UV light illumination, and can be reversible switched back with visible blue light illumination. Azobenzene substructure is shown in red.

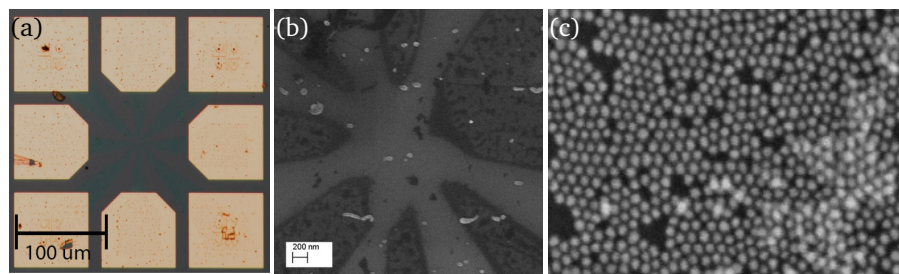


Figure 5.17: (a) Optical image of the G/NPA device with patterned graphene electrodes and gold contact pads. (b) SEM image of the nanogap between graphene electrodes. Dark areas: graphene electrodes. The gap size between electrodes is about 1 μm . (c) SEM image of transferred NP array with AzBT molecular shell.

by the factor of $G_{\text{on}}/G_{\text{off}} \approx 40$.

Thereby, cis-trans isomerization of AzBT by UV light illumination is changing the resistance of the device by a factor of ~ 40 , which is slightly higher than measured before by Viero *et al.* [137] in the configuration with bottom gold electrodes. The increase in conductance was observed in 43 two-terminal devices out of measured 44, therefore the yield of optical switching was 98%.

To perform reverse switching into ‘off’ state we exposed our devices to blue light (480 nm, 0.1 mW/cm²) for 2 hours. However, we observed only a slight decrease of conductance ($\approx 10\%$), and only in few devices. This can be explained by some reconfiguration of the molecules on the nanoparticle surface and even reorganization of nanoparticles in the array upon UV illumination mentioned in [137].

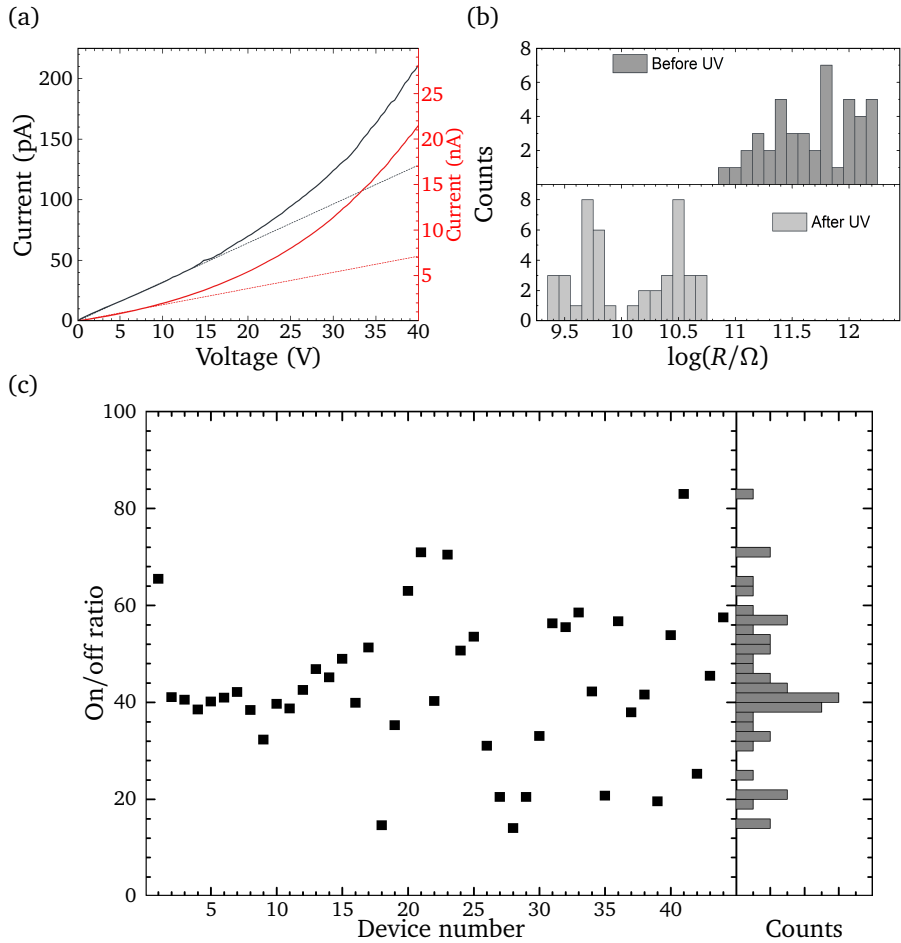
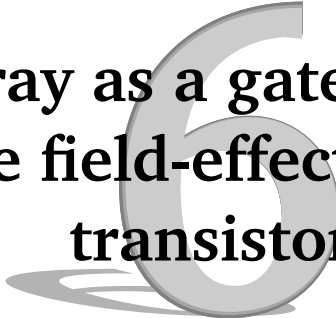


Figure 5.18: (a) Typical current-voltage characteristics of G/NPA devices with AzBT-covered nanoparticles and graphene electrodes before illumination (black curve) and after 2 hours of exposure to UV light. Note high applied voltages up to 40 V and different y-scales. Red and black dashed lines represent linear fits to the curves in the linear regime for each IV. (b) Distributions of device resistances. (c) Overview of on/off ratios for all measured devices.

5.4 Conclusion and outlook

Our investigations showed good potential of CVD grown graphene as a contact material for nanoparticle arrays. The adhesion of the nanoparticles to graphene is high due to hydrophobicity of organic shell, thereby NP array on top of graphene is stable under the condition of molecular exchange. Any functional molecules exhibiting e.g. optical or electrochemical switching behavior can be inserted into the array. Optical switching in the array with azobenzene-covered nanoparticles was demonstrated. To gain more functionality from the molecular networks, e.g. nonlinear response at lower applied voltages, further decrease of the gap size between the electrodes is required.

Nanoparticle array as a gate for graphene field-effect transistor



Graphene is known to be a zero band gap semimetal with ambipolar electric field effect [138]. Ideal defect-free graphene at the 0 applied potential has completely filled valence band and completely empty conductance band, thereby, its resistance is high. By applying the potential to the back gate (usually, Si/SiO₂ substrate), electrons or holes are induced into graphene, resulting the decrease in resistance (Fig. 6.1). The sharpness of the zero gate peak is defined by the mobility of the charge carriers in graphene and their scattering. Due to impurities or residues on the graphene after device fabrication, graphene has some induced charge carriers (*doping*), and some extra back gate voltage is required to deplete charge carrier density and observe maximum resistance. This point on the resistance vs. gate dependence is known as charge neutrality point (CNP), or Dirac point.

Graphene has a lot of another interesting features such as high electric and thermal conductivity. Quantum Hall effect (QHE) is observed in graphene up to room temperature. In the previous chapter the properties of graphene as an electrode for the nanoparticle array were demonstrated. In this chapter, the properties of graphene field effect transistor (graphene FET, or GFET) are studied. Since

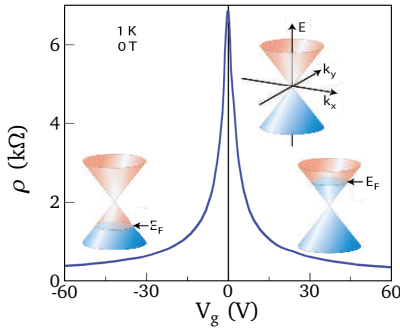


Figure 6.1: Electric field effect in graphene. V_g refers to the back gate voltage, applied to the Si/SiO₂ substrate, ρ denotes the resistivity of the device. Adapted by permission from Macmillan Publishers Ltd: Nature Materials, Geim and Novoselov [138], copyright 2007.

graphene does not have a band gap, it can not function efficiently as a transistor with high on/off ratio. However, band gap can be introduced into the graphene by, for example confining its dimensions. since the mobility of the carriers in graphene is very high, the graphene electronic device can be very fast.

6.1 Graphene FET with nanoparticle array

The proposed design of graphene FET with NPA is shown in Figure 6.2. The device consists of 8 terminals A–H, two of which (C, D) are connected to e-beam patterned graphene ribbon. Another 6 terminals are connected to 6 graphene electrodes, separated from the graphene ribbon by the gap with a size of 0.5–2 μm . Nanoparticle array is transferred on top of graphene by local stamping (see. 5.2.3). The diameter of transferred NP array is 5–10 μm . The active area of the graphene ribbon between the nanoparticles is about $1.5 \times 4 \mu\text{m}$ in size.

To investigate the properties of GFET, current-voltage characteristics were measured before and after nanoparticles transfer with respect to the applied back gate potential. Typical IV of the graphene FET is linear (Fig. 6.3a, inset). The back gate voltage was swept in the range (–40 V, 40 V). Measured gate dependence (Fig. 6.3a, black curve) shows the effective change of graphene resistance as expected. Charge neutrality point is about +35 V, i.e. graphene ribbon is highly p-doped.

Then, small-sized NP array (10 μm in diameter, formed by 10 nm gold nanoparticles with 1-octanethiol shell) was transferred on top of the FET. After NPA transfer, gate dependence was also measured (Fig. 6.3a, red curve). Presence of nanoparticles on the graphene shifts a charge neutrality point by 5–7 V, but the gate efficiency is decreasing. This effect can be attributed to increase of charge carrier scattering in graphene.

Since small hysteresis in the gate dependence is observed, effect of frequency was studied. Gate dependence was measured with different back gate voltage sweeping rates (Fig. 6.3b). The measurements show the change of hysteresis

6. NP array as a gate for graphene FET

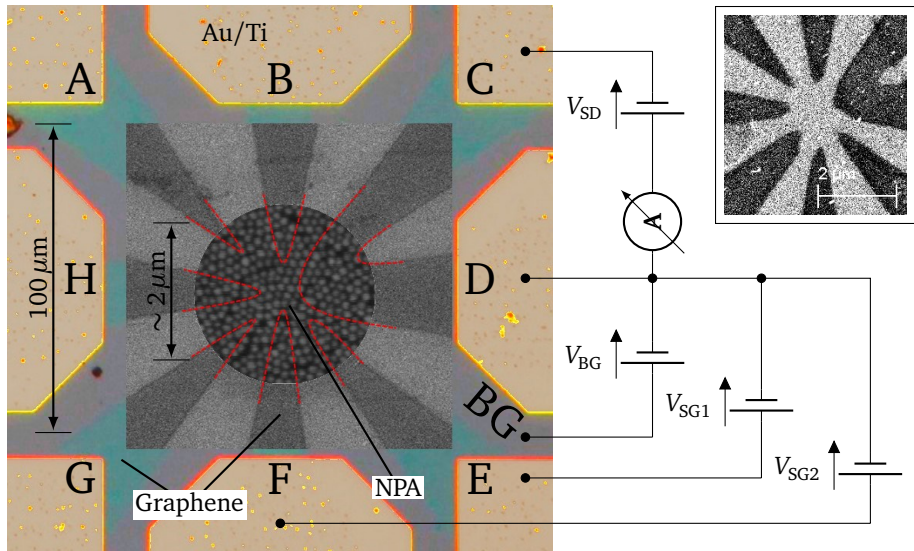


Figure 6.2: Schematics of graphene FET with NP array. Red dashed lines show the shape of graphene electrodes below the NP array. Capital letters A-H indicate names of the terminals, BG refers to the back gate, i.e. substrate. Inset shows the geometry of the electrodes and the gap.

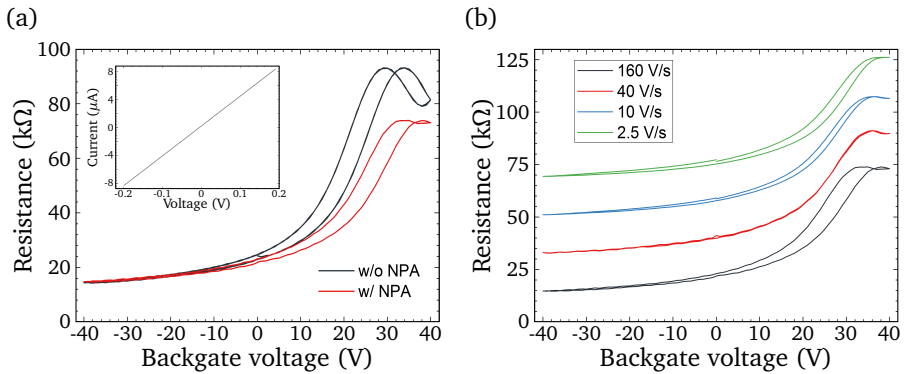


Figure 6.3: (a) Back-gate dependence of GFET without and with NPA. The inset shows typical IV of GFET. (b) Gate dependence of GFET with NPA for different sweeping frequencies. Curves are shifted vertically for clarity.

with change of sweeping rate, which can be attributed to capacitive coupling of nanoparticles to graphene.

6.2 Nanoparticle array as a top gate for the graphene FET

Since graphene has a good contact with nanoparticles, the possibility to apply potential to NP array via graphene electrodes is studied. Every multi-terminal device has 6 electrodes which can be considered as side (or, equivalently, top-) gates (terminals A–B and E–H on the Fig. 6.2). First, the resistance of graphene FET was measured with respect to voltages, applied to two side gates (Fig. 6.4a). Measured IVs have different slope, i.e. the graphene bridge has difference resistance. Assuming purely ohmic effect of applied top gate voltages on NPA, only offset in the IVs can be expected without changes in resistance. Therefore, the top gating effect is observed.

Figure 6.4b shows two-dimensional map of graphene resistance with respect to top gate voltages. Effect of single gate is shown in Figure 6.4c. Surprisingly, the gating effect is higher for the gate A than gate E, in spite of higher resistance of an array between gate A and graphene (Fig. 6.4d).

To characterize quantitatively an efficiency of top gating, the comparison of top gating with back gating was performed (Fig. 6.5). Surprisingly, while some voltage is applied to the back gate, the effect of top gate voltage is suppressed and can be neglected. The back gating curve was fitted according to [142] (Fig. 6.5b):

$$R(V_{BG}) = 2R_C + \frac{L/W}{e\mu\sqrt{n_0^2 + n_{ind}^2}} \equiv y_0 + \frac{A}{\sqrt{1 + \left(\frac{V_{BG} - V_C}{w}\right)^2}}, \quad (6.1)$$

where L , W are dimensions of graphene, n_0 and $n_{ind} = C_{ox}(V_{BG} - V_C)/e$ are intrinsic and induced charge carrier densities, respectively, $C_{ox} = \epsilon\epsilon_0/d$ is the sheet capacitance of SiO_2 layer with the thickness d , μ is the charge carrier mobility, V_C is the charge neutrality point, $w \equiv en_0d/\epsilon\epsilon_0$ is the shape parameter, defining the width of the gating peak, and y_0 is the offset parameter, related to the contact resistance R_C . The deduced parameters of the fit are the following: $y_0 = 9.6 \pm 0.3 \text{ k}\Omega$, $A = 27 \pm 0.5 \text{ k}\Omega$, $V_C = 19.6 \pm 0.5 \text{ V}$, $w = 17.1 \pm 0.3 \text{ V}$.

The effect of top gating can be defined as an effective voltage applied to the graphene, which causes the same effect when applied to the back gate. Mathematically, all measured resistances can be recalculated into effective back gate voltage using formula, reciprocal to Eq. 6.1:

$$V_{eff}(R) = V_C - w \cdot \sqrt{\left(\frac{A}{R - y_0}\right)^2 - 1}. \quad (6.2)$$

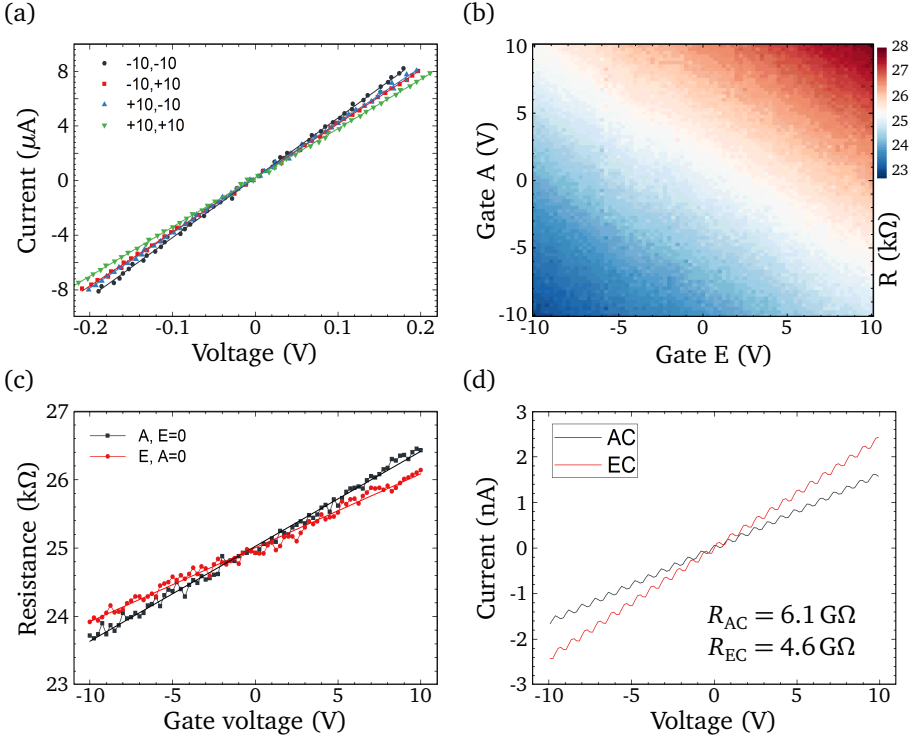


Figure 6.4: Double-gating measurements. (a) IV characteristics of graphene for different voltages, applied to the top gates E and A. (b) Two-dimensional map of resistance vs. gates E and A. (c) Single gate efficiency, while voltage applied to the second gate is 0 V. (d) Resistance of the NPA measured between graphene FET and the gates E and A.

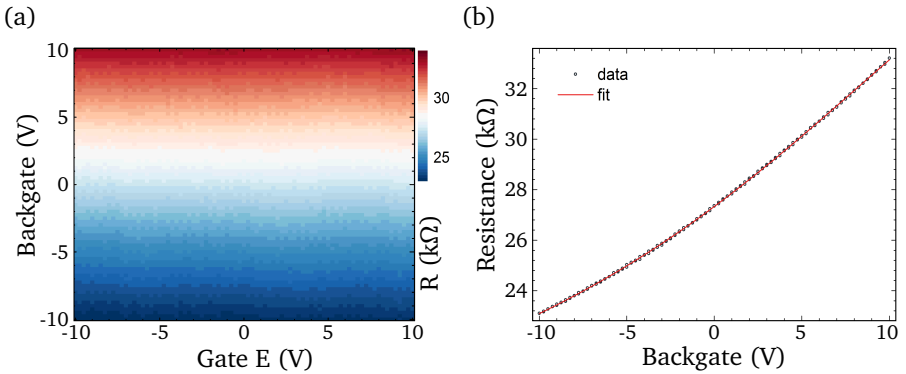


Figure 6.5: (a) Efficiency of top gating with back gate. (b) Back gating efficiency. Red curve denotes the fit of the data (black points).

Table 6.1: Extracted gating efficiencies for measured pairs of gates on the same multi-terminal device. BG refers to back gate, A, E, F, G, H refer to top gates (see Fig. 6.2).

Gate 1	α_{G1}	Gate 2	α_{G2}
E	0.016	BG	1
BG	1	A	0.015
E	0.21	A	0.27
F	0.09	A	0.27
F	0.07	H	0.24
G	0.16	H	0.21

The analysis was performed for all measured pairs of electrodes (Fig. 6.6).

Assuming linear relationship between applied voltages V_{G1} , V_{G2} and effective voltage V_{eff} :

$$V_{\text{eff}} = \alpha_{G1} V_{G1} + \alpha_{G2} V_{G2},$$

the efficiencies α for different pairs of electrodes can be deduced (see Table 6.1).

Summarizing, the possibility to gate graphene via NPA is demonstrated. Since gating efficiency of every gate depends on another connected gate (e.g., $\alpha_F^{FH} \neq \alpha_F^{FA}$, $\alpha_H^{FH} \neq \alpha_H^{GH}$, where α_X^{XY} is an efficiency of gate X while gates X and Y are measured), the overall efficiency depends on the entire configuration of all gates, or, more general, on the potential profile applied to the NPA. Thereby, G/NPA can be considered as a simple multi-terminal device with single output signal (graphene resistance) and ‘programmable’ functionality, defined by the applied top gate voltages.

6.3 Frequency response of GFET with NPA

Capacitive properties of nanoparticles inside the organic conductive materials let us to create devices with unconventional, bio-inspired properties, which can for example mimic biological neuron behavior [41, 42]. One of the main feature of a neuron is its frequency response. Since frequency-dependent hysteresis is observed in the gate dependence of the graphene with nanoparticles (Fig. 6.3d), the dynamics of the double-gating was studied.

10 V pulses were applied to two side gates of G/NPA device (namely, side gates F and H), and resistance of the graphene FET was measured. The measurements were performed with a sampling rate of 2, 8, 32 and 64 kHz (Hz = pts/s), and the duration of the pulse varied in the range of 1 to 10 pts for every frequency (e.g. for 32 kHz sampling rate the durations of the gate pulses were $\frac{1}{32000}$ s, $\frac{2}{32000}$ s, ...

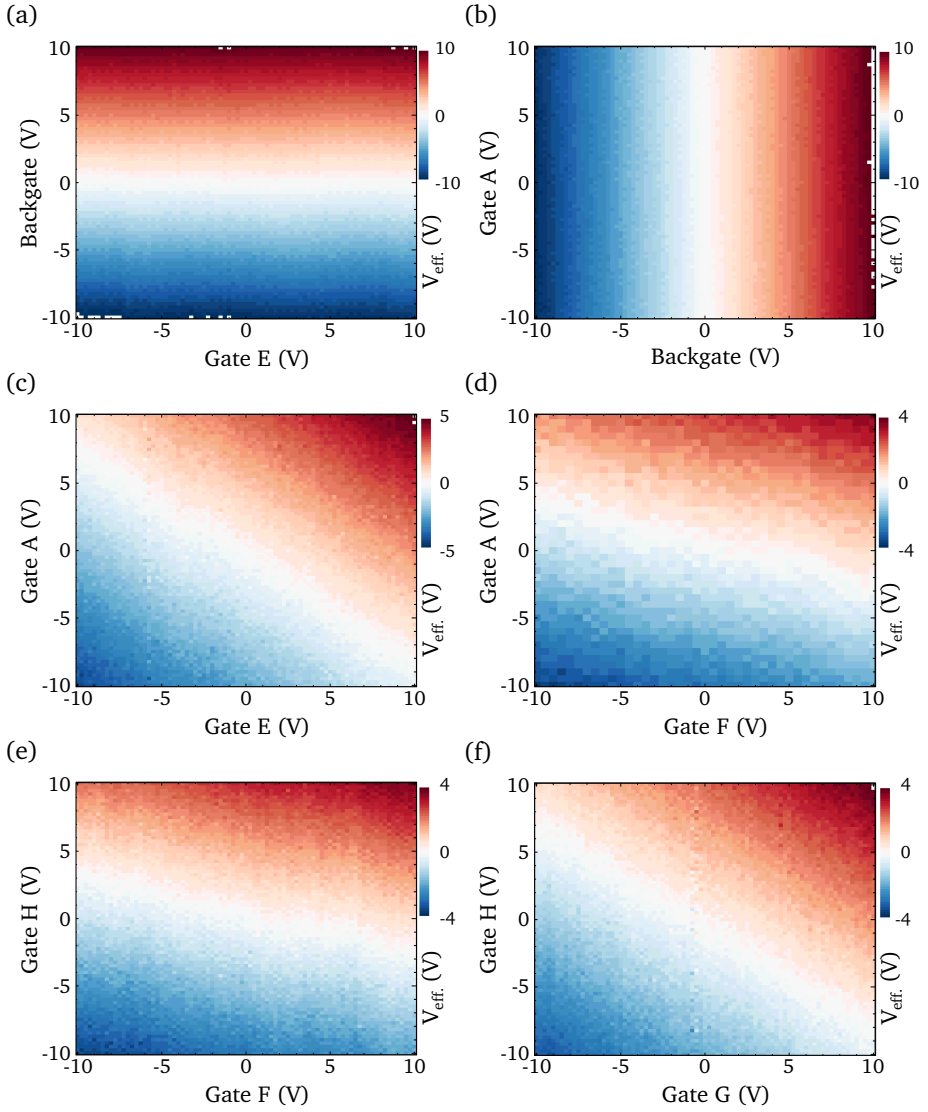


Figure 6.6: Gating efficiencies of G/NPA device for different pairs of electrodes.

$\frac{10}{32000}$ s).

The output of the device, i.e. resistance of GFET, was transformed into effective gate voltage as described in the previous section. The measurements for 2 kHz and 64 kHz sampling rate are shown in Figure 6.7. From all measured time dependencies the time constant of the response was deduced: $\tau_F^{FH} = 14 \pm 1 \mu\text{s}$, $\tau_H^{FH} = 23 \pm 1 \mu\text{s}$, $\tau_{F,H}^{FH} = 19 \pm 1 \mu\text{s}$. The resistances of the NPA between GFET and gates F and H are $R_F \approx 20 \text{ G}\Omega$ and $R_H \approx 40 \text{ G}\Omega$. Thereby, the effective capacitances of the device are $C_{\text{eff}} \approx \tau/R \sim (0.5 - 1) \text{ fF}$.

The amplitude of the response signal is shown in Figure 6.8. The responses for both gates $V_{F,10V}^{\text{eff}} \approx 2.1 \pm 0.2 \text{ V}$ and $V_{H,10V}^{\text{eff}} \approx 4.2 \pm 0.3 \text{ V}$ do not depend neither on the pulse duration, nor on the sampling rate (Fig. 6.9a). Corresponding gating efficiencies ($\alpha_{F,\text{pulse}}^{FH} = 0.21$ and $\alpha_{H,\text{pulse}}^{FH} = 0.42$) are slightly different from the ones measured in the IV mode ($\alpha_F^{FH} = 0.17$ and $\alpha_H^{FH} = 0.5$; Fig. 6.9b).

Considering an array as a plate capacitor, sheet capacitance of the NPA can be estimated as $C_{\square} = \frac{\epsilon\epsilon_0}{d} = \frac{2.7 \cdot 8.85 \cdot 10^{-12} \text{ F/m}}{1 \text{ nm}} = 2.4 \cdot 10^{-2} \text{ F/m}^2 = 24 \text{ fF}/\mu\text{m}^2$, where $d \approx 1 \text{ nm}$ is a length of the 1-octanethiol molecule and $\epsilon \approx 2.7$ is a relative permittivity of the octanethiol monolayer [143, 144]. The area of the array on top of graphene FET is about $10 \mu\text{m}^2$, which leads to the capacitance of $C_{\text{NPA}} \approx 250 \text{ fF}$. Thereby, only very small part of an array has a capacitive coupling to the graphene.

6.4 Overview and outlook

The gating of the graphene FET *via* stamped small-sized NP array as a top-gate with graphene electrodes was demonstrated. The gating efficiency depends on the potential profile applied to the NP array via the gates. The time response of the devices is defined by the capacitance properties of the NPA and lies in the range of microseconds, leading to the effective capacitance of $\sim 1 \text{ fF}$.

G/NPA devices attract more interest for further investigations such as the study of the influence of the functional molecules in NPA on the properties of an array. Extra functionality of the devices can be achieved by the ‘programming’ of the device by defining the potential profile on the NPA via all the gates.

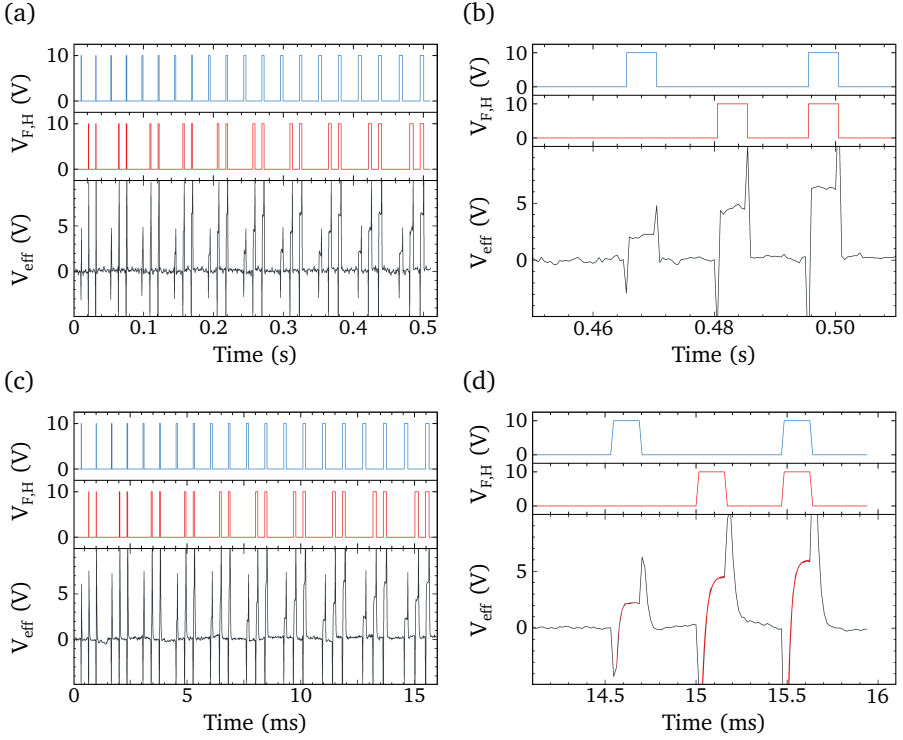


Figure 6.7: Measurements of G/NPA devices with 2 kHz (a, b) and 64 kHz (c, d) sampling rate. (a, c) Response of GFET (V_{eff} , bottom panel) with respect to the pulses applied to gates F (top panel) and H (central panel). Duration of the pulses is varied from 1 pt to 10 pts. (b, d) Response for the longest (10 pts) pulses with a sampling rate of 2 kHz. No time dependence is observed. (d) Analysis of the response for the longest (10 pts) pulses for a sampling rate of 64 kHz. Red curves on the bottom panel denote exponential fit of the response signal. Deduced time constants are $\tau_F = 14 \mu\text{s}$, $\tau_H = 23 \mu\text{s}$, $\tau_{F,H} = 19 \mu\text{s}$.

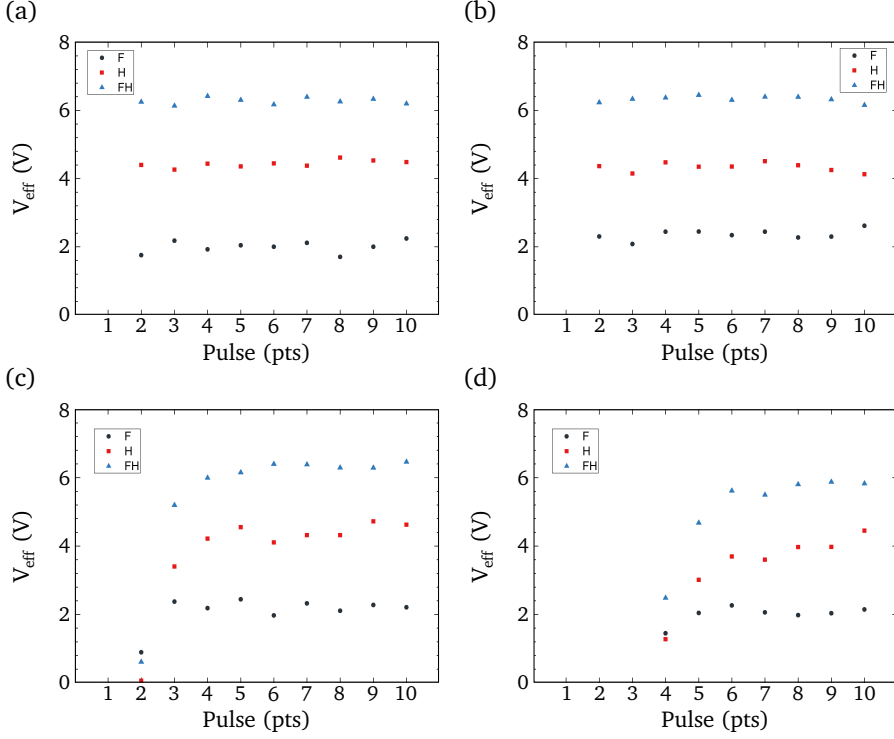


Figure 6.8: Analysis of response amplitude with respect to the pulse duration. Sampling rate is 2 kHz, 8 kHz, 32 kHz, 64 kHz for a–d, respectively. Note that the response corresponds to the 10 V amplitude of the gate pulses.

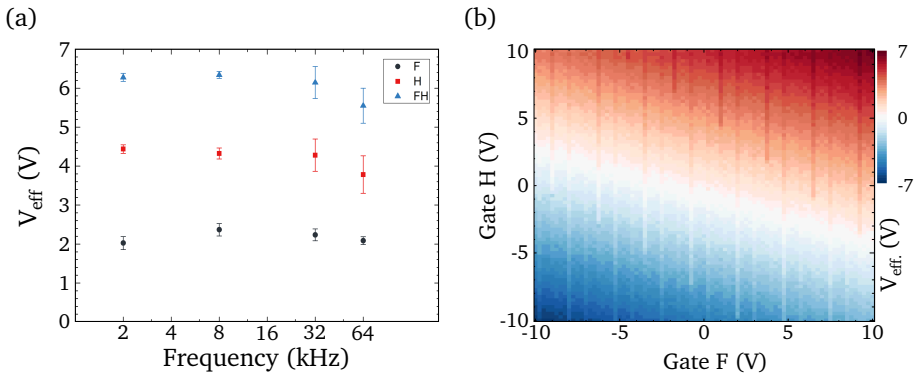


Figure 6.9: (a) Frequency response of G/NPA with respect to the sampling rate. (b) Double gating of the the same device in IV mode. The gating efficiencies are $\alpha_F^{\text{FH}} = 0.17$ and $\alpha_H^{\text{FH}} = 0.5$.

Conclusion and outlook

This thesis covers a wide range of experimental investigations in the field of molecular electronics from the level of individual molecular junctions to hybrid devices combining self-assembled molecular networks and graphene.

Chapter 1 describes the general principles of electrical single-molecule measurements using mechanically-controlled break junction technique in liquid environment at room temperature, and approaches for the analysis of measured data.

In Chapter 2, an in-depth experimental characterization and analysis of molecular junctions formed by isocyanide molecules is presented. The formation of molecular junctions for a simple 1,4-benzenediisocyanide (BdNC) molecule was studied at different concentrations and for the bi-substituted derivatives MBdNC and tBuBdNC. We observed the presence of two stable configurations in the molecular junctions for a 100 μ M BdNC solution, which was attributed to the chaining of the molecules with extra gold atoms in the chain. This effect was confirmed experimentally by analysis of closing traces, by the measurements of the molecules with side-groups and at lower concentrations (where intermolecular interactions are suppressed), as well as theoretically, using ab-initio DFT calculations. We also assumed the formation of multi-molecular junctions at higher concentrations, which can cause the observed asymmetry of conductance peaks and the different slope of the conductance plateaus.

Chapter 3 describes experimental and theoretical approaches to investigate the mechanical stability of π -stacked molecular junctions and its influence on the electrical properties. We demonstrated that fluctuations of the molecules in π -stacked junctions have a significant impact on the conductance.

Chapter 4 shows the general overview of the nanoparticle arrays: methods of fabrications, characterization and functionalities.

In Chapter 5 we introduced graphene as a contact material for nanoparticle arrays. Graphene is a good electrical conductor and graphene electrodes can be

easily patterned to arbitrary desired shapes. Thanks to the ultimate thickness of graphene, the uniformity and flatness of the nanoparticle array is not affected after transfer, and any uncertainties in contact geometry are negligible. The developed hybrid graphene–nanoparticle array (G/NPA) devices keep the functionality of the ‘conventional’ devices with gold evaporated electrodes: the possibilities to exchange the molecules in the array and to perform optical switching with azobenzene-covered nanoparticles were demonstrated.

The first steps towards building a hybrid ‘neuron-inspired’ device have been described in Chapter 6, which covers the investigations of G/NPA device as a graphene field-effect transistor with nanoparticle array acting like a top gate. We observed that the presence of an NPA on graphene decreases the back-gating efficiency due to capacitive coupling of an array to graphene. We also demonstrated the gating of the graphene device via the deposited nanoparticle array. The gating efficiency is defined by the potential profile applied to the array through graphene electrodes. To investigate the possibilities to use our hybrid device to observe STP or LTP effects, frequency measurements were performed, which demonstrated typical device response times of a few tens of microseconds.

Overall, it is shown that an in-depth analysis of all measured data for molecular junctions formation, including the rarely analyzed closing conductance traces as well as the length and shape of conductance plateaus, is very important and provides useful information for understanding the microscopic nature of the processes happening at the molecular level. These processes define the electrical properties and the stability of single molecular junctions and, consequently, the next level of molecular junctions integration — molecular networks. Molecular networks implemented in nanoparticle arrays is a promising platform where functionality can be tuned using different molecular compounds as active elements within the network. By introducing graphene into nanoparticle arrays as a contact material and as an active graphene transistor using integration of top-down and bottom-up approaches, we created a new type of hybrid devices with additional possibilities to implement electrical functionality, e.g., by creating a potential profile on the gate of graphene FET.

Multi-terminal NPA-based device represents a convenient platform to perform massively parallel processing of electrical signals. Investigations of the frequency response of these hybrid devices are promising for mimicking the neuronal synaptic functionality and open unprecedented possibilities [36]. Research on such devices not only may help better understanding the nature of the brain functionality, but also paves the road to build novel, unconventional type of computing machines with higher level of integration than existing CMOS-based devices, to perform robust and fault-tolerant information processing at the molecular scale.

Bibliography

- [1] N. Koumura *et al.*, “Light-driven monodirectional molecular rotor”, *Nature*, vol. 401, no. 6749, pp. 152–155, 1999. DOI: 10.1038/43646.
- [2] N. Katsonis *et al.*, “Electrically driven directional motion of a four-wheeled molecule on a metal surface”, *Nature*, vol. 479, no. 7372, pp. 208–211, 2011. DOI: 10.1038/nature10587.
- [3] J.-P. Sauvage, “Transition Metal-Containing Rotaxanes and Catenanes in Motion: Toward Molecular Machines and Motors”, *Accounts of Chemical Research*, vol. 31, no. 10, pp. 611–619, 1998. DOI: 10.1021/ar960263r.
- [4] M. C. Jimenez-Molero, C. Dietrich-Buchecker, and J.-P. Sauvage, “Towards artificial muscles at the nanometric level”, *Chemical Communications*, no. 14, p. 1613, 2003. DOI: 10.1039/b302326p.
- [5] C. P. Collier *et al.*, “Electronically configurable molecular-based logic gates”, *Science*, vol. 285, no. 5426, pp. 391–394, 1999. DOI: 10.1126/science.285.5426.391.
- [6] D. D. Eley and G. D. Parfitt, “Semiconductivity of organic substances. II”, *Transactions of the Faraday Society*, vol. 51, no. 17, pp. 1529–1539, 1955. DOI: 10.1039/tf9555101529.
- [7] D. D. Eley and D. I. Spivey, “The semiconductivity of organic substances. Part 6. A range of proteins”, *Transactions of the Faraday Society*, vol. 56, no. 4, pp. 1432–1442, 1960. DOI: 10.1039/tf9605601432.
- [8] D. D. Eley and D. I. Spivey, “Semiconductivity of organic substances. Part 9. Nucleic acid in the dry state”, *Transactions of the Faraday Society*, vol. 58, pp. 411–415, 1962. DOI: 10.1039/tf9625800411.
- [9] B. Mann and H. Kuhn, “Tunneling through Fatty Acid Salt Monolayers”, *Journal of Applied Physics*, vol. 42, no. 11, p. 4398, 1971. DOI: 10.1063/1.1659785.
- [10] A. Aviram and M. A. Ratner, “Molecular rectifiers”, *Chemical Physics Letters*, vol. 29, no. 2, pp. 277–283, 1974. DOI: 10.1016/0009-2614(74)85031-1.

-
- [11] A. Nitzan and M. A. Ratner, "Electron Transport in Molecular Wire Junctions", *Science*, vol. 300, no. 5624, pp. 1384–1389, 2003. DOI: 10.1126/science.1081572.
- [12] S. J. van der Molen and P. Liljeroth, "Charge transport through molecular switches", *Journal of Physics: Condensed Matter*, vol. 22, no. 13, p. 133 001, 2010. DOI: 10.1088/0953-8984/22/13/133001.
- [13] S. Y. Quek *et al.*, "Mechanically controlled binary conductance switching of a single-molecule junction", *Nature Nanotechnology*, vol. 4, no. 4, pp. 230–234, 2009. DOI: 10.1038/nnano.2009.10.
- [14] I. Díez-Pérez *et al.*, "Rectification and stability of a single molecular diode with controlled orientation.", *Nature chemistry*, vol. 1, no. 8, pp. 635–41, 2009. DOI: 10.1038/nchem.392.
- [15] A. Batra *et al.*, "Tuning Rectification in Single-Molecular Diodes", *Nano Letters*, vol. 13, no. 12, pp. 6233–6237, 2013. DOI: 10.1021/nl403698m.
- [16] M. L. Perrin *et al.*, "A gate-tunable single-molecule diode", *Nanoscale*, vol. 8, no. 16, pp. 8919–8923, 2016. DOI: 10.1039/C6NR00735J.
- [17] S. Kubatkin *et al.*, "Single-electron transistor of a single organic molecule with access to several redox states.", *Nature*, vol. 425, no. 6959, pp. 698–701, 2003. DOI: 10.1038/nature02010.
- [18] H. Song *et al.*, "Observation of molecular orbital gating", *Nature*, vol. 462, no. 7276, pp. 1039–1043, 2009. DOI: 10.1038/nature08639.
- [19] E. Lörtscher *et al.*, "Reversible and Controllable Switching of a Single-Molecule Junction", *Small*, vol. 2, no. 8-9, pp. 973–977, 2006. DOI: 10.1002/sml.200600101.
- [20] J. E. Green *et al.*, "A 160-kilobit molecular electronic memory patterned at 10¹¹ bits per square centimetre", *Nature*, vol. 445, no. 7126, pp. 414–417, 2007. DOI: 10.1038/nature05462.
- [21] G. Binnig *et al.*, "Surface studies by scanning tunneling microscopy", *Physical review letters*, no. 1, pp. 57–61, 1982. DOI: 10.1103/PhysRevLett.49.57.
- [22] G. Binnig, C. F. Quate, and C. Gerber, "Atomic Force Microscope", *Physical Review Letters*, vol. 56, no. 9, pp. 930–933, 1986. DOI: 10.1103/PhysRevLett.56.930.
- [23] C. Joachim *et al.*, "Electronic Transparence of a Single C60 Molecule", *Physical Review Letters*, vol. 74, no. 11, pp. 2102–2105, 1995. DOI: 10.1103/PhysRevLett.74.2102.
- [24] J. Moreland and J. W. Ekin, "Electron tunneling experiments using Nb-Sn "break" junctions", *Journal of Applied Physics*, vol. 58, no. 10, p. 3888, 1985. DOI: 10.1063/1.335608.
- [25] C. J. Muller, J. M. van Ruitenbeek, and L. J. de Jongh, "Conductance and supercurrent discontinuities in atomic-scale metallic constrictions of variable width", *Physical Review Letters*, vol. 69, no. 1, pp. 140–143, 1992. DOI: 10.1103/PhysRevLett.69.140.
- [26] C. Muller, J. van Ruitenbeek, and L. de Jongh, "Experimental observation of the transition from weak link to tunnel junction", *Physica C: Superconductivity*, vol. 191, no. 3-4, pp. 485–504, 1992. DOI: 10.1016/0921-4534(92)90947-B.

- [27] M. A. Reed *et al.*, “Conductance of a Molecular Junction”, *Science*, vol. 278, no. 5336, pp. 252–254, 1997. DOI: 10.1126/science.278.5336.252.
- [28] R. H. M. Smit *et al.*, “Measurement of the conductance of a hydrogen molecule”, *Nature*, vol. 419, no. 6910, pp. 906–909, 2002. DOI: 10.1038/nature01103.
- [29] B. Xu and N. J. Tao, “Measurement of Single-Molecule Resistance by Repeated Formation of Molecular Junctions”, *Science*, vol. 301, no. 5637, pp. 1221–1223, 2003. DOI: 10.1126/science.1087481.
- [30] H. Park *et al.*, “Fabrication of metallic electrodes with nanometer separation by electromigration”, *Applied Physics Letters*, vol. 75, no. 1999, pp. 301–303, 1999. DOI: 10.1063/1.124354.
- [31] H. Park *et al.*, “Nanomechanical oscillations in a single-C₆₀ transistor”, *Nature*, vol. 407, no. 6800, pp. 57–60, 2000. DOI: 10.1038/35024031.
- [32] R. C. Chiechi *et al.*, “Eutectic gallium-indium (EGaIn): A moldable liquid metal for electrical characterization of self-assembled monolayers”, *Angewandte Chemie - International Edition*, vol. 47, no. 1, pp. 142–144, 2008. DOI: 10.1002/anie.200703642.
- [33] D. S. Modha. (2012). Introducing a Brain-inspired Computer. TrueNorth’s neurons to revolutionize system architecture, [Online]. Available: <http://www.research.ibm.com/articles/brain-chip.shtml>.
- [34] J. Von Neumann and R. Kurzweil, *The computer and the brain*. Yale University Press, 2012.
- [35] J. Von Neumann and M. D. Godfrey, “First Draft of a Report on the EDVAC”, *IEEE Annals of the History of Computing*, vol. 15, no. 4, pp. 27–75, 1993.
- [36] A. Demming, J. K. Gimzewski, and D. Vuillaume, “Synaptic electronics”, *Nanotechnology*, vol. 24, no. 38, p. 380 201, 2013. DOI: 10.1088/0957-4484/24/38/380201.
- [37] A. Schnitzler and J. Gross, “Normal and pathological oscillatory communication in the brain”, *Nature Reviews Neuroscience*, vol. 6, no. 4, pp. 285–296, 2005. DOI: 10.1038/nrn1650.
- [38] M. Di Ventra and Y. V. Pershin, “The parallel approach”, *Nature Physics*, vol. 9, no. 4, pp. 200–202, 2013. DOI: 10.1038/nphys2566.
- [39] L. F. Abbott *et al.*, “Synaptic depression and cortical gain control”, *Science*, vol. 275, no. 5297, pp. 221–224, 1997. DOI: 10.1126/science.275.5297.221.
- [40] T. Ohno *et al.*, “Short-term plasticity and long-term potentiation mimicked in single inorganic synapses”, *Nature materials*, vol. 10, no. 8, pp. 591–595, 2011. DOI: 10.1038/nmat3054.
- [41] F. Alibart *et al.*, “An Organic Nanoparticle Transistor Behaving as a Biological Spiking Synapse”, *Advanced Functional Materials*, vol. 20, no. 2, pp. 330–337, 2010. DOI: 10.1002/adfm.200901335.
- [42] F. Alibart *et al.*, “A Memristive Nanoparticle/Organic Hybrid Synapstor for Neuroin-inspired Computing”, *Advanced Functional Materials*, vol. 22, no. 3, pp. 609–616, 2012. DOI: 10.1002/adfm.201101935.

- [43] J. M. Tour *et al.*, “Nanocell logic gates for molecular computing”, *IEEE Transactions on Nanotechnology*, vol. 1, no. 2, pp. 100–108, 2002. DOI: 10.1109/tnano.2002.804744.
- [44] J. Chen *et al.*, “Large on-off ratios and negative differential resistance in a molecular electronic device”, *Science*, vol. 286, no. 5444, pp. 1550–1552, 1999. DOI: 10.1126/science.286.5444.1550.
- [45] S. K. Bose *et al.*, “Evolution of a designless nanoparticle network into reconfigurable Boolean logic”, *Nature Nanotechnology*, vol. 10, no. 12, pp. 1048–1052, 2015. DOI: 10.1038/nnano.2015.207.
- [46] L. O. Chua, “Memristor-The missing circuit element”, *IEEE Transactions on Circuit Theory*, vol. 18, no. 5, pp. 507–519, 1971. DOI: 10.1109/tct.1971.1083337.
- [47] D. B. Strukov *et al.*, “The missing memristor found”, *Nature*, vol. 453, no. 7191, pp. 80–83, 2008. DOI: 10.1038/nature06932.
- [48] T. Prodromakis, C. Toumazou, and L. Chua, “Two centuries of memristors”, *Nature materials*, vol. 11, no. 6, pp. 478–481, 2012. DOI: 10.1038/nmat3338.
- [49] M. Di Ventra *et al.*, “Circuit Elements With Memory: Memristors, Memcapacitors, and Meminductors”, *Proceedings of the IEEE*, vol. 97, no. 10, pp. 1717–1724, 2009. DOI: 10.1109/jproc.2009.2021077.
- [50] A. Thomas, “Memristor-based neural networks”, *Journal of Physics D: Applied Physics*, vol. 46, no. 9, p. 93 001, 2013. DOI: 10.1088/0022-3727/46/9/093001.
- [51] Y. V. Pershin and M. Di Ventra, “Solving mazes with memristors: A massively parallel approach”, *Physical Review E*, vol. 84, no. 4, p. 46 703, 2011. DOI: 10.1103/PhysRevE.84.046703.
- [52] L. Grüter *et al.*, “Electrical Conductance of Atomic Contacts in Liquid Environments”, *Small*, vol. 1, no. 11, pp. 1067–1070, 2005. DOI: 10.1002/smll.200500145.
- [53] I. Yanson and O. Shklyarevskij, “Point-contact spectroscopy of metallic alloys and compounds”, Russian, *Fizika Nizkikh Temperatur*, vol. 12, no. 9, pp. 899–933, 1986.
- [54] C. Zhou *et al.*, “Microfabrication of a mechanically controllable break junction in silicon”, *Applied Physics Letters*, vol. 67, p. 1160, 1995.
- [55] X. Li *et al.*, “Controlling charge transport in single molecules using electrochemical gate”, *Faraday Discussions*, vol. 131, pp. 111–120, 2006. DOI: 10.1039/b505666g.
- [56] J. He *et al.*, “Electrochemical origin of voltage-controlled molecular conductance switching”, *Journal of the American Chemical Society*, vol. 128, no. 46, pp. 14 828–14 835, 2006. DOI: 10.1021/ja0635433.
- [57] S. Guo, J. M. Artés, and I. Dérez, “Electrochemically-gated single-molecule electrical devices”, *Electrochimica Acta*, vol. 110, pp. 741–753, 2013. DOI: 10.1016/j.electacta.2013.03.146.
- [58] M. T. González *et al.*, “Electrical conductance of molecular junctions by a robust statistical analysis”, *Nano Letters*, vol. 6, no. 10, pp. 2238–2242, 2006. DOI: 10.1021/nl061581e.
- [59] N. Agraït, A. Levy Yeyati, and J. M. van Ruitenbeek, “Quantum properties of atom-sized conductors”, *Physics Reports*, vol. 377, no. 2-3, pp. 81–279, 2003. DOI: 10.1016/S0370-1573(02)00633-6.

- [60] J. M. van Ruitenbeek *et al.*, “Adjustable nanofabricated atomic size contacts”, *Review of Scientific Instruments*, vol. 67, no. 1, p. 108, 1996. DOI: 10.1063/1.1146558.
- [61] S. Vrouwe *et al.*, “Mechanics of lithographically defined break junctions”, *Physical Review B*, vol. 71, no. 3, pp. 1–7, 2005. DOI: 10.1103/PhysRevB.71.035313.
- [62] J. G. Simmons, “Generalized Formula for the Electric Tunnel Effect between Similar Electrodes Separated by a Thin Insulating Film”, *Journal of Applied Physics*, vol. 34, no. 6, p. 1793, 1963. DOI: 10.1063/1.1702682.
- [63] J. G. Kushmerick *et al.*, “Effect of Bond-Length Alternation in Molecular Wires”, *Journal of the American Chemical Society*, vol. 124, no. 36, pp. 10 654–10 655, 2002. DOI: 10.1021/ja027090n.
- [64] D. Roldan *et al.*, “Charge transport in photoswitchable dimethyldihydropyrene-type single-molecule junctions”, *Journal of the American Chemical Society*, vol. 135, no. 16, pp. 5974–5977, 2013. DOI: 10.1021/ja401484j.
- [65] Y. Kim *et al.*, “Charge Transport in Azobenzene-Based Single-Molecule Junctions”, *Physical Review Letters*, vol. 109, no. 22, p. 226 801, 2012. DOI: 10.1103/PhysRevLett.109.226801.
- [66] S. Martin *et al.*, “The impact of E-Z photo-isomerization on single molecular conductance”, *Nano Letters*, vol. 10, no. 6, pp. 2019–2023, 2010. DOI: 10.1021/nl9042455.
- [67] F. Chen *et al.*, “A molecular switch based on potential-induced changes of oxidation state”, *Nano Letters*, vol. 5, no. 3, pp. 503–506, 2005. DOI: 10.1021/nl0478474.
- [68] N. J. Kay *et al.*, “Single-molecule electrochemical gating in ionic liquids”, *Journal of the American Chemical Society*, vol. 134, no. 40, pp. 16 817–16 826, 2012. DOI: 10.1021/ja307407e.
- [69] R. Frisenda *et al.*, “Mechanically controlled quantum interference in individual π -stacked dimers”, *Nature Chemistry*, vol. 8, no. 12, pp. 1099–1104, 2016. DOI: 10.1038/nchem.2588.
- [70] C. M. Guédon *et al.*, “Observation of quantum interference in molecular charge transport”, *Nature Nanotechnology*, vol. 7, no. 5, pp. 305–309, 2012. DOI: 10.1038/nnano.2012.37.
- [71] T. Juffmann *et al.*, “Real-time single-molecule imaging of quantum interference”, *Nature Nanotechnology*, vol. 7, no. 5, pp. 297–300, 2012. DOI: 10.1038/nnano.2012.34.
- [72] D. Z. Manrique *et al.*, “A quantum circuit rule for interference effects in single-molecule electrical junctions”, *Nature communications*, vol. 6, pp. 1–8, 2015. DOI: 10.1038/ncomms7389.
- [73] C. R. Arroyo *et al.*, “Quantum interference effects at room temperature in OPV-based single-molecule junctions”, *Nanoscale research letters*, vol. 8, no. 1, p. 234, 2013. DOI: 10.1186/1556-276X-8-234.
- [74] C. Li *et al.*, “Charge transport in single Au|alkanedithiol|Au Junctions: Coordination geometries and conformational degrees of freedom”, *Journal of the American Chemical Society*, vol. 130, no. 17, p. 19, 2008. DOI: 10.1021/ja0762386.

- [75] L. Venkataraman *et al.*, “Single-molecule circuits with well-defined molecular conductance”, *Nano Letters*, vol. 6, no. 3, pp. 458–462, 2006. DOI: 10.1021/nl052373.
- [76] L. Venkataraman *et al.*, “Dependence of single-molecule junction conductance on molecular conformation”, *Nature*, vol. 442, no. 7105, pp. 904–907, 2006. DOI: 10.1038/nature05037.
- [77] M. S. Hybertsen *et al.*, “Amine-linked single-molecule circuits: systematic trends across molecular families”, *Journal of Physics: Condensed Matter*, vol. 20, no. 37, p. 374 115, 2008. DOI: 10.1088/0953-8984/20/37/374115.
- [78] A. Mishchenko *et al.*, “Single-molecule junctions based on nitrile-terminated biphenyls: a promising new anchoring group”, *Journal of the American Chemical Society*, vol. 133, no. 2, pp. 184–187, 2011. DOI: 10.1021/ja107340t.
- [79] L. A. Zotti *et al.*, “Revealing the Role of Anchoring Groups in the Electrical Conduction Through Single-Molecule Junctions”, *Small*, vol. 6, no. 14, pp. 1529–1535, 2010. DOI: 10.1002/sml.200902227.
- [80] B. Kim *et al.*, “Correlation between HOMO alignment and contact resistance in molecular junctions: aromatic thiols versus aromatic isocyanides”, *Journal of the American Chemical Society*, vol. 128, no. 15, pp. 4970–4971, 2006. DOI: 10.1021/ja0607990.
- [81] W. Hong *et al.*, “Single Molecular Conductance of Tolanes: Experimental and Theoretical Study on the Junction Evolution Dependent on the Anchoring Group”, *Journal of the American Chemical Society*, vol. 134, no. 4, pp. 2292–2304, 2012. DOI: 10.1021/ja209844r.
- [82] C.-H. Ko *et al.*, “Superior contact for single-molecule conductance: electronic coupling of thiolate and isothiocyanate on Pt, Pd, and Au”, *Journal of the American Chemical Society*, vol. 132, no. 2, pp. 756–764, 2010. DOI: 10.1021/ja9084012.
- [83] F. Chen *et al.*, “Effect of anchoring groups on single-molecule conductance: comparative study of thiol-, amine-, and carboxylic-acid-terminated molecules”, *Journal of the American Chemical Society*, vol. 128, no. 49, pp. 15 874–15 881, 2006. DOI: 10.1021/ja065864k.
- [84] J. Chen *et al.*, “Electronic transport through metal–1,4-phenylene diisocyanide–metal junctions”, *Chemical Physics Letters*, vol. 313, no. 5-6, pp. 741–748, 1999. DOI: 10.1016/S0009-2614(99)01060-X.
- [85] E. Lörtscher *et al.*, “Influence of the Anchor Group on Charge Transport through Single-Molecule Junctions”, *Chemphyschem : A European journal of chemical physics and physical chemistry*, vol. 12, no. 9, pp. 1677–1682, 2011. DOI: 10.1002/cphc.201000960.
- [86] M. Kiguchi *et al.*, “Conductance of a single molecule anchored by an isocyanide substituent to gold electrodes”, *Applied Physics Letters*, vol. 89, no. 21, p. 213 104, 2006. DOI: 10.1063/1.2392816.
- [87] X. Xiao, B. Xu, and N. J. Tao, “Measurement of Single Molecule Conductance: Benzenedithiol and Benzenedimethanethiol”, *Nano Letters*, vol. 4, no. 2, pp. 267–271, 2004. DOI: 10.1021/nl035000m.

- [88] S. Y. Quek *et al.*, “Amine-gold linked single-molecule circuits: experiment and theory”, *Nano Letters*, vol. 7, no. 11, pp. 3477–3482, 2007. DOI: 10.1021/nl072058i.
- [89] S. Nakashima, Y. Takahashi, and M. Kiguchi, “Effect of the environment on the electrical conductance of the single benzene-1,4-diamine molecule junction”, *Beilstein journal of nanotechnology*, vol. 2, no. 1, pp. 755–759, 2011. DOI: 10.3762/bjnano.2.83.
- [90] Y. Kim *et al.*, “Benzenedithiol: A Broad-Range Single-Channel Molecular Conductor”, *Nano Letters*, vol. 11, no. 9, pp. 3734–3738, 2011. DOI: 10.1021/nl201777m.
- [91] K. Ishizuka *et al.*, “Effect of Molecule–Electrode Contacts on Single-Molecule Conductivity of π -Conjugated System Measured by Scanning Tunneling Microscopy under Ultrahigh Vacuum”, *Japanese Journal of Applied Physics*, vol. 45, no. 3B, pp. 2037–2040, 2006. DOI: 10.1143/JJAP.45.2037.
- [92] E. Lörtscher *et al.*, “Transport Properties of a Single-Molecule Diode”, *ACS Nano*, vol. 6, no. 6, pp. 4931–4939, 2012. DOI: 10.1021/nn300438h.
- [93] Y. Kim *et al.*, “Charge transport characteristics of diarylethene photoswitching single-molecule junctions”, *Nano Letters*, vol. 12, no. 7, pp. 3736–3742, 2012. DOI: 10.1021/nl3015523.
- [94] M. Baghernejad *et al.*, “Highly-effective gating of single-molecule junctions: an electrochemical approach”, *Chem. Commun.*, vol. 50, no. 100, pp. 15 975–15 978, 2014. DOI: 10.1039/c4cc06519k.
- [95] K. Yoshida *et al.*, “Correlation of breaking forces, conductances and geometries of molecular junctions”, *Scientific Reports*, vol. 5, p. 9002, 2015. DOI: 10.1038/srep09002.
- [96] V. Kaliginedi *et al.*, “Correlations between Molecular Structure and Single-Junction Conductance: A Case Study with Oligo(phenylene-ethynylene)-Type Wires”, *Journal of the American Chemical Society*, vol. 134, no. 11, pp. 5262–5275, 2012. DOI: 10.1021/ja211555x.
- [97] J. J. Stapleton *et al.*, “Self-assembly, characterization, and chemical stability of isocyanide-bound molecular wire monolayers on gold and palladium surfaces”, *Langmuir*, vol. 21, no. 24, pp. 11 061–11 070, 2005. DOI: 10.1021/la051094z.
- [98] M. Teresa González *et al.*, “Conductance values of alkanedithiol molecular junctions”, *New Journal of Physics*, vol. 10, no. 6, p. 065 018, 2008. DOI: 10.1088/1367-2630/10/6/065018.
- [99] J. Brunner *et al.*, “Random telegraph signals in molecular junctions”, *Journal of Physics: Condensed Matter*, vol. 26, no. 47, p. 474 202, 2014. DOI: 10.1088/0953-8984/26/47/474202.
- [100] W. H. A. Thijssen *et al.*, “Oxygen-enhanced atomic chain formation”, *Physical Review Letters*, vol. 96, no. 2, pp. 2–5, 2006. DOI: 10.1103/PhysRevLett.96.026806.
- [101] Z. Balogh, P. Makk, and A. Halbritter, “Alternative types of molecule-decorated atomic chains in Au–CO–Au single-molecule junctions”, *Beilstein journal of nanotechnology*, vol. 6, pp. 1369–1376, 2015. DOI: 10.3762/bjnano.6.141.

- [102] Y. Kim *et al.*, “Characteristics of Amine-Ended and Thiol-Ended Alkane Single-Molecule Junctions Revealed by Inelastic Electron Tunneling Spectroscopy”, *ACS Nano*, vol. 5, no. 5, pp. 4104–4111, 2011. DOI: 10.1021/nn200759s.
- [103] R. Vardimon *et al.*, “Probing the Orbital Origin of Conductance Oscillations in Atomic Chains”, *Nano Letters*, vol. 14, no. 6, pp. 2988–2993, 2014. DOI: 10.1021/nl4041737.
- [104] P. Makk *et al.*, “Pulling platinum atomic chains by carbon monoxide molecules”, *Nanoscale*, vol. 4, no. 15, p. 4739, 2012. DOI: 10.1039/c2nr30832k.
- [105] T. Yelin *et al.*, “Atomically Wired Molecular Junctions: Connecting a Single Organic Molecule by Chains of Metal Atoms”, *Nano Letters*, vol. 13, no. 5, pp. 1956–1961, 2013. DOI: 10.1021/nl304702z.
- [106] M. J. Irwin *et al.*, “Rigid-Rod Polymers and Model Compounds with Gold(I) Centers Bridged by Diisocyanides and Diacetylides”, *Organometallics*, vol. 15, no. 1, pp. 51–57, 1996. DOI: 10.1021/om950659r.
- [107] W. Schneider, A. Bauer, and H. Schmidbaur, “(Isocyanide)gold(I) Thiosalicylates: Supramolecular Assembly Based on both Aurophilic and Hydrogen Bonding”, *Organometallics*, vol. 15, no. 26, pp. 5445–5446, 1996. DOI: 10.1021/om960682s.
- [108] L. Venkataraman *et al.*, “Electronics and chemistry: Varying single-molecule junction conductance using chemical substituents”, *Nano Letters*, vol. 7, no. 2, pp. 502–506, 2007. DOI: 10.1021/nl062923j.
- [109] S. Martín *et al.*, “Identifying Diversity in Nanoscale Electrical Break Junctions”, *Journal of the American Chemical Society*, vol. 132, no. 26, pp. 9157–9164, 2010. DOI: 10.1021/ja103327f.
- [110] R. Huber *et al.*, “Electrical conductance of conjugated oligomers at the single molecule level”, *Journal of the American Chemical Society*, vol. 130, no. 3, pp. 1080–1084, 2008. DOI: 10.1021/ja0767940.
- [111] E. Lörtscher, H. B. Weber, and H. Riel, “Statistical Approach to Investigating Transport through Single Molecules”, *Physical Review Letters*, vol. 98, no. 17, p. 176807, 2007. DOI: 10.1103/PhysRevLett.98.176807.
- [112] M. G. Reuter *et al.*, “Signatures of cooperative effects and transport mechanisms in conductance histograms”, *Nano Letters*, vol. 12, no. 5, pp. 2243–2248, 2012. DOI: 10.1021/nl204379j.
- [113] P. D. Williams and M. G. Reuter, “Level Alignments and Coupling Strengths in Conductance Histograms: The Information Content of a Single Channel Peak”, *The Journal of Physical Chemistry C*, p. 130312140209000, 2013. DOI: 10.1021/jp310180s.
- [114] Y. Imry and R. Landauer, “Conductance viewed as transmission”, *Reviews of Modern Physics*, vol. 71, no. 2, 1999. DOI: 10.1103/RevModPhys.71.S306.
- [115] T. Ghane *et al.*, “Interplay between Mechanical and Electronic Degrees of Freedom in π -Stacked Molecular Junctions: From Single Molecules to Mesoscopic Nanoparticle Networks”, *The Journal of Physical Chemistry C*, vol. 119, no. 11, pp. 6344–6355, 2015. DOI: 10.1021/jp512524z.

- [116] L. Yuan *et al.*, “A Molecular Diode with a Statistically Robust Rectification Ratio of Three Orders of Magnitude”, *Nano Letters*, vol. 15, no. 8, pp. 5506–5512, 2015. DOI: 10.1021/acs.nanolett.5b02014.
- [117] L. Yuan *et al.*, “Controlling the direction of rectification in a molecular diode”, *Nature communications*, vol. 6, p. 6324, 2015. DOI: 10.1038/ncomms7324.
- [118] B. Capozzi *et al.*, “Single-molecule diodes with high rectification ratios through environmental control”, *Nature Nanotechnology*, vol. 10, no. 6, pp. 522–527, 2015. DOI: 10.1038/nnano.2015.97.
- [119] J. Trasobares *et al.*, “A 17 GHz molecular rectifier”, *Nature Communications*, vol. 7, p. 12850, 2016. DOI: 10.1038/ncomms12850.
- [120] S. Wu *et al.*, “Molecular junctions based on aromatic coupling”, *Nature Nanotechnology*, vol. 3, no. 9, pp. 569–574, 2008. DOI: 10.1038/nnano.2008.237.
- [121] J. Liao *et al.*, “Reversible Formation of Molecular Junctions in 2D Nanoparticle Arrays”, *Advanced Materials*, vol. 18, no. 18, pp. 2444–2447, 2006. DOI: 10.1002/adma.200601001.
- [122] D. van der Spoel *et al.*, “GROMACS: Fast, flexible, and free”, *Journal of Computational Chemistry*, vol. 26, no. 16, pp. 1701–1718, 2005. DOI: 10.1002/jcc.20291.
- [123] T. Ghane *et al.*, “Modeling of Solvent Effects in the Electrical Response of π -Stacked Molecular Junctions”, *The Journal of Physical Chemistry C*, vol. 119, no. 34, pp. 20201–20209, 2015. DOI: 10.1021/acs.jpcc.5b06867.
- [124] J. Liao *et al.*, “Ordered nanoparticle arrays interconnected by molecular linkers: Electronic and optoelectronic properties”, *Chemical Society Reviews*, vol. 44, no. 4, pp. 999–1014, 2015. DOI: 10.1039/c4cs00225c.
- [125] J. Liao *et al.*, “Interlinking Au nanoparticles in 2D arrays via conjugated dithiolated molecules”, *New Journal of Physics*, vol. 10, no. 6, p. 65019, 2008. DOI: 10.1088/1367-2630/10/6/065019.
- [126] L. Bernard *et al.*, “Spectroscopy of Molecular Junction Networks Obtained by Place Exchange in 2D Nanoparticle Arrays”, *The Journal of Physical Chemistry C*, vol. 111, no. 50, pp. 18445–18450, 2007. DOI: 10.1021/jp077095c.
- [127] A. Zabet-Khosousi and A.-A. Dhirani, “Charge transport in nanoparticle assemblies”, *Chemical Reviews*, vol. 108, no. 10, pp. 4072–4124, 2008. DOI: 10.1021/cr0680134.
- [128] T. B. Tran *et al.*, “Sequential tunneling and inelastic cotunneling in nanoparticle arrays”, *Physical Review B - Condensed Matter and Materials Physics*, vol. 78, no. 7, pp. 22–24, 2008. DOI: 10.1103/PhysRevB.78.075437.
- [129] J.-F. Dayen *et al.*, “Enhancing the Molecular Signature in Molecule-Nanoparticle Networks Via Inelastic Cotunneling”, *Advanced Materials*, vol. 25, no. 3, pp. 400–404, 2013. DOI: 10.1002/adma.201201550.
- [130] D. Dulić *et al.*, “One-way optoelectronic switching of photochromic molecules on gold.”, *Physical review letters*, vol. 91, no. 20, p. 207402, 2003. DOI: 10.1103/PhysRevLett.91.207402.

- [131] S. J. van der Molen *et al.*, “Stochastic and photochromic switching of diarylethenes studied by scanning tunnelling microscopy”, *Nanotechnology*, vol. 17, no. 1, pp. 310–314, 2005. DOI: 10.1088/0957-4484/17/1/053.
- [132] S. J. van der Molen *et al.*, “Light-Controlled Conductance Switching of Ordered Metal-Molecule-Metal Devices”, *Nano Letters*, vol. 9, no. 1, pp. 76–80, 2009. DOI: 10.1021/nl802487j.
- [133] J. Liao *et al.*, “Cyclic conductance switching in networks of redox-active molecular junctions”, *Nano Letters*, vol. 10, no. 3, pp. 759–764, 2010. DOI: 10.1021/nl902000e.
- [134] C. M. Guédon *et al.*, “Controlling the interparticle distance in a 2D molecule–nanoparticle network”, *Nanotechnology*, vol. 22, no. 12, p. 125 205, 2011. DOI: 10.1088/0957-4484/22/12/125205.
- [135] J. Liao *et al.*, “Patterned Close-Packed Nanoparticle Arrays with Controllable Dimensions and Precise Locations”, *Small*, vol. 8, no. 7, pp. 991–996, 2012. DOI: 10.1002/smll.201102038.
- [136] Y. Wang *et al.*, “Dimensionality-dependent charge transport in close-packed nanoparticle arrays: from 2D to 3D”, *Scientific Reports*, vol. 4, p. 7565, 2014. DOI: 10.1038/srep07565.
- [137] Y. Viero *et al.*, “High Conductance Ratio in Molecular Optical Switching of Functionalized Nanoparticle Self-Assembled Nanodevices”, *The Journal of Physical Chemistry C*, vol. 119, no. 36, pp. 21 173–21 183, 2015. DOI: 10.1021/acs.jpcc.5b05839.
- [138] A. K. Geim and K. S. Novoselov, “The rise of graphene.”, *Nature materials*, vol. 6, no. 3, pp. 183–91, 2007. DOI: 10.1038/nmat1849.
- [139] A. Holovchenko *et al.*, “Near Room-Temperature Memory Devices Based on Hybrid Spin-Crossover@SiO₂ Nanoparticles Coupled to Single-Layer Graphene Nanoelectrodes”, *Advanced Materials*, vol. 28, no. 33, pp. 7228–7233, 2016. DOI: 10.1002/adma.201600890.
- [140] C. S. Ruiz-Vargas *et al.*, “Contact transfer length investigation of a 2D nanoparticle network by scanning probe microscopy”, *Nanotechnology*, vol. 26, no. 36, p. 365 701, 2015. DOI: 10.1088/0957-4484/26/36/365701.
- [141] A. E. Grigorescu *et al.*, “10nm lines and spaces written in HSQ, using electron beam lithography”, *Microelectronic Engineering*, vol. 84, no. 5-8, pp. 822–824, 2007. DOI: 10.1016/j.mee.2007.01.022.
- [142] S. Kim *et al.*, “Realization of a high mobility dual-gated graphene field-effect transistor with Al₂O₃ dielectric”, *Applied Physics Letters*, vol. 94, no. 6, 2009. DOI: 10.1063/1.3077021.
- [143] M. D. Porter *et al.*, “Spontaneously Organized Molecular Assemblies. 4. Structural Characterization of n-Alkyl Thiol Monolayers on Gold by Optical Ellipsometry, Infrared Spectroscopy, and Electrochemistry”, *Journal of American Chemical Society*, vol. 109, no. 6, pp. 3559–3568, 1987. DOI: 10.1021/ja00246a011.
- [144] M. A. Rampi, O. J. A. Schueller, and G. M. Whitesides, “Alkanethiol self-assembled monolayers as the dielectric of capacitors with nanoscale thickness”, *Applied Physics Letters*, vol. 72, no. 14, p. 1781, 1998. DOI: 10.1063/1.121183.

- [145] D. Gamota *et al.*, Eds., *Printed Organic and Molecular Electronics*. Boston, MA: Springer US, 2004, ISBN: 978-1-4613-4783-5. DOI: 10.1007/978-1-4419-9074-7.
- [146] J. G. Laquindanum *et al.*, “n-Channel organic transistor materials based on naphthalene frameworks”, *Journal of the American Chemical Society*, vol. 118, no. 45, pp. 11 331–11 332, 1996. DOI: 10.1021/ja962461j.
- [147] H. E. Katz *et al.*, “Naphthalenetetracarboxylic diimide-based n-channel transistor semiconductors: Structural variation and thiol-enhanced gold contacts”, *Journal of the American Chemical Society*, vol. 122, no. 32, pp. 7787–7792, 2000. DOI: 10.1021/ja000870g.
- [148] H. E. Katz *et al.*, “A soluble and air-stable organic semiconductor with high electron mobility”, *Nature*, vol. 404, no. 6777, pp. 478–481, 2000. DOI: 10.1038/35006603.
- [149] R. Frisenda *et al.*, “Single-Molecule Break Junctions Based on a Perylene-Diimide Cyano-Functionalized (PDI8-CN2) Derivative”, *Nanoscale Research Letters*, vol. 10, no. 1, p. 305, 2015. DOI: 10.1186/s11671-015-1011-3.
- [150] E. Fischer *et al.*, “Formation of Coloured Forms of Spirans by Low-temperature Irradiation”, *Journal of the Chemical Society*, p. 4522, 1952. DOI: 10.1039/jr9520004518.
- [151] Y. Shiraishi, M. Itoh, and T. Hirai, “Thermal isomerization of spiropyran to merocyanine in aqueous media and its application to colorimetric temperature indication.”, *Physical chemistry chemical physics : PCCP*, vol. 12, no. 41, pp. 13 737–13 745, 2010. DOI: 10.1039/c0cp00140f.
- [152] J. Zhou *et al.*, “Detailed investigation on a negative photochromic spiropyran”, *Journal of Photochemistry and Photobiology, A: Chemistry*, vol. 90, no. 2-3, pp. 117–123, 1995. DOI: 10.1016/1010-6030(95)04082-Q.
- [153] N. Darwish *et al.*, “Multi-Responsive Photo- and Chemo-Electrical Single-Molecule Switches”, *Nano Letters*, vol. 14, no. 12, pp. 7064–7070, 2014. DOI: 10.1021/nl5034599.
- [154] K. Thodkar *et al.*, “Comparative study of single and multi domain CVD graphene using large-area Raman mapping and electrical transport characterization”, *Physica status solidi (RRL) — Rapid Research Letters*, vol. 5, pp. 1–5, 2016. DOI: 10.1002/pssr.201600211.
- [155] J. S. Ágústsson, “Arrays of gold nanoparticles as a platform for molecular electronics”, PhD thesis, University of Basel, May 2011.
- [156] V. Santhanam and R. P. Andres, “Microcontact Printing of Uniform Nanoparticle Arrays”, *Nano Letters*, vol. 4, no. 1, pp. 41–44, 2004. DOI: 10.1021/nl034851r.

Functional molecules measured in MCBJ



A.1 Single-molecule characterization of organic semiconductor Cys-NTCDI

Recent advances in the field of organic electronics created variety of organic semiconductors, which are widely used in TFT-screens available on the consumer market. Chemically, organic semiconductors are the molecules with fused aromatic rings, and the most common are based on naphthalene carbodiimide (NTCDI) or perylene carbodiimide (PTCDI, or PDI) skeleton [145].

NTCDI- as well as PTCDI-based compounds were intensively studied as good n-type organic semiconductors with high electron mobility up to $0.1 \text{ cm}^2/(\text{V} \cdot \text{s})$ observed in the uniform films [146–148]. Such unique properties of organic semiconductors attract interest to investigate the electrical properties on the single molecule level. For the organic semiconductor PDI8-CN2 Frisenda *et al.* [149] demonstrated presence of two conductance configurations (low-G and high-G), which were attributed to the different binding of the molecule to the electrodes due

to presence of two pairs of anchor groups.

To utilize NTCDI-based organic semiconductor in MCBJ as well as in nanoparticle array, two linker groups were added to NTCDI. Synthesized N,N'-bis-(2-sulfanylethyl)-1,4,5,8-naphthalenetetracarboxydiimide (Cys-NTCDI, from Shlomo Yitzchaik group, Hebrew University of Jerusalem; Fig. A.1a) molecule consists of NTCDI core and two thiol-terminated ethyl anchor groups. Thiol groups bond strongly to the gold electrodes, and short ethyl chains decouple the NTCDI core from the linkers. At the same time these ethyl chains are short, so the possible conductance is predicted to be relatively high.

All the measurements were performed in 100 μM solution of Cys-NTCDI in the mixture of tetrahydrofuran and mesitylene (1:4 v/v) with a bias voltage of 0.1 V. The measurements are shown of the Figure A.1b–f.

Conductance histogram (Fig. A.1b) shows the broad conductance peak ($G = 10^{-3.4} G_0$, FWHM = 2.67). Conductance-displacement histogram (Fig. A.1c) also demonstrate presence of slightly slanted conductance plateau with the estimated length of 4.8 Å (Fig. A.1d). Histogram evolution plot (Fig. A.1e) shows the formation of the junction on the time scale. Estimated yield of junction formation is 79% (Fig. A.1f).

Thereby, the measurements demonstrate the possibility of Cys-NTCDI molecule to bridge the gold electrodes to form molecular junction. The distance between terminal sulfur atoms is about 1.5 nm, which is close to the interparticle distance in the NP array with 1-octanethiol. This fact allows to assume possibility to use Cys-NTCDI molecule in the NP array. To test the assumption, the measurements were performed on the regular NPSAN samples, containing decades of individual NPSAN devices (Fig. A.2a). First, voltage-current characteristics were measured for 160 individual two-terminal NPSAN devices with 1-octanethiol (C8SH) shell. Then, sample was placed into 10 mM solution of Cys-NTCDI molecule in mesitylene for 24 hours under argon atmosphere for molecular exchange [121]. After 24 hours, sample was washed in mesitylene and all the devices were measured again. Typical IVs before and after molecular exchange procedure are shown in Figure A.2b.

From all the measured voltage-current characteristics the sheet conductance G_{\square} values were deduced (Fig. A.2c). The distribution of conductance values after exchange is less narrower than before exchange, and average conductance value is higher (Fig. A.2d). the distribution of conductance values after an exchange procedure remains close to normal, which is a signature of effective replacement of C8SH molecules in the network with CysNTCDI molecules [125], which is also confirmed by the scatter plot of G^{CysNTCDI} vs. G^{C8SH} values (Fig. A.2e) as well as the sharpness of $G^{\text{CysNTCDI}}/G^{\text{C8SH}}$ values distribution (Fig. A.2f). The average sheet conductance value for Cys-NTCDI molecule, deduced from the Figure A.2d, is $10^{-5.0} G_0$, which is significantly smaller than measured before in MCBJ. The reason is a low efficiency of an exchange due to short (in comparison to the interparticle distance) length of the molecule. For quantitative characterization of exchange

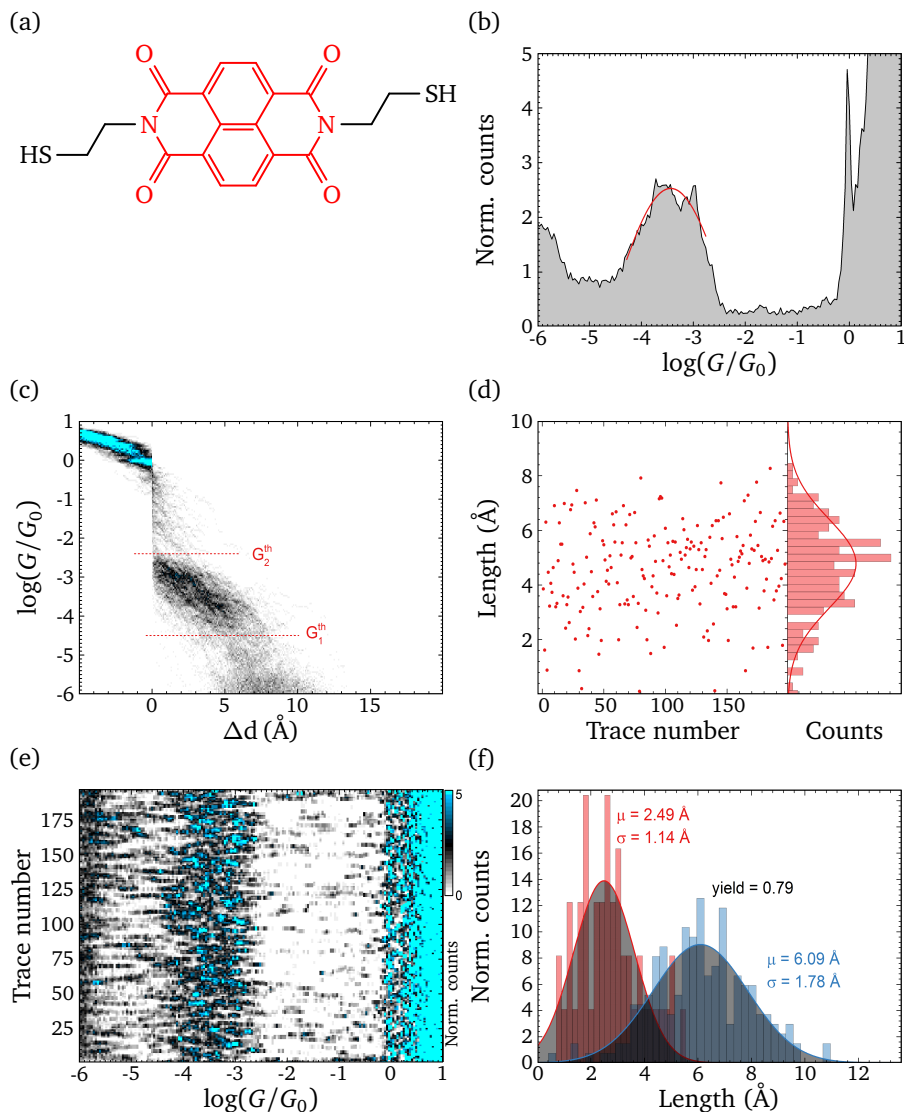


Figure A.1: (a) Structural formula of Cys-NTCDI molecule. NTCDI core is shown in red. (b–f) Measurements of Cys-NTCDI in solution, 197 opening traces. (b) Conductance histogram. Red curve shows the Gaussian fit of the histogram with the peak conductance value of $10^{-3.4} G_0$. (c) Conductance-displacement histogram. Red dashed lines indicate threshold conductances $G_1^{\text{th}} = 10^{-4.5} G_0$ and $G_2^{\text{th}} = 10^{-2.2} G_0$ which define plateau conductance range. (d) Scatter plot of plateau length for all the traces and the distribution. The Gaussian fit of the histogram yields to the average plateau length of 4.8 Å. (e) Histogram evolution plot. (f) Yield of junction formation estimation.

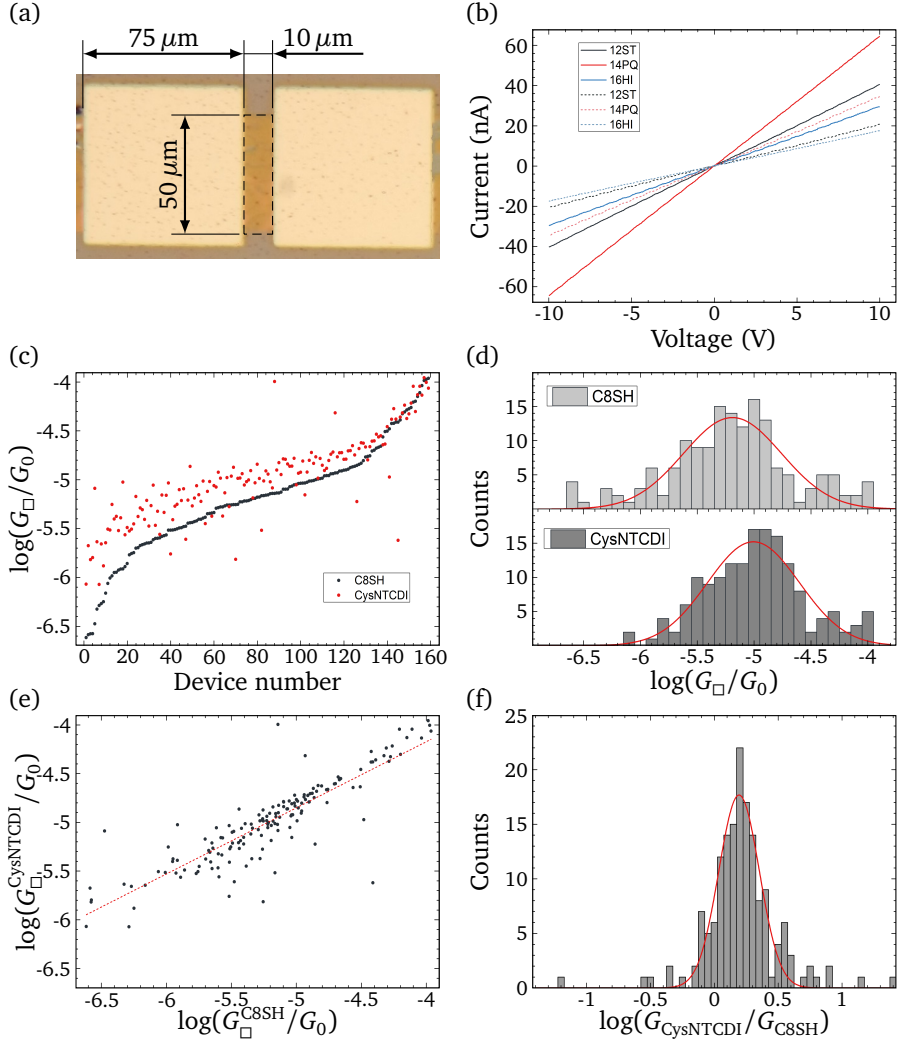


Figure A.2: (a) Optical image of the NPSAN device. The active area of the device (marked with dashed rectangle) is $50 \times 10 \mu\text{m}$. (b) Typical IVs of the NPSAN device before (dashed lines) and after exchange (solid lines), i.e. with C8SH and Cys-NTCDI, respectively. (c) Overview of all measured sheet conductances. Devices are sorted by initial sheet conductance value before exchange for clarity. (d) Distributions of the sheet conductances for all measured devices before and after exchange procedure. Red curves show the Gaussian fit of every histogram. (e) Log-log plot shows the final (CysNTCDI) vs. initial (C8SH) conductances for all devices. Red dashed line shows the linear fit with a slope of 0.68. (f) Distribution of conductance ratio values. The red curve shows the Gaussian fit of the histogram with $\mu = 0.2$ (FWHM = 0.37).

efficiency, the average change in conductance was deduced from the Figure A.2f. Extracted average conductance change is $10^{0.2} \approx 1.6$.

Thereby, possibility to use Cys-NTCDI molecule in the nanoparticle arrays was demonstrated. However, the efficiency of an exchange is low, and the conductance increase in comparison to 1-octanethiol organic shell is less than 2.

A.2 Spiropyran-based compound as a possible molecular optical switch

Optical molecular switches are intensively studied on the level of SAMs, individual molecules in MCBJ and STM-BJ, and on the network level. The most studied photochromic switches are derivatives of azobenzene [65], diarylethene [93] and stilbene [66]. Spiropyranes are another type of chemical compounds which are well known for their photochromic switching. These molecules were first synthesized in the beginning of 20th century, and in 1952 Fischer *et al.* [150] discovered reversible isomerization of spiropyranes caused by UV light illumination. Usually, spiropyranes are colorless, but upon UV light illumination spiro-structure isomerizes into merocyanine-structure [151, 152]. Merocyanines have longer π -conjugated system and are colored compounds. Measurements of spiropyranes in the STM break junctions demonstrated efficient switching on the single molecule level [153].

Here the electrical properties of the spiropyran-like molecule (TSP, from Shlomo Yitzchaik group, Hebrew University of Jerusalem; Fig. A.3, left) were investigated. This molecule has spiropyran core (marked in red in the formula), and 2 linker groups: nitro- and long alkyl chain with 1,2-dithiol-3-yl group in the tail of the chain. Dithiolyl group is used as a linker to create strong covalent bond with the gold electrodes.

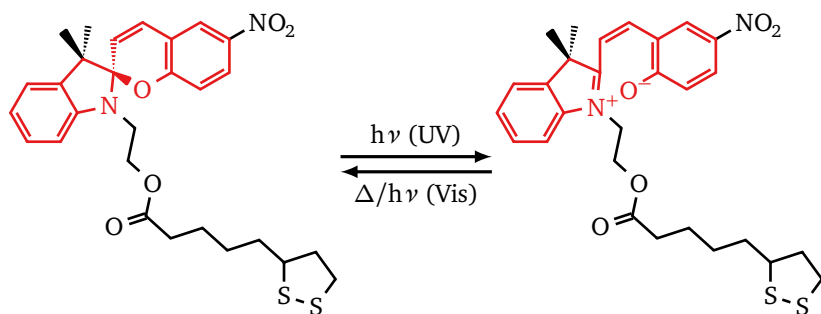


Figure A.3: Reversible isomerization of TSP molecule caused by light illumination. Spiropyran (left) and mesocyanine (right) cores of both compounds are shown in red.

All the measurements were performed in a freshly prepared 100 μ M solution of

TSP molecule in the mixture of tetrahydrofuran and mesitylene (1:4 v/v).

First we measured TSP solution without light illumination (Fig. A.4a). To investigate the optical switching of TSP, we performed the following measurements:

1. 2 mL of TSP was exposed to UV light for 15 minutes. During exposure the color of the solution is changing to slightly blueish, indicating isomerization of the molecule to merocyanine. After illumination the not-exposed solution in the liquid cell was exchanged with 100 μ L of exposed one, and 50 cycles were recorded (Fig. A.4b).
2. 50 traces were recorded with continuous UV light illumination (Fig. A.4c). Since the setup is not completely insulated in such regime, much higher noise level is observed (Fig. A.4d).
3. The solution of TSP was exposed to UV light for 15 minutes in the cell, and 50 traces were recorded after (Fig. A.4e).

In all the cases no clear signature of molecular junction formation was observed. This can be explained by very long alkyl chain between anchor group and aromatic subsystem.

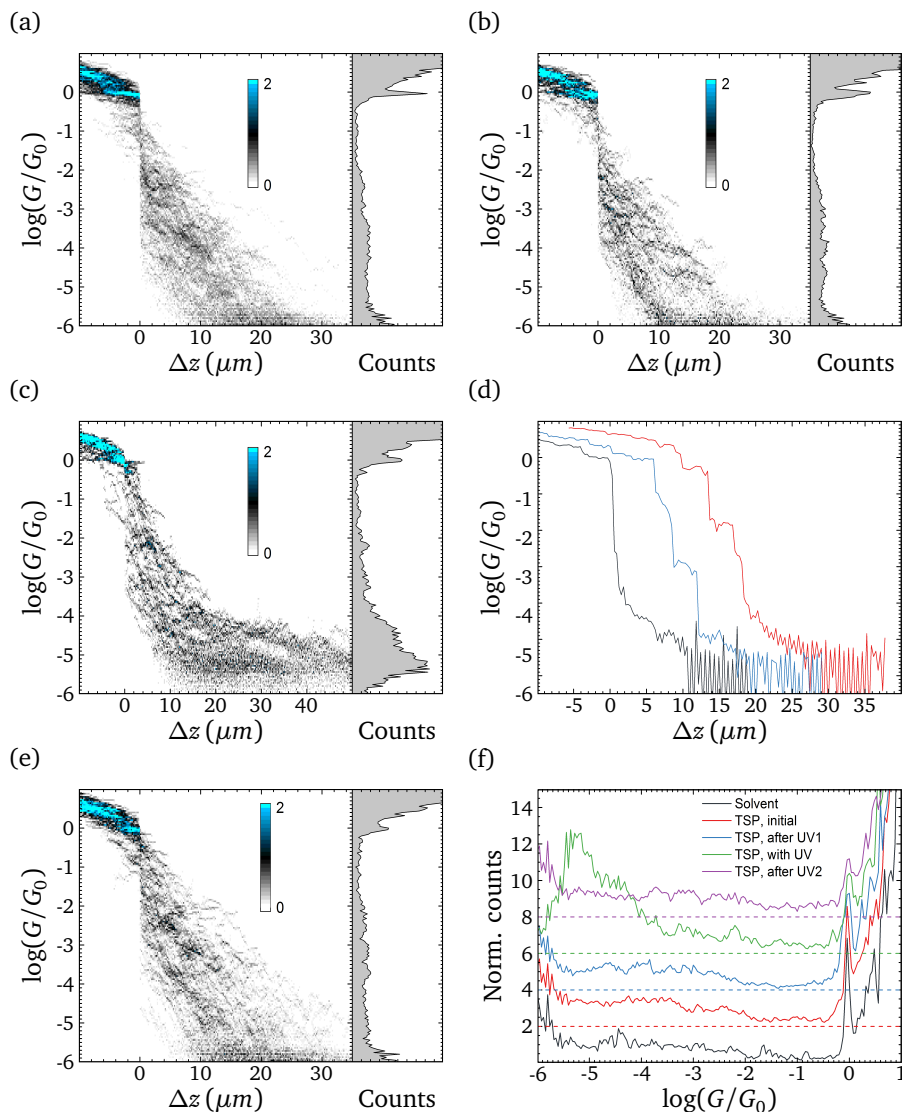


Figure A.4: TSP molecule measurements. (a–c, e) Conductance-displacement histograms for: (a) 100 μM solution of TSP before UV exposure, (b) TSP after 15 min of UV exposure, (c) TSP with continuous UV exposure in situ, (e) TSP after 15 minutes UV exposure. (d) Typical opening traces during UV exposure. Oscillations in the range $< 10^{-5} G_0$ occur due to UV exposure of connecting wires and because the setup is not completely isolated, and 50 Hz extra noise is possible. (f) Comparison of conductance histograms for all the measurements.

Fabrication

B.1 MCBJ fabrication

MCBJ samples are fabricated as described before [52, 58]. First, spring steel plates (65×65 mm) with a thickness of 0.3 mm are covered with 4 layers of polyimide (HD-2610, HD Microsystems), followed by hard bake in the vacuum oven for 1 hour at 375°C . Final thickness of polyimide is about $5\text{ }\mu\text{m}$. After that, the plates are cut into individual MCBJ substrates with the size of 24×10 mm each by laser cutting.

Fabrication steps of the MCBJ samples are the following (Fig. B.1):

1. Spin-coat 500–550 nm of PMMA (PMMA 671.09 950k, diluted with chlorobenzene to 5% concentration) for 40 seconds at 4000 rpm, followed by baking on the hot plate for 3 minutes at 180°C .
2. Write the structure with e-beam at the acceleration voltage of 10 kV with an area dose of $150\text{ }\mu\text{C}/\text{cm}^2$ for rough structures and the line dose of $900\text{ pC}/\text{cm}$ for fine structures.

3. Develop the samples in the mixture of isopropyl alcohol (IPA) and methylisobutylketone (MIBK) (3:1 v/v) for 55 seconds, rinse in IPA, dry in N₂ flow.
4. Evaporate 5 nm of titanium as an adhesion layer under an angle of 60 degrees (to avoid presence of titanium in the constriction area) and 60 nm of gold.
5. Remove excess metals by dissolving not-exposed PMMA in warm acetone (lift-off process). Rinse the sample in IPA and dry in N₂ flow.
6. Spin-coat 5 μm of UV-sensitive resist (HD-4104, HD Microsystems), followed by soft-baking on the hotplate: 2 minutes at 90 °C and 2 minutes at 100 °C.
7. Expose with UV light (365 nm, 350 W/cm², 6.5 seconds) the entire sample except protected areas of contact pads and constriction of the junction.
8. Develop and rinse the resist, dry in N₂ flow.
9. Post bake the resist in the vacuum oven ($p < 10^{-5}$ mTorr) for 1 hour at 375 °C.
10. Etch the polyimide using the reactive ion etching. RIE parameters: 100 mTorr, 32 sccm O₂ and 8 sccm CHF₃ with the power of 100 W, 3 minutes.

The liquid cell is made of teflon ring (Viton[®]) and fixed on the sample using polyimide sealing (PI-2610), followed by hard-bake in the oven.

B.2 Graphene growth and transfer

CVD graphene for hybrid devices was grown in the home-made furnace. The growth is performed on the copper foil (25 μm thick, 99.8% purity) at 1000 °C using methane CH₄ as a precursor. At this temperature, methane decomposes into carbon and hydrogen and forms multi-domain monolayer of graphene on the copper surface (see [154] for details).

Since graphene is grown on both surfaces of the copper, one surface ('top side') is covered with PMMA (50k, spin-coated for 30 seconds at 3000 rpm, without post-bake). Back side of copper foil is etched in RIE plasma (16 sccm of O₂ and 8 sccm of Ar, 250 mTorr, 30 W, 1 minute).

For the transfer, prepared copper foil is placed on the surface of 0.1 M solution of ammonia persulfate (NH₄)₂S₂O₈ to etch the copper (Fig. B.2a, Eq. B.1):



Typical etching time is about 5–6 hours. After etching, the thin film of PMMA with graphene on the bottom side is floating on the water surface (Fig. B.2b). To clean the graphene, the solution in the beaker is several times exchanged with DI-water. After that, cleaned Si/SiO₂ (300 nm) substrate is dipped into the water below the

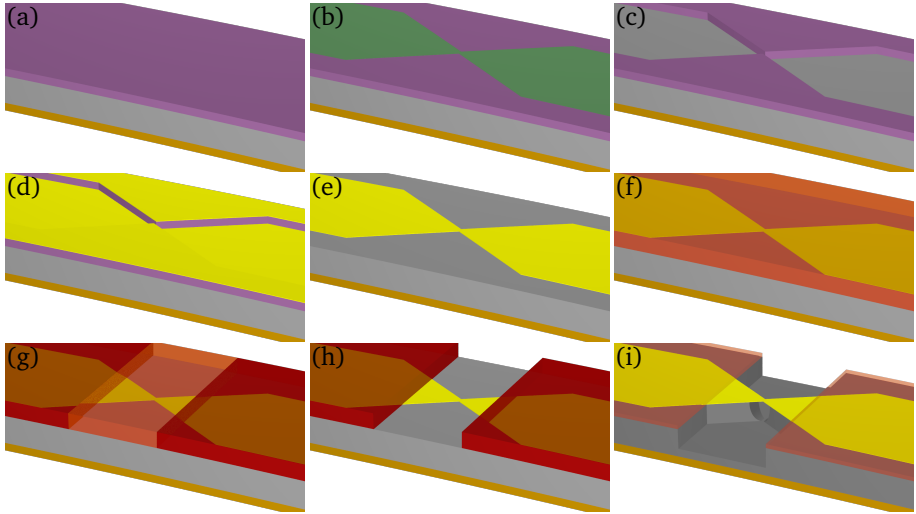


Figure B.1: MCBJ fabrication steps. (a) Spring steel substrate with 5 μm thick polyimide layer and 500 nm PMMA layer (b) E-beam exposure. (c) PMMA Development. (d) Metals (Ti/Au) evaporation. (e) Lift-off. (f) UV-sensitive polyimide spinning. (g) UV exposure. (h) UV resist development. (i) RIE etching and final device.

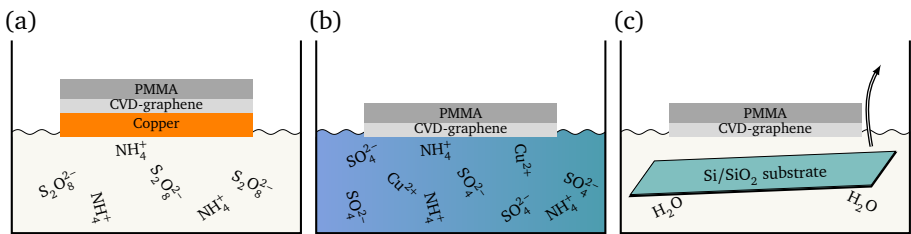


Figure B.2: Graphene transfer procedure. (a) Start of copper etching. (b) After full etching of copper solution becomes blueish. (c) 'Fishing' of the graphene/PMMA stack with Si/SiO₂ substrate.

floating PMMA/graphene film, and the carefully lifted up letting PMMA/graphene film to lay on top of the substrate without wrinkles (Fig. B.2c).

B.3 Graphene patterning for multi-terminal hybrid devices

CVD-grown graphene, transferred onto Si/SiO₂ (300 nm) substrate (with predefined markers for proper alignment of e-beam structures) was used. To pattern the graphene, PMMA mask is used as an etching mask for dry etching.

Fabrication protocol:

1. Spin-coat 500 nm of PMMA (950k, 5% in chlorobenzene) at 4000 rpm for 40 seconds, followed by baking on the hotplate at 180 °C for 3 minutes.
2. Write the e-beam structures with an accelerated voltage of 10 kV and a dose of 900 $\mu\text{C}/\text{cm}^2$.
3. Develop in MIBK:IPA mixture (1:3 v/v) for 1 minute.
4. Etch the graphene using PMMA as a protecting mask. Parameters of the RIE: 5 sscm of Ar, 16 sscm of O₂, pressure 250 mTorr, RF power 50 W for 40 seconds.
5. Remove excess PMMA in warm acetone: 50 °C for 5 minutes.

Final gap size between the graphene electrodes is extremely sensitive to the dose (see. Fig. B.3).

B.4 PMMA master fabrication

Masters for the PDMS stamps, designed for local NP array transfer, are prepared in thick PMMA layer.

Fabrication procedure protocol:

1. Clean Si/SiO₂ substrates (17×17 mm with 300 nm of thermally grown SiO₂) in acetone and IPA. Substrates have previously fabricated markers used for precise write-field alignment during e-beam lithography. The markers are fabricated in gold and form a squared grid with a step of 200 μm .
2. Spin-coat PMMA (PMMA AR-P 649.04 from Allresist, 9% solution in chlorobenzene) at 2000 rpm for 30 sec. Bake for 5 minutes at the 180 °C on the hotplate. Final thickness of the resist is 3 μm . The gold markers are visible in the SEM with 30 kV acceleration voltage, making proper writefield alignment during e-beam exposure possible.

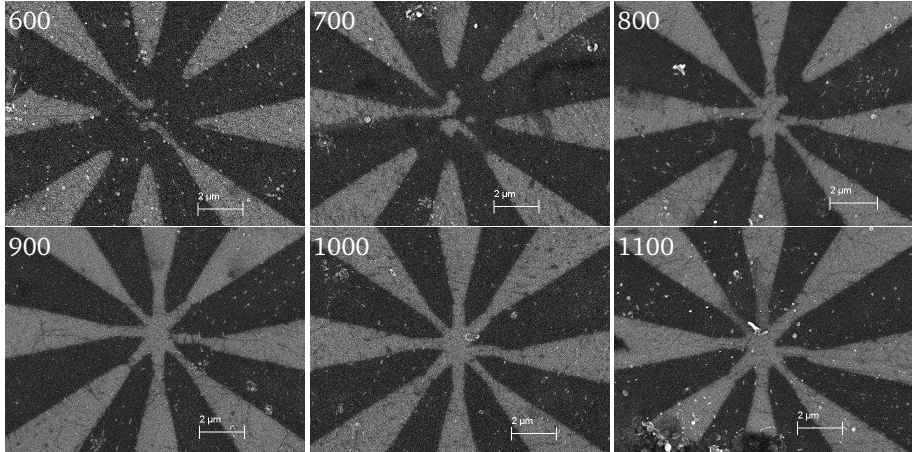


Figure B.3: Patterned graphene electrodes after RIE and PMMA removal. The etching mask was prepared by exposure of 500 nm thick PMMA to 10 kV e-beam with the doses of 600, 700, 800, 900, 1000 and 1100 $\mu\text{C}/\text{cm}^2$.

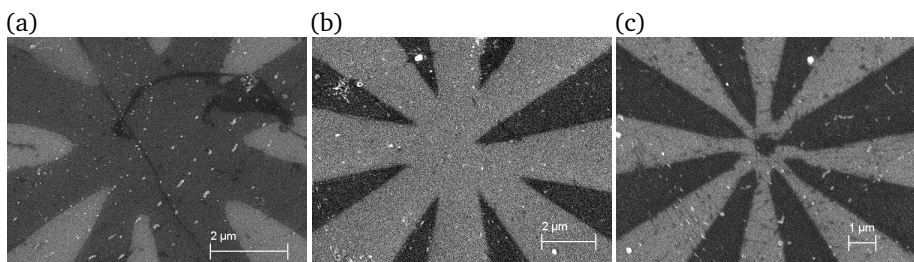


Figure B.4: Typical problems of e-beam lithography: (a) not enough dose, no gap between electrodes; (b) overdose, the gap is too big; (c) wrong exposed area, graphene residues in the center area

3. Write the structures using e-beam lithography with 30 kV accelerated voltage and the area dose of $350 \mu\text{C}/\text{cm}^2$.
4. Develop the sample in MIBK:IPA (1:3 v/v) mixture for 1 minute.

B.5 PDMS stamps fabrication

The stamps for NP array transfer are fabricated using PDMS (polydimethylsiloxane, Sylgard[®] 184 Silicone elastomer, from Dow Corning).

Fabrication protocol:

1. Clean the master in the IPA (not ethanol for PMMA masters!).
2. Put the master on the bottom of a plastic petri dish (40 mm in diameter). Be sure that there is nothing on the bottom, so the substrate is completely parallel to the bottom of the dish.
3. Prepare PDMS:
 - add together 10 g of the elastomer base and 1 g of curing agent;
 - mix everything properly till it forms uniform small bubbles.
4. Pour the mixture on top of the PMMA master.
5. Put the dish into desiccator and carefully outgas in slow steps for 15–20 minutes.
6. Transfer the dish into baking oven, heated to 60 °C. Check the parallelism of the dish with levels.
7. Bake the PDMS for 90 minutes.
8. After baking, peel the PDMS off and cut it into small pieces with individual stamps.

B.6 Nanoparticles preparation

Gold nanoparticles are synthesized using the reaction of Au^{3+} reduction by sodium citrate [121, 155].

B.6.1 Synthesis

First, three solutions are prepared in deionized water (DI-water):

- 1% (w/v) chloroauric acid tetrahydrate $\text{HAuCl}_4 \cdot 4\text{H}_2\text{O}$ (ACS reagent from Sigma-Aldrich) in DI-water;
- 1% (w/v) sodium citrate dihydrate $\text{C}_6\text{H}_5\text{O}_9\text{Na}_3 \cdot 2\text{H}_2\text{O}$ (>99.5% purity) in DI-water;
- 1% (w/v) tannic acid $\text{C}_{76}\text{H}_{52}\text{O}_{46}$ (ACS reagent) in DI-water.

Fabrication protocol:

1. In a clean 150 mL beaker mix 1 mL of 1% chloroauric acid with 79 mL of DI-water. Add magnetic stirrer into the beaker, cover with watch glass and heat at the hotplate for 15 minutes at 80 °C.
2. In clean 25 mL beaker mix 4 mL of 1% sodium citrate solution, 80 μL of 1% tannic acid solution and 16 mL of DI-water. Cover the beaker with watch glass and heat at the hotplate for 15 minutes at 80 °C.
3. After 15 minutes, heat a hotplate up to 250 °C for 5 minutes.
4. Quickly pour the contents of 25 mL beaker into bigger one. The solution becomes purple.
5. Wait until solution turns red and leave it on the hotplate for 10 more minutes.
6. Cool down the solution in the ice water.

Prepared solution can be stored for months in dark.

B.6.2 Functionalization

Coverage of nanoparticles with alkanethiol organic shell is performed in ethanol (Ethanol absolute, ACS reagent from Sigma Aldrich).

Protocol:

1. Fill 24 Eppendorf TubesTM with 1 mL of aqueous gold nanoparticle solution.
2. Place all the tubes into centrifuge for 45 minutes at 13 krpm. After centrifugation, the precipitate of gold nanoparticles is formed on the bottom of the tube.
3. With a pipette carefully remove the water above the precipitate.
4. Add ~1 mL of ethanol into the tubes, mix the contents with the shaker for 30–40 seconds.

5. Transfer all the solutions from the tubes into a clean 20 mL bottle.
6. Put the bottle in an ultrasonic bath for 10 minutes at the temperature below 30 °C.
7. Add 200 μ L of the desired alkanethiol (>98%, distilled before usage) to the bottle.
8. Leave the bottle in darkness for 2–3 days for functionalization.

Alkanethiol-covered nanoparticles form black precipitate on the bottom and solution becomes colorless.

B.7 Nanoparticles transfer

First, alkanethiol-covered nanoparticles are transferred into chloroform (CHCl_3 , >99.8% from Sigma-Aldrich):

1. With a pipette carefully remove ethanol from above the precipitated nanoparticles.
2. Add new ethanol and wait for 1 hour.
3. Repeat the step 1, try to remove as much ethanol as possible.
4. Add 4 mL of chloroform into the bottle.
5. Put the bottle in ultrasonic bath for ~ 10 minutes until solution turns red.

To transfer the nanoparticles on the substrate, the Langmuir-Schaefer method is employed. The transfer procedure follows described in [156]:

1. Into the Petri dish put 2–3 glass slides stacked to each other and to the bottom of the dish.
2. Teflon ring with an inner diameter of 15 mm (carefully cleaned with soap and water) put on top of glass slides.
3. Fill the Petri dish with DI water. Suspended water surfaces is formed inside the Teflon ring (Fig. B.5a).
4. Transfer 300 – 350 μ L of NPs solution into a small vial.
5. With a pipette carefully transfer NPs solution from the vial on top of suspended water surface.
6. Chloroform starts to evaporate, forcing nanoparticles to form self-assembled array (Fig. B.5b)

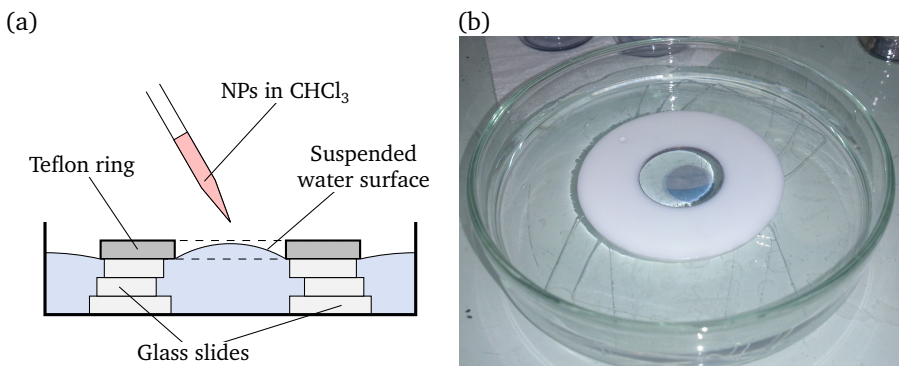


Figure B.5: (a) Schematic of NPs transfer from chloroform solution onto suspended water surface. (b) Optical image of self-assembled 2D nanoparticle array on the water surface after solvent evaporation.

7. Clean the stamps in ethanol for 5 minutes in the ultrasonic bath.
 8. Ink the stamp: carefully bring the stamp with a tweezers into a contact with the array on top of the water surface for 10 seconds.
 9. Tilt the stamp to break a contact with a surface and remove the it.
 10. Carefully remove excess water from the stamp with a piece of clean soft paper.
- The stamp is ready for stamping.

B.8 NPSAN fabrication

Regular NPSAN devices are fabricated following the procedure described in [121]:

1. Prepare clean Si/SiO₂ substrates with a size of $\sim 5 \times 5$ mm.
2. Put the inked PDMS stamp upside down (with inked surface up) on the glass slide.
3. ‘Drop’ the substrate on the stamp without additional pressure.
4. After 10 seconds, carefully tilt the substrate to remove it from the stamp.

For the regular NPSAN devices, NP array is patterned in stripes with a width of $29 \mu\text{m}$ and $53 \mu\text{m}$ separated by $44 \mu\text{m}$ (Fig. B.6a). The period of the structure ($85 \mu\text{m}$) corresponds to the period of the TEM grid with 300 lines/inch.

To evaporate the contact pads, the TEM grid is carefully placed on top of the samples with patterned NP array stripes, aligned under the microscope and fixed

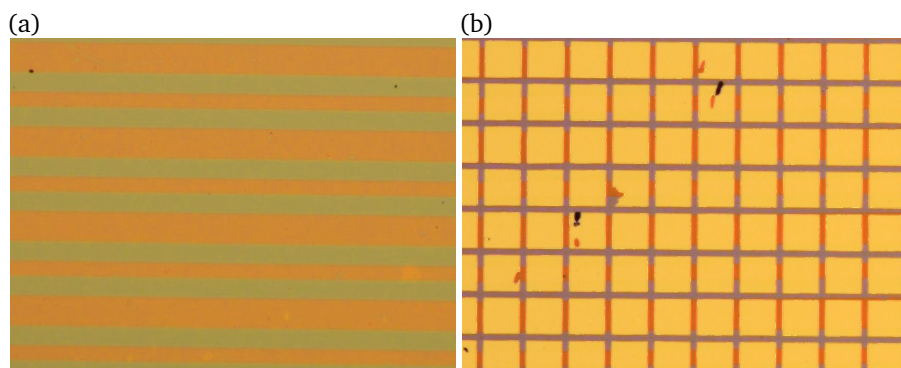


Figure B.6: (a) Optical image of transferred NP array. NP array is patterned in stripes with the width of $29\text{ }\mu\text{m}$ and $53\text{ }\mu\text{m}$. (b) Optical image of transferred NP array after contact pads evaporation. Contact pads (5 nm Ti/45 nm Au) are $75 \times 75\text{ }\mu\text{m}$ in size.

with a cover. Metal contact pads (5 nm Ti/45 nm Au) are evaporated using TEM grid as a shadow mask (Fig. B.6b). Every two neighboring contact pads and NP array between them represent individual two-terminal NPSAN device.

List of publications

Journal articles

1. **Anton Vladyka**, J. Brunner, J. Overbeck, M. Gantenbein, M. Mayor, C. Schö-
nenberger, R. R. Ferradás, J. F. Rodriguez, and M. Calame, “Controlled in-situ
formation of organometallic electronic junctions”, *In preparation*, 2017.
2. T. Ghane, D. Nozaki, A. Dianat, **Anton Vladyka**, R. Gutierrez, J. Chinta, S.
Yitzchaik, M. Calame, and G. Cuniberti, “Interplay between Mechanical and
Electronic Degrees of Freedom in π -Stacked Molecular Junctions: From Single
Molecules to Mesoscopic Nanoparticle Networks”, *The Journal of Physical
Chemistry C*, vol. 119, no. 11, pp. 6344–6355, 2015. DOI: 10.1021/jp512524z.
3. J. Liao, S. Blok, S. van der Molen, S. Diefenbach, A. Holleitner, C. Schö-
nenberger, **Anton Vladyka**, and M. Calame, “Ordered nanoparticle arrays
interconnected by molecular linkers: Electronic and optoelectronic proper-
ties”, *Chemical Society Reviews*, vol. 44, no. 4, pp. 999–1014, 2015, ISSN:
0306-0012. DOI: 10.1039/c4cs00225c.
4. V. A. Sydoruk, D. Xiang, S. A. Vitusevich, M. V. Petrychuk, **Anton Vladyka**,
Y. Zhang, *et al.*, “Noise and transport characterization of single molecular
break junctions with individual molecule”, *Journal of Applied Physics*, vol. 112,
no. 1, p. 14908, 2012, ISSN: 00218979. DOI: 10.1063/1.4736558.

Oral contributions

1. **Anton Vladyka**, J. Brunner, M. Gantenbein, M. Mayor, R. Ferradás, J. Ferrer,
and M. Calame, “Controlled formation of organometallic molecular junctions
in liquid environment”, *8th International Conference on Molecular Electronics*
“*Electmol-2016*”, Paris, France, 2016.

-
2. **Anton Vladyka**, Y. Viero, D. Vuillaume, and M. Calame, “Self-assembled nanoparticle arrays with graphene contacts”, *2016 European Material Research Society Spring Meeting*, Lille, France, 2016.
 3. **Anton Vladyka**, J. Brunner, C. Nef, R. Gutierrez, V. G. Suarez, J. Ferrer, *et al.*, “Molecular and carbon-based devices for electronic functionality”, *Joint Workshop between the EC FP7 projects SYMONE and MOLESCO and 1st annual workshop of the project MOLESCO*, Engelberg, Switzerland, 2015.

Poster contributions

1. J. Overbeck, **Anton Vladyka**, M. Gantenbein, S. Neumann, D. Marti, R. R. Ferradás, *et al.*, “Investigation of electron transport in molecular and optoelectronic nanojunctions”, *8th International Conference on Molecular Electronics “Elecmod-2016”*, Paris, France, 2016.
2. **Anton Vladyka**, J. Overbeck, M. Gantenbein, S. Neumann, D. Marti, R. R. Ferradás, *et al.*, “Importance of contacts and functional backbone in molecular electronic junctions”, *Swiss Nano Convention*, Basel, Switzerland, 2016.
3. **Anton Vladyka**, J. Brunner, M. Gantenbein, R. R. Ferradás, V. García-Suárez, J. Ferrer, M. Mayor, and M. Calame, “The role of metal-molecule interactions in stable molecular junctions”, *SNI Annual Meeting*, Lenzerheide, Switzerland, 2015.
4. **Anton Vladyka**, C. Nef, J. Chinta, S. Yitzchaik, C. Schönenberger, and M. Calame, “Molecular and carbon-based devices for electronic functionality”, *International Workshop “Controlled Charge and Heat Transport at the Molecular Scale”*, Konstanz, Germany, 2014.
5. **Anton Vladyka**, V. Sydoruk, S. Vitusevich, M. Petrychuk, D. Xiang, A. Ofenhäusser, V. Kochelap, A. Belyaev, and D. Mayer, “Transport properties characterization of individual molecule device using noise spectroscopy: A new approach”, *THE PHYSICS OF SEMICONDUCTORS: Proceedings of the 31st International Conference on the Physics of Semiconductors (ICPS) 2012*, AIP Publishing, vol. 1566, 2013, pp. 401–402. DOI: 10.1063/1.4848455.

Curriculum Vitae

05.09.1988 Born in Yalta, Crimea, Ukraine

Education

11.2012–02.2017 Ph.D. student in the field of Molecular Electronics, University of Basel, Switzerland

09.2010–05.2012 M.Sc. in High Technologies, Institute of High Technologies, Taras Shevchenko National University of Kyiv, Ukraine
Thesis: “Transport and noise characteristics of individual biomolecules in mechanically controllable break-junctions”, performed in FZ Jülich

09.2006–06.2010 B.Sc. in Applied Physics, Department of Radiophysics, Taras Shevchenko National University of Kyiv, Ukraine

09.2005–06.2006 Department of Chemistry, Taras Shevchenko National University of Kyiv, Ukraine

Research experience

11.2012–present Research assistant, University of Basel, Switzerland

07.2011–06.2012 Assistant student, Forschungszentrum Jülich, Germany